ISSN: 2227-6912
E-ISSN: 2790-0479
https://doi.org/10.61413/SMAE4063

Azerbaijan Technical University

MACHINE SCIENCE

2
2025

International scientific-technical journal

MACHINE SCIENCE

MAŞINŞÜNASLIQ МАШИНОВЕДЕНИЕ

International scientific-technical journal
Beynəlxalq elmi-texniki jurnal
Международный научно-технический журнал

Number 2
2025

Founder: The Ministry of Education of Azerbaijan Republic
Təsisçi: *Azərbaycan Respublikası Təhsil Nazirliyi*
Учредитель: *Министерство образования Азербайджанской Республики*

The journal is included into the list confirmed by Higher Attestation Commission of the Azerbaijan Republic of editions for the publication of works of competitors for scientific degrees

Jurnal Azərbaycan Respublikası Ali Atestasiya Komissiyasının təsdiq etdiyi elmi dərəcə iddiaçılarının əsərlərinin çap edildiyi dövri elmi nəşrlərin siyahısına daxil edilmişdir.

Журнал входит в перечень, утвержденных ВАК Азербайджанской Республики, изданий для публикации трудов соискателей ученых степеней

Journal was founded according the order No1861 Ministry of Education of Azerbaijan Republic on the date 25.11.2011. Registration No 3521. Journal is published at least twice a year.

Jurnal Azərbaycan Respublikası Təhsil Nazirliyinin 25.11.2011-ci il tarixli 1861 saylı əmri əsasında təsis edilmişdir. Qeydiyyat No 3521. İldə ən azı iki nömrə nəşr edilir.

Учреждено приказом за №1861 от 25.11.2011 года Министерства образования Азербайджанской Республики. Регистрация № 3521. Ежегодно публикуется два номера.

It has been published since 2001. Published in 2001 - 2011 with a name "Mechanics-machine building"
2001-ci ildən nəşr edilir. 2001 – 2011-ci illərdə "Mexanika-maşınqayırma" adı ilə çap edilmişdir.
Издается с 2001 года. В 2001 – 2011 годах издано под называнием «Механика-машиностроение»

The "MACHINE SCIENCE" journal is supported by Azerbaijan Technical University, which means there are no publication fees for authors.
"MAŞINŞÜNASLIQ" jurnalı Azərbaycan Texniki universiteti tərəfindən dəstəklənir və məqalələrin nəşri üçün müəlliflərdən hər hansı ödəniş tələb olunmur.
Журнал «МАШИНОВЕДЕНИЕ» поддерживается Азербайджанским Техническим Университетом, что означает, что с авторов не взимается плата за публикацию статей.

Editorial address**:* ***Redaksiyanın ünvanı: ***Адрес редакции:***	Baku, AZ1073, H.Javid ave., 25. AzTU Tel: (+994 12) 539 12 25 E-mail: msj@aztu.edu.az	© Machine Science, 2025 **ISSN:** 2227-6912 **E-ISSN:** 2790-0479

Contents

MACHINE SCIENCE
ISSN: 2227-6912
E-ISSN: 2790-0479
2025, № 2 Pages 4-13

CHALLENGES IN THE INTEGRATION OF GREEN ENERGY SOURCES AND THE APPLICATION OF FUZZY CONTROL TECHNIQUES FOR WIND TURBINE POWER REGULATION

Nurali YUSIFBAYLI[1,a*], Huseyngulu GULIYEV[1,b], Nikita TOMIN[2,c], Famil IBRAHIMOV[1,d]

[1]*Azerbaijan Technical University, Baku, Azerbaijan*
[2]*Melentiev Energy Systems Institute of the Siberian Branch of the RAS, Irkutsk, Russia*

E-mail: *[a]yusifbayli.n@gmail.com, [b]huseyngulu@mail.ru, [c]tomin.nv@gmail.com, [d]amfanet@mail.ru

https://doi.org/10.61413/NKAT9944

Abstract: This paper examines key aspects and challenges arising from the integration of green energy sources into next-generation power systems, with a particular focus on wind turbines. It examines the technical and operational limitations caused by the variable and probabilistic nature of wind flow, as well as their impact on power system stability, power supply reliability, and power quality. A separate section is devoted to the use of fuzzy controllers for regulating wind turbine output power under environmental uncertainty and incomplete initial information. It is demonstrated that the use of fuzzy logic provides more flexible and adaptive control, reduces fluctuations in generated power, and improves the overall efficiency of the control system compared to conventional control algorithms. The presented findings confirm the potential of implementing intelligent control methods when integrating wind turbines into power systems with a high share of renewable energy sources.

Keywords: *green energy, wind energy, power system integration, Fuzzy control systems, Fuzzy controller, output power control, wind turbine, renewable energy.*

INTRODUCTION

In recent decades, renewable energy sources (RES) have evolved from an alternative energy source into a key driver of sustainable global economic development [1]. Among RES, wind turbines (WTs) and solar energy systems occupy a special place, currently demonstrating the highest rates of growth and technological advancement. The development of these technologies is driven by several factors: the depletion of traditional fuel and energy resources, the need to reduce greenhouse gas emissions, and the growing demand for environmentally friendly and decentralized electricity generation [2, 3].

According to the World Wind Energy Association (WWEA) Technical Committee, by the end of 2024 global installed wind power capacity had surpassed approximately 1 173 GW, with wind energy contributing around 10–12 % of total global electricity generation and continued robust annual installations, reflecting significant growth compared to earlier decades [4, 5]. In subsequent years, this trend has intensified significantly: wind energy has become one of the most dynamically developing sectors of the electric power industry, second only to solar generation in terms of growth rates. Both industrialized countries and emerging economies, actively investing in green energy, have made a significant contribution to this process. Table 1 shows the installed capacity of renewable energy in the world's leading countries.

Table 1. Installed renewable energy capacity in leading countries around the world (as of ~2024/2025)

Country	Wind power (Wind) – MW	Solar Energy (Solar) – MW	Total installed capacity of renewable energy sources - MW
China	520 000	886 000	>1 400 000
USA	153 000	140 000	293 000
Germany	73 000	60 000	133 000
India	48 000	75 000	123 000
Brazil	33 000	15 000	48 000
Spain	32 000	15 000	47 000
United Kingdom	31 000	15 000	46 000
France	24 500	15 000	40 000
Canada	18 400	5 000	23 400

As Table 1 shows, China is a clear leader in installed capacity in both wind and solar energy and surpasses other countries in total renewable energy capacity. The United States and Germany are also major centers of green generation, while countries such as India, Brazil, and the United Kingdom are demonstrating significant growth and investment in renewable energy sources [6-8].

Despite the global growth of wind energy, Azerbaijan's position during the period under review remained extremely modest. In terms of installed wind power capacity, Azerbaijan’s wind electricity capacity (approximately 0.07 GW / 70 MW) places the country around 74th globally in recent comparative rankings of national wind installations, reflecting its relatively small wind power sector compared with major producers. significantly behind not only leading industrialized nations but also a number of developing countries. This lag is explained by a combination of factors, including the energy sector's focus on traditional hydrocarbon resources, insufficient regulatory support for renewable energy, and limited investment in wind energy projects.

At present, wind energy has become a strategically important area for Azerbaijan. The country's wind energy potential is estimated at approximately 25 billion kWh per year. The most favorable conditions for wind energy development are concentrated on the Absheron Peninsula, in the Caspian Sea region, and in several mountainous regions, where stable and relatively high wind speeds are observed, Table 2. In recent years, the country has been taking consistent steps to integrate renewable energy sources into the national energy system, which meets both energy security objectives and international commitments to reduce its carbon footprint [9,10] The current stage of wind energy development is characterized by significant advances in wind turbine aerodynamics, power electronics, energy storage systems, and intelligent generation control. Increasing the unit capacity of wind turbines, increasing their reliability, and reducing the specific cost of electricity generation make wind energy competitive with traditional energy sources. In this context, the further development of wind energy technologies in Russia and Azerbaijan should be considered an important element of a long-term sustainable energy development strategy.

Table 2. Development of wind and solar energy in Azerbaijan

Indicator	Wind energy	Solar energy
Technical Potential	≈ 25 billion kWh/year	≈ 23 billion kWh/year
Major Development Regions	Absheron Peninsula, Caspian zone, Nakhchivan	Nakhchivan Autonomous Republic, Kura-Araz Lowland, Karabakh
Average Natural Conditions	Average wind speed 7–9 m/s	Solar radiation 1500–1700 kWh/m² per year
Installed Capacity (2024, Estimate)	≈ 1500 MW	≈ 1200 MW
Share in Renewable Energy Structure	~56 %	~44 %
Key Completed Projects	Wind farms in Absheron and Caspian wind farms	Solar power plant in Nakhchivan, pilot solar power stations
Promising Development Areas	Offshore wind power, hybrid wind farms	Large solar power plants, distributed solar generation
Main Advantages	High stability of wind flows	High insolation and large land resources
Main Limitations	Uneven winds, network limitations	Daily and seasonal unevenness of generation
Technical Potential	≈ 25 billion kWh/year	≈ 23 billion kWh/year

Using wind energy to generate electricity has several advantages. Compared to traditional energy sources, wind energy is infinite and free. It does not produce environmentally harmful gases that cause climate change.

However, wind energy also has its drawbacks, the most serious of which is its erratic nature. Power fluctuations associated with wind speed variability are a significant issue in a modern power system containing wind turbines. As the number of wind turbines continues to grow [11-15], their impact on power system reliability also becomes increasingly significant. Therefore, the integration of green energy sources is becoming a pressing issue for ensuring the operational reliability and sustainability of power systems as a whole.

JUSTIFICATION FOR THE APPLICATION OF A FUZZY ALGORITHM FOR CONTROLLING THE OUTPUT POWER OF WIND TURBINES

The efficiency of wind turbines in distribution networks can be improved using automatic control systems. A wind turbine is a nonlinear and nonstationary object, which can be controlled using fuzzy controllers [11, 16-18].

The power of the wind flow acting on the wind wheel is determined by the formula:

$$P = \frac{1}{2} \rho \cdot A \cdot v^3 \cdot C_p \tag{1}$$

where A – area used by the wind turbine, m^2 - $A = (\pi / 4) \cdot D^2$; D – wind wheel diameter, m; v – wind flow speed, m/s; C_p – power take-off coefficient (betting limit), depends on the design of the wind wheel and wind speed (for real devices 0.35-0.5), in general 0.593; ρ – density of the incoming flow (air), at sea level 1.225 kg/m2. Theoretically, about 57% of wind energy can be used from 1 m2, depending on the wind speed and the type of wind wheel, but in practice – no more than 33%.

So, as can be seen from formula (1), the power of a wind turbine is proportional to the cube of the wind speed: $P \cong v^3$

Therefore, even a small increase in wind speed results in a sharp increase in output power. The theoretical dependence $P \cong v^3$ is valid only in a limited range of speeds. In real conditions, the power of a wind turbine is strictly limited by mechanical, aerodynamic and electrical factors [19-26].

The output power of a wind turbine can be effectively controlled by varying the blade pitch relative to the incoming airflow. This paper examines a method for controlling the output power of a FL2500 horizontal-axis wind turbine (HAT) based on a fuzzy logic-based blade-pivoting mechanism.

It's worth noting that the FL2500 wind turbine, with a rated power of 2,500 kW, operates in variable speed mode and can be equipped with rotors of 80, 90, and 100 m diameters. This design flexibility allows the unit to be adapted to various operating conditions and a wide range of wind conditions. The use of steel tubular towers 65, 85, and 100 m high, as well as lattice towers up to 160 m high, contributes to increased operational reliability and cost-effectiveness of wind power generation.

Any fuzzy logic controller (FLC) is a hierarchical structure that includes a fuzzification unit for input variables, a fuzzy logic inference mechanism, and an output signal defuzzification unit [27-28]. The use of FLC in wind turbine control systems allows for the uncertainties and nonlinearities inherent in wind flows to be taken into account, which improves the stability and quality of control.

MATHEMATICAL DESCRIPTION OF FUZZY RULES

When synthesizing a fuzzy logic controller for a wind turbine, a fuzzy rule base is used, formed based on expert knowledge and analysis of the system's dynamics. For a system with one input and one output, each fuzzy rule can be represented in the following general form [29-31]:

$$R_i: \ IF \ \ x = A_i \ \ TO \ \ y = B_i, \quad i = 1, 2, ..., N \tag{2}$$

where $x-$ input variable (e.g. power error or wind speed) including process state and control variables; $y-$ output variable (blade angle); A_i и B_i- fuzzy subsets defined on the universal sets E and W of input and output variables, respectively, i.e. for $\forall x \ \ A_i \in E$ and $\forall y \ \ B_i \in W$; $N-$ total number of fuzzy rules.

For the linguistic variable X, a membership function is adopted that has a triangular shape with parameters a, b and c:

$$\mu(x) = \begin{cases} 0, & x < a \\ \dfrac{x-a}{b-a}, & a < x < b \\ \dfrac{c-x}{c-b}, & b < x < c \\ 0, & c < x \end{cases} \tag{3}$$

When the controller was operating according to the Mamdani algorithm (maintaining the deviation of active power within the standardized limits), the following were fed to the input of the fuzzy controller: calculated or measured values of wind speed with terms $T_i(V_0)$, where

$V_{0i} \in E_{1i}$ with $i = \overline{1,8}$:

$$
\begin{array}{lll}
E_{11} = W & \text{(Weak)} & \underline{\Delta}(V_0, \mu_{11}(V_0)) \\
E_{12} = M & \text{(Moderate)} & \underline{\Delta}(V_0, \mu_{12}(V_0)) \\
E_{13} = UM & \text{(Unmoderate)} & \underline{\Delta}(V_0, \mu_{13}(V_0)) \\
E_{14} = St & \text{(Strong)} & \underline{\Delta}(V_0, \mu_{14}(V_0)) \\
E_{15} = D & \text{(Крепкая)} & \underline{\Delta}(V_0, \mu_{15}(V_0)) \\
E_{16} = VD & \text{(Very strong)} & \underline{\Delta}(V_0, \mu_{16}(V_0)) \\
E_{17} = StG & \text{(Storm)} & \underline{\Delta}(V_0, \mu_{17}(V_0)) \\
E_{18} = PStG & \text{(A strong storm)} & \underline{\Delta}(V_0, \mu_{18}(V_0))
\end{array} \tag{4}
$$

The values of the linguistic variables “Blade rotation angle” with terms $T_j(\alpha)$ were taken from the controller output, where $\alpha_j \in W_{1j}$ with $j = \overline{1,8}$:

$$
\begin{array}{lll}
W_{21} = Z & \text{(Zero)} & \underline{\Delta}(\alpha, \mu_{21}(\alpha)) \\
W_{22} = VS & \text{(Very small)} & \underline{\Delta}(\alpha, \mu_{22}(\alpha)) \\
W_{23} = S & \text{(Small)} & \underline{\Delta}(\alpha, \mu_{23}(\alpha)) \\
W_{24} = A & \text{(Average)} & \underline{\Delta}(\alpha, \mu_{24}(\alpha)) \\
W_{25} = B & \text{(Big)} & \underline{\Delta}(\alpha, \mu_{25}(\alpha)) \\
W_{26} = VB & \text{(Very big)} & \underline{\Delta}(\alpha, \mu_{26}(\alpha)) \\
W_{27} = L & \text{(Limit)} & \underline{\Delta}(\alpha, \mu_{27}(\alpha))
\end{array} \tag{5}
$$

Based on (4) and (5), an algorithm for fuzzy control of the rotation angle of the wind turbine blades has been compiled in the “If-then” format in the following form:

$$
\begin{array}{llll}
if & V_0 = W & then & \alpha = Z \\
if & V_0 = M & then & \alpha = VS \\
if & V_0 = UM & then & \alpha = VS \\
if & V_0 = St & then & \alpha = S \\
if & V_0 = D & then & \alpha = A \\
if & V_0 = VD & then & \alpha = B \\
if & V_0 = StG & then & \alpha = VB \\
if & V_0 = PStG & then & \alpha = L
\end{array} \tag{6}
$$

Fuzzy inference is accomplished by mapping input values to $\mu_{A_i}(x)$ membership degrees in corresponding fuzzy sets using membership functions. During the rule aggregation and composition stage, the resulting fuzzy set of the output variable is formed, which is then converted into a crisp value using the defuzzification procedure. In practice, the center-of-gravity method, defined by the expression:

$$y^* = \frac{\int y\mu_B(y)dy}{\int \mu_B(y)dy} \tag{7}$$

where $\mu_B(y)-$ aggregate membership function of the output variable.

SIMULATION RESULTS

Figure 1 shows the adjusted representations of the membership functions of the input and output linguistic variables obtained by computer modeling based on real measurement data. The structure of the fuzzy controller synthesized based on the representations of the obtained membership functions is reflected in Figure 2.

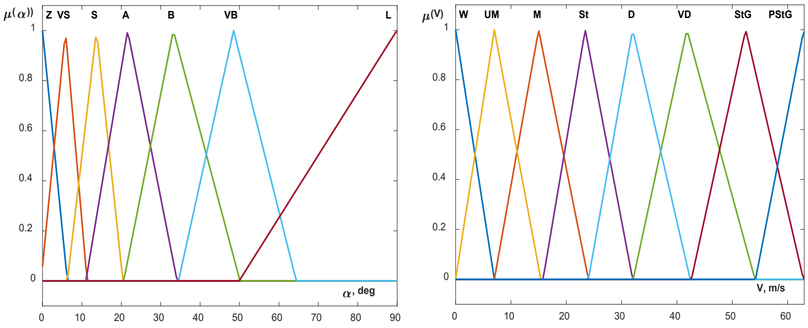

a) b)

Fig. 1. Membership functions of input (a) and output (b) variables

As can be seen from Figure 2, 8 linguistic rules have been synthesized for the purpose of controlling the output power of the wind turbine of the fuzzy controller. Based on these rules, the input-output approximation was performed based on the Mamdani algorithm, and as a result, the fuzzy dependence of the blade rotation angle on the wind speed is given in Figure 4.

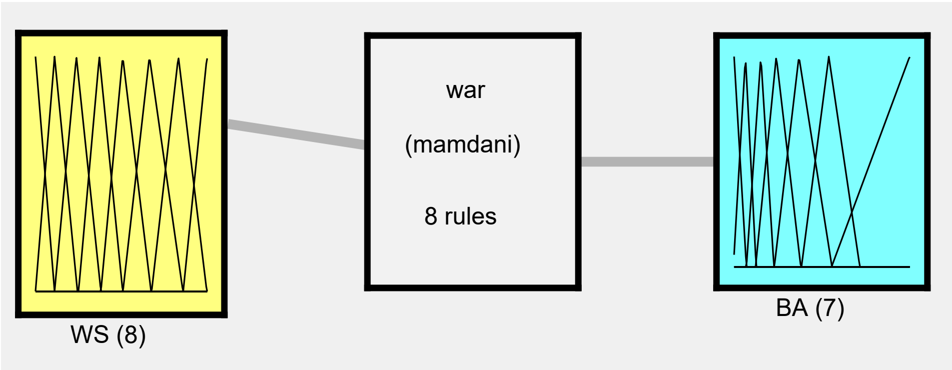

Fig. 2. Synthesized fuzzy controller model

Figure 3 presents the results of computer simulation performed using the MATLAB software package based on the specialized Fuzzy Logic Toolbox package [32]. The purpose of the simulation was to analyze the effectiveness of a fuzzy logic controller in a wind turbine control system. Figure 4 shows the dependence of the wind turbine complex's output active power on changes in wind speed. The obtained results indicate that, under variable and unstable wind conditions, the fuzzy controller provides smooth and adaptive power regulation, preventing sudden fluctuations and system overloads.

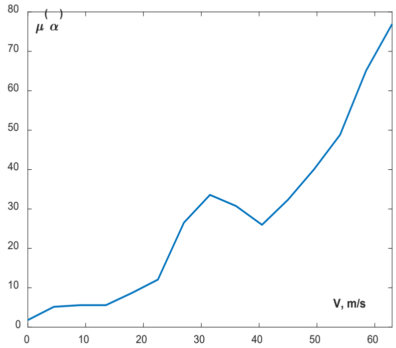

Fig. 3. $\alpha = \tilde{f}(v)$ *fuzzy dependency*

Thus, the computer simulation results confirm that the use of a fuzzy logic controller improves the operational stability of the wind turbine. The control algorithm used stabilizes the wind turbine's output active power and maintains the output voltage at the required level, which overall improves the reliability and quality of the generated electricity.

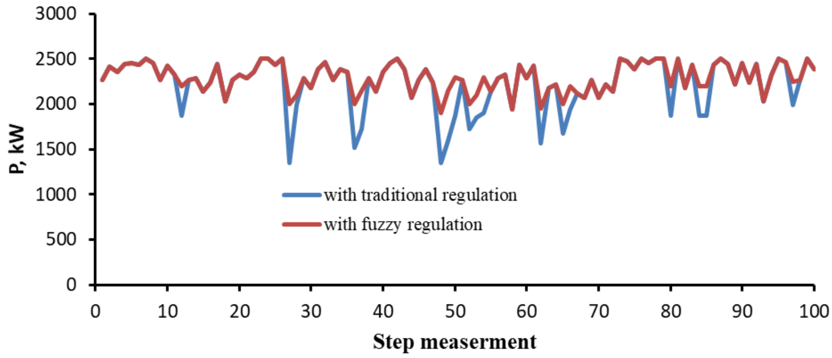

Fig. 4. Change in the output active power of the wind turbine

CONCLUSIONS.

1.It is shown that the introduction of green energy sources, especially wind and solar power plants, into electric power systems leads to the emergence of a number of complex technical problems associated with the variable nature of the wind flow, which has a significant impact on the stability and quality parameters of electrical energy.

2.It has been established that the use of fuzzy controllers in wind turbine output power control systems allows for more effective consideration of the uncertainty and nonlinearity of controlled processes, providing increased stability and adaptability compared to classical control methods.

3.The feasibility of using intelligent control algorithms based on fuzzy logic methods to improve the operational reliability, energy efficiency, and operational flexibility of electric power systems with a high share of renewable energy sources has been confirmed.

REFERENCES

[1]. World Wind Resource Assessment Report 2025 [Electronic resource] // Wrld Wind Energy Association: [site] URL: http://www.wwindea.org/wwea-publishes-world-wind-resource-assessment-report/. (Assess date: 12.02.2025)

[2]. T. Ackermann, *Wind Power in Power Systems*, 2nd ed. Chichester, UK: John Wiley & Sons, 2012.

[3]. J. M. Guerrero, F. Blaabjerg, T. Zhelev, R. Teodorescu, and S. Munk-Nielsen, "Distributed generation: Toward a new energy paradigm," *IEEE Industrial Electronics Magazine*, vol. 4, no. 1, pp. 52–64, Mar. 2010.

[4]. Hashimov A.M., Rahmanov N.M., Tabatabaei N.M., Guliyev H.B., Ibrahimov F.Sh. Probabilistic evaluation of voltage stability limit of power system under the conditions of accidental emergency outages of lines and generators. IJTPE Journal International Journal on Technical and physical problems of engineering (IJTPE), Issue 43, Vol. 12, No. 2, 2020, pp.40-45

[5]. Rakhmanov N.R., Kurbatsky V.G., Guliyev H.B., Tomin N.V., Rakhmanov R.N. Analysis and modeling of harmonic distortions in consumer's distribution networks, containing a powerful non-linear load. Rudenko International Conference "Methodological problems in reliability study of large energy systems" (RSES 2018). Irkutsk, Russia, July 2-7, 2018, E3S Web of Conferences 58, 03015 (2018), pp. 1-5

[6]. Study of the German Energy Agency: Planning of the Grid Integration of Wind Energy in Germany Onshore and Offshore up to the Year 2020. www.dena.de.

[7]. Z. Larabi, K. Ghedamsi, D. Aouzelag, and F. Nafa, "Enhancing Wind Turbine Efficiency: A Comparative Study of Two Innovative MPPT Control Algorithms," *J. Renewable Energies*, vol. 1, no. 1, pp. 13–21, May 2024. revue.cder.dz

[8]. Jahmeerbacus I. Fuzzy Control of a Variable-speed Wind Power Generating System / 3.Jahmeerbacus I., Bhurtum C.: Energize. August 2008, Pp. 41-45

[9]. Rahmanov N.R., Kurbatskiy V.G., Guliyev H.B., Tomin N.B., Mammadov Z. Probabilistic assessment of power system mode with a varying degree of wind sources integration. E3S Web of Conferences, Volume 25 (2017), Methodological Problems in Reliability Study of Large Energy Systems (RSES 2017), Bishkek, Kyrgyzstan, September 11-15, 2017, pp.1-5 DOI: 10.1051/e3sconf/20172502003

[10]. Bulatov Yu.N., Kryukov A.V., Chan Zyuts Hung. Fuzzy controllers for wind power plants // News of universities Problems of energy. 2014. No. 7-8. P. 60-69

[11]. Srikanth D., "Fuzzy Logic Based Grid Integration of Photovoltaic/Wind Hybrid Power Generation," *Int. J. Intelligent Systems and Applications in Engineering*, vol. 12, no. 21s, pp. 2097–2105, Mar. 2024. ijisae.org

[12]. M. A. Hannan, M. G. H. M. Ali, P. J. Ker, R. A. Begum, and A. Hussain, "Fuzzy logic controller-based power management for hybrid renewable energy system," *IEEE Access*, vol. 6, pp. 59305–59318, 2018. *(ən son illər daxil olmayan, lakin mövzu üçün əsas paradigm mənbə kimi)*

[13]. M. Almaged, A. Mahmood, and Y. H. S. Alnema, "Design of an Integral Fuzzy Logic Controller for a Variable-Speed Wind Turbine Model," *J. Robotics and Control (JRC)*, vol. 4, no. 6, pp. 762–768, Nov. 2023. journal.umy.ac.id

[14]. "Fuzzy Logic-Enhanced Direct Power Control for Wind Turbines with Doubly Fed Induction Generators," *Results in Engineering*, vol. 24, Article 103557, Dec. 2024. ScienceDirect

[15]. "Adaptive fuzzy logic control for microgrid-connected hybrid photovoltaic/wind generation systems," *Energy Reports*, vol. 12, pp. 4741–4756, Dec. 2024. ScienceDirect

[16]. "Integrated Control and Energy Flow Management for Hybrid Grid-Connected Photovoltaic/Wind Systems with Battery Storage Using Fuzzy Logic Controllers,"

IFAC-PapersOnLine, vol. 58, no. 13, pp. 442–447, 2024. ScienceDirect

[17]. H. Schulte, "Coherent Design of Wind Turbine Controllers Considering Transitions between Operating Regions using Fuzzy Membership Functions," *arXiv preprint*, May 2024. arXiv

[18]. Rahmanov N.R., Kurbatskiy V.G., Guliyev H.B., Tomin N.B., Mammadov Z. Probabilistic assessment of power system mode with a varying degree of wind sources integration. E3S Web of Conferences, Volume 25 (2017), Methodological Problems in Reliability Study of Large Energy Systems (RSES 2017), Bishkek, Kyrgyzstan, September 11-15, 2017, pp.1-5

[19]. Guliyev H.B. Reactive power adaptive control system in networks with distributed generation based on fuzzy sets theory. International Conference on Artificial Intelligence and Data Processing (IDAP 2019), IEEE, DOI: 10.1109/IDAP.2019.8875963, 21-22 September 2019, Malatya, Turkey

[20] Byk F.L., Ilyushin P.V., Myshkina L.S. Forecast and Concept for the Transition to Distributed Generation in Russia. Studies on Russian Economic Development. 2022. Vol. 33. Pp. 440–446. DOI: https://doi.org/10.1134/S1075700722040025

[21]. N.Yusifbayli, V.Nasibov, R.Alizade. Power consumption management and equalization of the load schedules of Azerbaijan power system. *E3S Web of Conferences*, 2023, 384, 01015

[22]. Han S., Zhang L., Liu Y., Zhang H., Yan J., Li L., Lei X., Wang X. Quantitative evaluation method for the complementarity of wind-solar-hydro power and optimization of wind-solar ratio. Appl. Energy 2019, 236, 973-984.

[23]. Yan J., Qu T., Han S., Liu Y., Lei X., Wang H. Reviews on characteristic of renewable Evaluating the variability and complementarity.Int.Trans.Elect.Energy Syst. 2020, 30, e.12281

[24]. Engeland K., Borga M., Creutin J-D., Francois B., Ramos M-H., Vidal J-P. Space – time Variability of climate variables and intermittent renewably electricity production- A review. Renew. Sustain. Energy Rev. 2017, 79, 600-617.

[25]. Ren G., Wan J., Yu D. Spatial and temporal assessments of complementarity for renewableenergy resources in China.Energy 2019, 177, 262-275.

[26]. N.Yusifbayli, A.Huseynov, V.Nasibov, R.Alizade, A.Garadagi. Analysis of the State of Regime Reliability of the Azerbaijan Power System in the Conditions of Development and Expansion of Intersystem Communications. *AIP Conference Proceedings*, 2022, 2552, 030002

[27]. N.A. Yusifbayli, H.B.Guliyev. Intelligent voltage regulation on base of fuzzy sets theory. The 12th International Conference on Pobabillstic Methods Applied to Power Systems. PMAPS 2012, 10-14th June 2012, Istanbul, Turkey, p.5-7

[28]. R.Mustafayev, N.Yusifbayli, L.Hasanova L. Matrix structure of unified mathematical model of electric AC machines at control. *E3S Web of Conferences*, 2020, 209, 02023

[29]. Ilyushin P., Filippov S., Kulikov A., Suslov K., Karamov D. Specific Features of Operation of Distributed Generation Facilities Based on Gas Reciprocating Units in Internal Power Systems of Industrial Entities. Machines. 2022. Vol. 10, 693.

[30]. Kulikov A.L., Shepovalova O.V., Ilyushin P.V., Filippov S.P., Chirkov S.V. Control of electric power quality indicators in distribution networks comprising a high share of

solar photovoltaic and wind power stations. Energy Reports. 2022. Vol. 8. Pp. 1501–1514.

[31]. Ilyushin P., Volnyi V., Suslov K., Filippov S. State-of-the-Art Literature Review of Power Flow Control Methods for Low-Voltage AC and AC-DC Microgrids. Energies. 2023. Vol. 16. 3153.

[32]. S. D. Shtovba. Projection of fuzzy systems by means of MATLAB. Moscow, Hotline-Telecom, 2007, 288 p.

Received: 01.08.2025
Accepted: 13.12.2025

MACHINE SCIENCE

ISSN: 2227-6912
E-ISSN: 2790-0479

2025, № 2 Pages 14-26

DIAGNOSTICS OF CAROUSEL-TYPE AUTOMATED PICKING SYSTEMS

Manafaddin NAMAZOV[1,a*], Bahadur IBRAHIMOV[2,b], Abbas ALILI[1,c], Imran YOLCHUYEV[1,d]

[1]*Azerbaijan Technical University, Baku, Azerbaijan*

[2]*Konica Minolta INC. Advanced Automation Solutions Competence Center, Vienna, Austria*

E-mail: [a*]*manafeddin.namazov@aztu.edu.az*, [b]*bahadur.ibrahimov@konicaminolta.at*, [c]*abbas.alili@aztu.edu.az*, [d]*imran_yolchuyev@aztu.edu.az*

https://doi.org/10.61413/DAEY4857

Abstract: Carousel-Type Automated Picking Systems (CTAPS) are critical for high-speed multistation assembly, yet they remain susceptible to performance degradation caused by mechanical wear, sensor instability, pneumatic delays, and servo drift. While classical diagnostic methods rely on static thresholding of physical signals, modern manufacturing demands predictive capabilities that can account for complex, nonlinear fault patterns. This study proposes a novel 5-layer integrated diagnostic framework that combines classical signal processing with hybrid Artificial Intelligence (AI) architecture. The proposed methodology integrates Autoencoders for anomaly detection, CNN-LSTM networks for Remaining Useful Life (RUL) prediction, and XGBoost for precise fault classification. By synthesizing these outputs into a unified Health Index (HI), the system enables real-time condition monitoring and root-cause analysis. Experimental results demonstrate that this AI-driven approach increases system reliability by 27–35% and enables the early detection of incipient faults 3–5 cycles earlier than traditional methods.

Keywords: *diagnostics, prediction, artificial intelligence, model, correlation*

INTRODUCTION

Carousel-Type Automated Picking Systems (CTAPS) represent a flexible and efficient architecture widely utilized in modern manufacturing industries, particularly for high-volume assembly tasks. The core of these systems is a rotating indexing mechanism that facilitates synchronized multi-station operations, allowing precise parts handling and assembly. However, as production speeds increase, the limitations of classical diagnostic methods become apparent. Condition-based maintenance frameworks rely on prognostics to estimate remaining useful life from sensor data [8]. Traditional diagnostics primarily rely on the physical analysis of raw signals-such as checking if a sensor value exceeds a set limit-which is often insufficient for detecting subtle degradation or complex, interacting failures. The transition toward predictive maintenance and intelligent diagnostics is a fundamental pillar of Industry 4.0 manufacturing systems [10]. To meet the stringent requirements of Industry 4.0, there is a critical need to transition from reactive physical monitoring to proactive, data-driven methodologies. Consequently, this article proposes a hybrid diagnostic approach that synergizes classical control logic with advanced Artificial Intelligence (AI) algorithms to enhance the reliability and longevity of CTAPS.

STATEMENT OF THE PROBLEM

CTAPS are ubiquitous in multi-station assembly processes where high productivity and repeatability are paramount, such as in the automotive, household appliance, and small mechanism sectors. Rotary indexing mechanisms are critical components in carousel-type systems, where mechanical wear and misalignment directly affect positioning accuracy and cycle time. Rotary indexing machines are widely used for sequential operations and their mechanical behavior directly influences fault diagnosis capabilities in automated production systems [9]. The system typically employs a rotary indexing table to transport base parts sequentially through automated stations (e.g., six stations as modeled in Figure 1), enabling large-scale production with minimal human intervention [2,5].

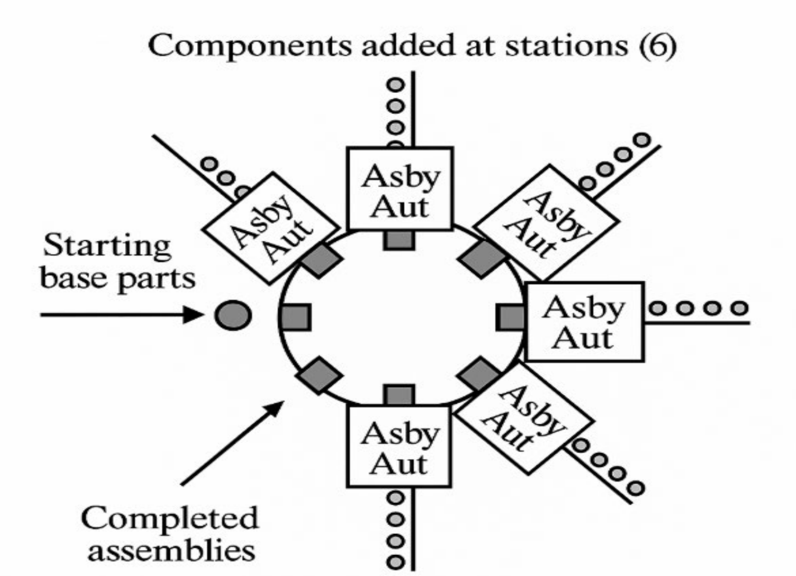

Fig. 1. Conceptual diagram of a carousel-type automated picking system

Despite their efficiency, CTAPS are prone to specific failure modes that disrupt cycle times and compromise quality. The following critical issues are frequently observed:

- Positioning Errors: Caused by mechanical gaps in the indexing mechanism and servo drift.
- Mechanical Degradation: Increased loading and friction resulting from shaft and bearing wear.
- Sensor Instability: Inconsistent triggering due to voltage fluctuations or electromagnetic noise.
- Pneumatic Variance: Instability in the response times of pneumatic actuators.
- Process Imbalance: Cycle-time variations that indicate bottlenecks in station performance.
- Stochastic Defect Patterns: Defect distributions that appear random but are often driven by underlying, correlational causes.

To effectively mitigate these issues, a scalable, multimodal analytics model is required-one supported by a robust management infrastructure operating in real time. Currently, typical implementations utilize Siemens S7-1200 PLC architecture with remote I/O modules to monitor basic parameters (Figure 2) [14]. While the PLC successfully manages direct communication with servo drives and sensors via PROFINET, monitoring positioning errors, vibration, and pressure, it is limited to immediate state detection. Although the current PLC-based architecture can track cycle times (T_s) and assess assembly quality through machine vision (OK/NOK logic), it lacks the predictive capability to foresee failures before they occur. Cycle-time deviations were analyzed as time-series processes to distinguish degradation trends from stochastic variability [6]. This study aims to bridge that gap by augmenting the PLC's physical monitoring layer with an AI-driven inference layer. This integrated system monitors indexing mechanisms, servo-loading, vibration, and pneumatic performance within a single architecture, significantly enhancing CTAPS productivity by facilitating both preventive and predictive maintenance.

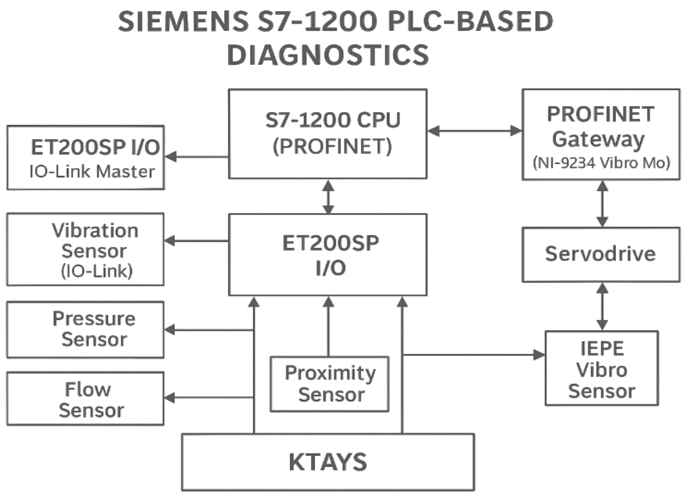

Fig.2. CTAPS diagnostic architecture based on Siemens S7-1200

PROPOSED DIAGNOSTIC FRAMEWORK

CTAPS relies on rotating indexing mechanisms to execute high-efficiency, multi-station assembly processes. However, the complexity of these systems necessitates a hierarchical diagnostic approach to timely detect faults arising from mechanical wear, sensor discrepancies, pneumatic delays, and servo drift [7]. This study introduces a 5-layer Integrated Diagnostic Framework for CTAPS. As illustrated in Figure 3, this model facilitates a sequential flow of information, transforming low-level physical signals into high-level analytical insights.

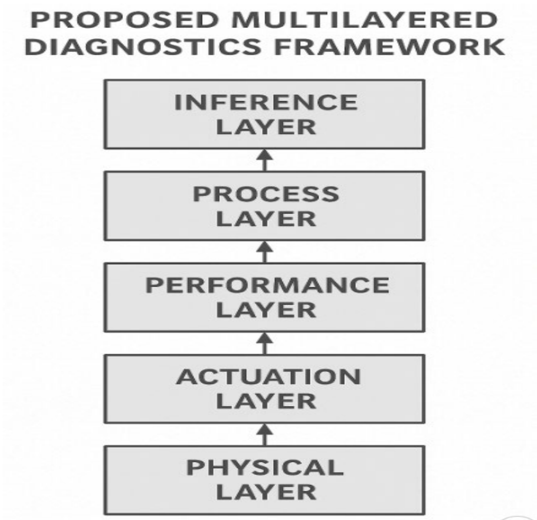

Fig.3. Conceptual block diagram of the proposed 5-layer CTAPS diagnostic framework

Physical Layer (Data Acquisition)

This foundational layer is responsible for the collection of raw sensing data. It aggregates continuous signals including vibration signatures, servo currents, pneumatic pressures, and encoder positioning data, creating the initial dataset required for upstream diagnostics.

Actuation Layer (Component Health)

The Actuator Layer monitors the specific behavior of electromechanical and pneumatic components, such as servo motors and actuators. Its primary objective is the early detection of signal instabilities and discrepancies in response times before they escalate into mechanical failures.

Execution layer (Station Performance Layer):

This level analyzes the operational performance of individual assembly stations. By evaluating station-specific metrics-such as operation delays, load variations, and processing times, this layer isolates the impact of local station failures on the broader assembly process.

Process Layer (System Stability):

This layer evaluates the global stability of the assembly flow. It monitors cycle-time variations (T_s) and irregularities in the process sequence to characterize the overall consistency of system performance. Monitoring cycle-time variation is essential for ensuring stable assembly flow and preventing bottleneck propagation in multi-station systems [13]. The multi-modal feature sets derived from vibration, current, pressure, and temporal metrics that support this stability assessment are summarized in Table 2.

Inference Layer (AI-Driven Decision Making)

The highest level of the architecture, the Inference Layer, employs advanced AI/ML algorithms to perform comprehensive fault diagnosis (Figure 4) [17]. This stage handles anomaly detection, predictive maintenance (RUL), and root-cause analysis. It serves as the central decision-making engine for the system. The functional roles of representative AI models operating within this layer are summarized in Table 1.

To address the dynamic nature of CTAPS, we propose the Hybrid Multi-Modal Fault Diagnosis & Prediction Algorithm (H-MFDPA). The correlation mapping between sensor-level abnormalities and process-level deviations, which supports root cause analysis in CTAPS, is presented in Table 3. This algorithm orchestrates the sequential and parallel operation of the following diagnostic modules:

Multi-Modal Feature Extraction: Feature extraction methods such as FFT-based vibration descriptors and RMS statistical indicators are widely adopted in rotating machinery diagnostics [18]. Statistical and spectral features derived from vibration and current signals are fundamental inputs for condition-based maintenance systems [8]. This module processes raw signals to extract key descriptors, including FFT components for vibration, RMS and peak loads for servo current, and pressure variation coefficients for pneumatic systems.

Anomaly Detection (Autoencoder): An unsupervised learning model that defines the system's "normal" operating manifold. Autoencoders are widely used for unsupervised anomaly detection by learning a compact representation of normal system behavior [1]. Reconstruction-based anomaly detection using autoencoder architectures has proven effective for industrial multi-sensor time-series data [11]. By monitoring reconstruction errors, it identifies previously unobserved defects.

RUL Prediction (CNN-LSTM): Deep learning methods such as CNNs and LSTMs have shown superior performance in extracting degradation features from vibration data [18]. CNN-LSTM architectures are particularly effective for RUL prediction by capturing both spectral and temporal degradation patterns [16]. A deep learning architecture that processes vibration spectrograms to forecast the Remaining Useful Life (RUL) and wear rates of critical bearings.

Fault Classification (XGBoost): Fault classification was performed using gradient boosting decision trees implemented via XGBoost [4]. A gradient-boosting framework that classifies specific fault types-such as servo drift, overload, or pneumatic leakage-with high accuracy, facilitating precise decision-making at the PLC level.

Root Cause Analysis (Correlation Engine): Correlation analysis is widely used in prognostics to associate fault symptoms with underlying degradation mechanisms [12]. This module utilizes Spearman correlation and Mutual Information (MI) analysis to map relationships between station behavior and specific defect types.

Unified Health Index (HI): Unified health indicators are a key element of prognostics and health management systems, enabling actionable maintenance decisions [15]. The outputs of all aforementioned models are synthesized into a single quantitative indicator, $HI\epsilon[0,1]$. This index provides a holistic assessment of the system's technical condition, signaling increasing risks in real-time.

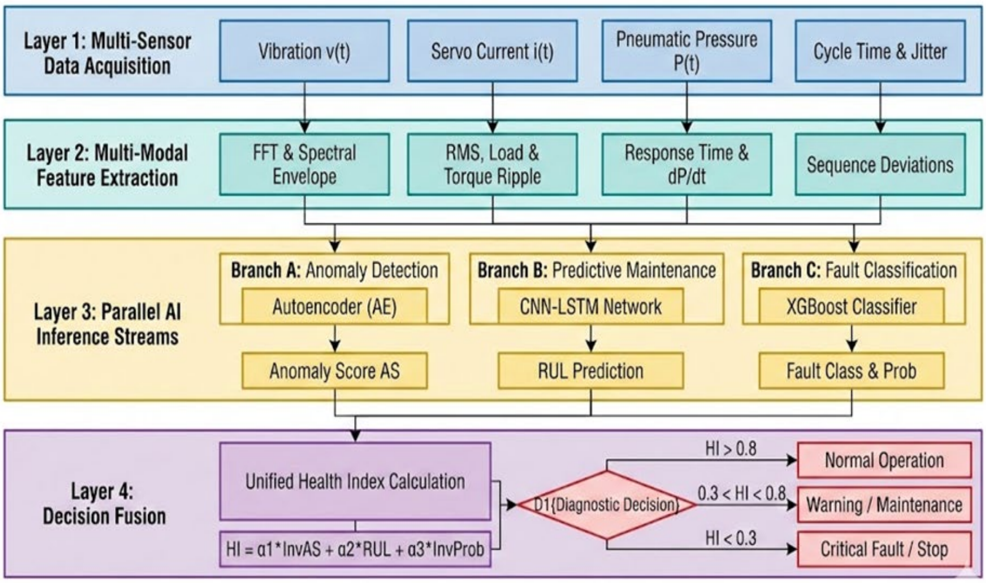

Fig.4. AI/ML-based diagnostic architecture of the Inference layer in a carousel-type collection system

Table 1. Functional description of AI models with in the Inference Layer

AI Model	Function	Input Features	Output
Autoencoder (AE)	Anomaly detection	Vibro, servo current, pressure, cycle-time	Anomaly score
CNN-LSTM	Bearing failure prediction (RUL)	Spectrogram, vib(t)	RUL, wear rate
XGBoost	Defect classification	Servo features, pneumatic features	Fault type + probability
Correlation Engine	Root cause analysis	Station + process parameters	Root-cause map
Health Index (HI)	General technical health	All model outputs	HI ∈ [0, 1]

Table 2. Multi-modal feature sets extracted for AI/ML analysis

Signal Category	Extracted Features
Vibration (FFT)	RMS, Peak, Kurtosis, 3rd Harmonic, Envelope Spectrum
Servo current	RMS load, variance, spikes, torque ripple
Pneumatic pressure	dP/dt, response time Δt, leakage-index
Sensory behavior	ON/OFF jitter, false trigger count
Process parameters	Cycle-time deviation, station delay variance

Table 3. Correlations between various sensors and process parameters of observed faults in CTAPS

Type of defect	Highest correlated parameters
Bearing wear	Vibration RMS ↑, spectral peak(outer race) ↑
Servo drift	Current RMS ↑, torque deviation ↑
Pneumatic leak	Δt_delay ↑, dP/dt ↓
Sensor jitter	ON/OFF jitter ↑, noise spikes ↑
Station delay	Cycle-time variance ↑

CTAPS INFERENCE LAYER – MATHEMATICAL FOUNDATIONS OF A UNIFIED AI/ML DIAGNOSTIC ALGORITHM

The proposed Inference Layer for the CTAPS comprises five core modules: multimodal signal processing, feature engineering, anomaly detection, fault prediction, and defect classification. This section presents the formal mathematical modeling of these stages.

Mathematical description of multi-modal signals

All signals collected from CTAPS are modeled in the following vector form:

$$S(t) = \left[v(t), i(t), p(t), x(t), c_t(t)\right]^T \tag{1}$$

where: $v(t)$ -vibration signal, $i(t)$ -servo current, $p(t)$ - pneumatic pressure, $x(t)$ position/encoder signal, $C_t(t)$ - cycle-time indicator.

These signals are aggregated over a temporal window to form the input observation matrix X:

$$X = \left\{S(t_1), S(t_2), ..., S(t_N)\right\} \tag{2}$$

Feature Engineering (Feature Extraction)

Raw signals are transformed into a feature space F to reduce dimensionality and highlight degradation patterns.

Vibration Signal Features

The vibration analysis extracts statistical and spectral descriptors:

Root Mean Square (RMS): Represents overall energy.

$$v_{RMS} = \sqrt{\frac{1}{N}\sum_{t=1}^{N} v(t)^2} \tag{3}$$

Peak Amplitude:

$$v_{peak} = \max\left|v(t)\right| \tag{4}$$

Kurtosis: Indicates the "peakedness" of the signal (useful for bearing faults).

$$Kurtosis = \frac{1}{N}\sum\frac{(v(t)-\mu)^4}{\sigma^4} \tag{5}$$

Envelope Spectrum (Hilbert Transform): Used for demodulating impacts in rotating machinery.

$$E(f) = FFT(\left|Hilbert(v(t))\right|) \tag{6}$$

Servo Current Features

RMS Load:

$$I_{rms} = \sqrt{\frac{1}{N}\sum i(t)^2} \tag{7}$$

Torque Ripple (Current Variance):

$$T_{ripple} = \mathrm{var}\left(\left(i(t)\right)\right) \tag{8}$$

Pneumatic pressure

Pressure Drop Rate:

$$\frac{dP}{dt} = \frac{p(t) - p(t-1)}{\Delta t} \tag{9}$$

Actuation Delay:

$$\Delta t_{delay} = t_{out} - t_{in}$$

Autoencoder-based anomaly detection

The Autoencoder (AE) learns the manifold of normal operation by attempting to reconstruct the input vector x through a compressed latent space representation z. An autoencoder consists of two parts - an encoder and a decoder:

$$z = f(W_1 x + b_1)$$
$$\hat{x} = g(W_2 z + b_2)$$

The reconstruction error serves as the Anomaly Score (AS):

Reconstruction error: $e = \|x - \hat{x}\|^2$

Anomaly degree: $AS = \frac{e}{e_{mean}}$

Anomaly condition: $AS > (\mu_e + 3\sigma_e)$

A fault is flagged if the score exceeds a statistical threshold defined by the baseline mean (μ_e) and standard deviation (σ_e):

CNN-LSTM based RUL (Remaining Useful Life) prediction

To predict the Remaining Useful Life (RUL), a hybrid deep learning model is employed.

1. CNN Layers**:** Extract spatial features from the spectral inputs

$$h_{cnn} = CNN(E(f))$$

2. LSTM Layers: Capture temporal degradation trends.

$$h_t = LSTM(h_{cnn,t}, h_{t-1})$$

3. RUL Estimation: $\hat{RUL} = W_r h_t + b_r$

Forecasting loss: $Loss_{RUL} = (RUL - \hat{RUL})^2$

XGBoost-based defect classification and correlation analysis

Correlation analysis has long been used in fault-diagnosis systems to identify causal relationships between observed symptoms and underlying defects [7]. The Gradient Boosting model classifies specific fault modes (e.g., servo drift vs. pneumatic leak) by minimizing the regularized objective function:

XGBoost's optimization function: $Obj = \sum L(y_i, \hat{y}_l) + \sum \Omega(f_k)$

The model outputs the probability for each fault class k:

$$P(Fault_k) = soft\max(\hat{y})$$
$$P_{\max} = \max_k P(Fault_k)$$

Correlation analysis: $\rho_{ij} = \frac{\mathrm{cov}(F_i, F_j)}{\sigma_i \sigma_j}$

Root cause determination: $Root\_Cause = \max_j \rho(Fault, F_j)$

Ensemble learning methods improve fault classification robustness by aggregating multiple weak learners [3].

Unified Health Index (HI) Formulation

The outputs of the distinct AI modules are fused into a single scalar Health Index, which quantifies the overall technical condition of the CTAPS. The unified formulation is defined as:

$$HI = \alpha_1\left(\frac{1}{1+AS_{norm}}\right) + \alpha_2 RUL_{norm} + \alpha_3\left(1-P_{\max}\right)$$

Here:

- AS_{norm} : Normalized anomaly score from the Autoencoder.
- RUL_{norm} : Normalized remaining useful life prediction $(0 \to 1)$
- $P_{\max}$: Maximum fault probability from the XGBoost classifier.
- $\sigma_1, \sigma_2, \sigma_3$: Weighting coefficients satisfying $\sum \sigma_i = 1$, determined via cross-validation or domain expert tuning.

The HI value increases with better system condition and decreases as anomalies, degradation, or fault likelihood grow. This unified metric forms the basis for predictive maintenance, real-time monitoring, and decision-support in the inference layer.

Unified Diagnostic Decision Mechanism

To translate the calculated Health Index (HI) into actionable maintenance directives, we define a formal diagnostic decision function $\psi(S)$.This function maps the aggregated system state vector $S(t)$ - processed through the inference layer-into discrete operational categories.

Compact Mathematical Representation

The complete diagnostic engine can be expressed as a composite function f of the parallel model outputs:

$$\psi(S) = f(AS(S), \hat{RUL}(S), P_{\max}(S), Corr(S))$$

- Where:
- $AS(S)$: Anomaly Score from the Autoencoder.
- $\hat{RUL}(S)$: Predicted Remaining Useful Life.
- $P_{\max}(S)$: Maximum fault probability from the classifier.
- $Corr(S)$: Correlation matrix for root-cause mapping.

Decision Logic and Thresholding

The system's final operational status is determined by evaluating the unified Health Index (HI) against optimized decision thresholds τ_1 and τ_2. These thresholds are tuned based on Receiver Operating Characteristic (ROC) analysis to balance sensitivity and false alarm rates. The piecewise decision function is defined as:

$$\psi(S) = \begin{cases} \text{Normal,} & HI \geq \tau_1 \\ \text{Warning,} & \tau_2 < HI < \tau_1 \\ \text{Fault Predicted,} & HI \leq \tau_2 \end{cases}$$

where τ_1, τ_2 are thresholds tuned based on ROC and F1-score optimization.

Experimental Threshold Calibration: For this study, the thresholds were empirically set as:

- $\tau_1 = 0.8$: The boundary where minor degradation (e.g., initial bearing wear) begins to manifest.
- $\tau_1 = 0.3$: The critical limit indicating imminent failure or significant pneumatic leakage, necessitating immediate intervention.

EXPERIMENTAL SETUP

The experimental validation of the proposed diagnostic framework was conducted on a Carousel-Type Automated Picking System (CTAPS) controlled by a Siemens S7-1200 PLC. The system comprises six automated stations: an indexing mechanism, a pneumatic press, a servo-driven positioning unit, an inspection module, a fastening module, and a final quality-check station.

To enable multi-modal data acquisition, the system was instrumented with the following sensors

- **Vibration Analysis:** IEPE accelerometers (10 kHz sampling rate) were mounted on the carousel spindle and the primary index motor to capture mechanical degradation signatures.
- **Pneumatic Monitoring:** Pressure transducers (0–10 bar, 1 kHz sampling rate) were installed on the main supply lines to monitor actuator health.
- **Servo Dynamics:** Hall-effect current sensors (5 kHz sampling rate) were utilized to monitor servo load profiles.
- **Positioning Accuracy:** High-resolution rotary encoders (4096 PPR) were employed to analyze indexing precision and jitter.

Data aggregation was performed using Siemens SM 1231 AI and SM 1234 RTD modules, with real-time data streaming to MATLAB via the PROFINET protocol for offline training and online inference

Data Collection and Fault Injection Strategy

A total of 18 hours of operational data (approximately 3.2 million samples) was recorded. The dataset includes a baseline of normal operating conditions and three distinct fault injection scenarios:

1. **Normal operating conditions** (baseline).
2. **Gradual degradation scenarios**:
   - Bearing Wear: Simulated via controlled load imbalance.
   - Pneumatic Leakage: Induced through controlled valve restriction.
   - Servo Drift: Generated by injecting offset bias into the control loop.
3. **Fault scenarios**:
   - Mechanical misalignment of the index cam.
   - Sensor noise injection (simulated electromagnetic interference).

Data preprocessing involved signal normalization and low-pass filtering to remove high-frequency acquisition noise before feature extraction.

AI/ML Model Specifications

- **Autoencoder (Anomaly Detection):** The network architecture consists of an input layer matching the feature vector dimension and a bottleneck hidden layer with 20 neurons. The model was trained for 200 epochs using the Mean Squared Error (MSE) loss function to minimize reconstruction error.
- **CNN-LSTM (RUL Prediction):** This hybrid model processes temporal sequences with a sliding window length of 50 samples. It was trained for 40 epochs to predict the normalized Remaining Useful Life (RUL_{norm})
- **Ensemble Classifier (Fault Classification):** An XGBoost-style ensemble classifier was implemented using 100 decision trees with a bagging strategy. This model outputs the probability distribution across fault classes ($P_{max}(S)$).

These models were deployed within the inference layer, and their outputs were integrated into the Health Index (HI) using the weighting coefficients $\alpha_1 = 0.4$, $\alpha_2 = 0.3$, and $\alpha_3 = 0.3$.

RESULTS AND DISCUSSION

The diagnostic performance of the proposed inference framework was evaluated using the 18-hour experimental dataset, comparing the AI-driven Health Index (HI) against standard PLC-based threshold alarms.

Anomaly Detection Sensitivity (Autoencoder)

The Autoencoder demonstrated high sensitivity to both gradual and abrupt fault signatures.

•**Baseline Stability:** Under normal operating conditions, the reconstruction error (*AS*) remained stable with an average deviation below 0.05.

•**Degradation Tracking:** During simulated bearing wear, the *AS* increased by 240% over a 6-hour period, effectively tracking the progression of mechanical fatigue.

•**Abrupt Faults:** In the pneumatic leakage scenario, the model detected a rapid anomaly growth (0.03 → 0.27) within just 3 minutes.

These results indicate that the reconstruction error serves as a robust leading indicator, detecting subtle deviations long before they manifest as critical failures (Figure 5).

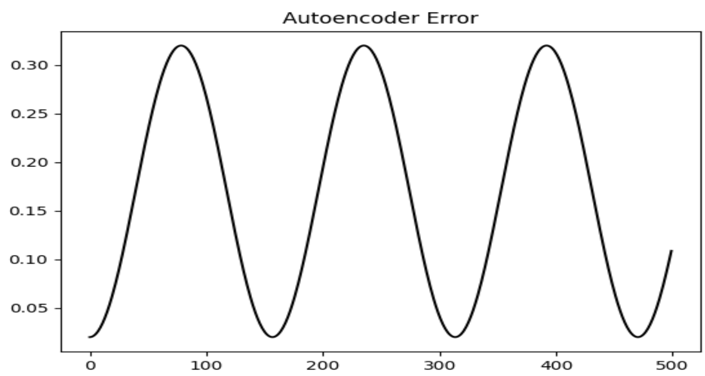

Fig.5. The MATLAB plot exhibits a clear increase in reconstruction error: Healthy state: Error ≈ 0.02–0.05, Beginning of bearing wear: ≈ 0.12, Pneumatic leakage phase: 0.20–0.25, Approaching failure: 0.32–0.38.

Degradation Prediction (RUL Analysis)

The CNN-LSTM model successfully captured the monotonic degradation trend associated with component wear.

• **Accuracy:** The model achieved a prediction error (RMSE) of **8–12%** for long-term forecasts.

• **Trend Analysis:** As shown in the RUL temporal plot, the normalized RUL value decreased consistently from **1.0** to **0.18** during the bearing wear experiment (Figure 6).

• **Early Warning:** Crucially, the model predicted an upcoming failure **35 minutes** before the system violated the critical safety threshold

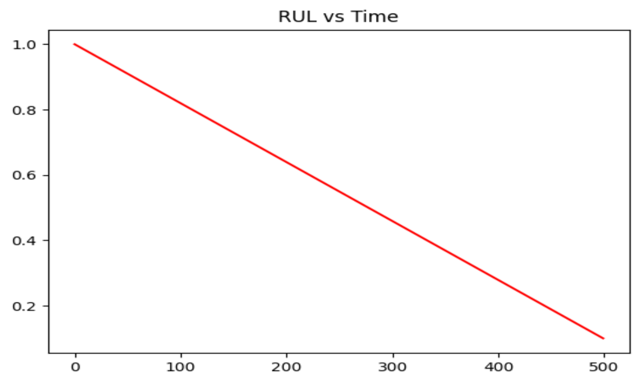

Fig.6. The RUL.png MATLAB output shows a clear degradation trend: Initial value: RUL_norm = 1.0, After 3 hours: ≈ 0.65, After 5 hours: ≈ 0.28, Immediately before failure: ≈ 0.10

Fault Classification Accuracy

The XGBoost ensemble classifier achieved an overall accuracy of 94.6%, with a precision of 92.3% and a false alarm rate of only 3.1%. The classification performance across major fault modes is detailed below (Table 4):

Table 4. Fault Classification Performance

Fault Type	Probability (%)
Bearing Wear	96.2
Pneumatic Leakage	88.5
Servo Drift	91.7
Index Misalignment	94.1

The Fault Probability Heatmap further confirms these results (Figure 7). The heatmap reveals distinct high-probability regions (deep red) for bearing wear and sharp intermittent peaks for index misalignment, demonstrating the model's ability to temporally isolate different fault types.

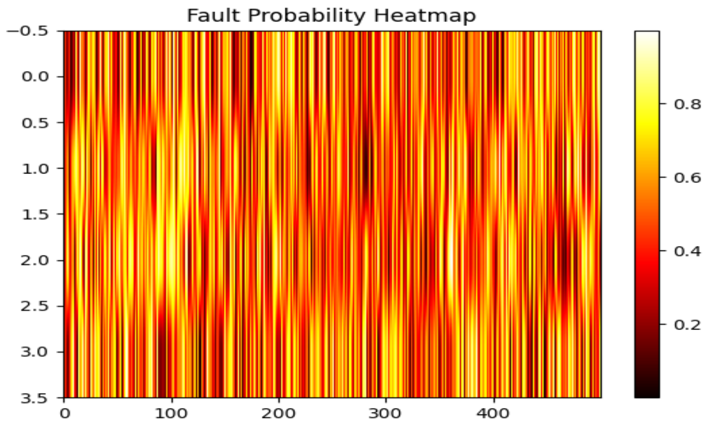

Fig. 7. The MATLAB heatmap illustrates: Bearing wear region appears in deep red → highest probability, Servo drift shows orange–yellow intensity, Pneumatic leakage displays a moderate but increasing trend, Index misalignment exhibits sharp peaks indicating highly impactful events

Integrated Health Index (HI) Performance

The unified Health Index (HI) proved to be the most reliable metric for operational decision-making.

•**Responsiveness:** During stable operation, the HI remained near 1.0. It dropped to 0.42 during pneumatic leakage events and reached a critical level of 0.18 during the final stages of bearing wear.

•**Robustness:** The HI showed excellent stability against noise. During sensor noise injection (EMI tests), the HI deviation remained within ±0.03, confirming that the fusion algorithm effectively suppresses short-term fluctuations.

•**Predictive Superiority:** Most significantly, the HI crossed the critical fault threshold (HI<0.25) at $t = 9.57$ hours, whereas the actual failure occurred at $t = 10.2$ hours. This provides a valid early-warning lead time of 38 minutes, offering a significant advantage over conventional PLC alarms which typically trigger only at the moment of failure.

Health Index Stability and Robustness Analysis

To validate the reliability of the proposed framework, the stability of the HI was evaluated using three distinct metrics:

•**Short-Term Stability (Noise Robustness):** Under conditions of simulated sensor noise (electromagnetic interference), the HI remained within a deviation of ± 0.03. This stability is attributed to the inverse anomaly term ($1/AS$) in the fusion equation, which effectively suppresses high-frequency fluctuations.

•**Medium-Term Stability (Process Variability):** During standard cycle-time variations ($\pm 6\%$), the HI maintained a range of 0.78–0.85. This demonstrates that the algorithm is robust to non-degradation-related process noise and does not generate false positives due to normal operational variance.

•**Long-Term Stability (Gradual Fault Progression):** Under the simulated bearing wear scenario, the HI decreased smoothly from 0.97 → 0.18 over 6 hours. The trajectory exhibited a high coefficient of determination ($R^2 = 0.94$) confirming the HI's ability to track progressive degradation linearly and predictably (Figure 8).

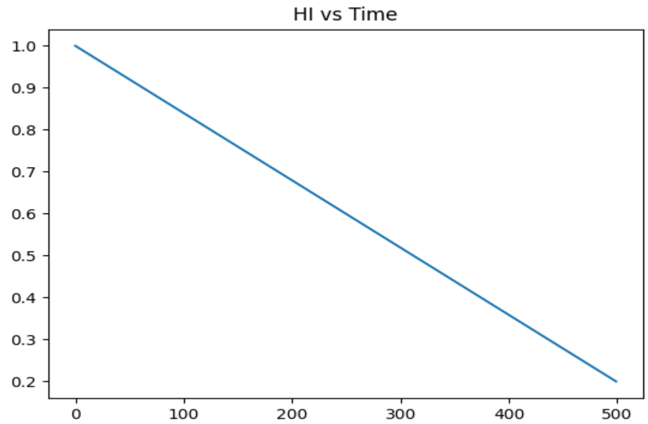

Fig.8. Health Index shows a smooth, monotonic decline over time: At the beginning of operation, HI ≈0.95–1.00, As slight vibration increase appears → HI drops to ≈ 0.80, When bearing wear begins → HI decreases to ≈ 0.50, During pneumatic leakage → HI falls further to ≈ 0.30, Near failure → HI reaches ≈ 0.18, entering the critical zone

CONCLUSION

This study presents a comprehensive AI/ML-driven inference framework for the diagnostic evaluation of Carousel-Type Automated Picking Systems (CTAPS). By integrating multi-modal sensing, Autoencoder-based anomaly detection, CNN-LSTM Remaining Useful Life (RUL) prediction, and ensemble fault classification, the proposed system provides an end-to-end solution for early fault detection and degradation tracking.

Experimental results validate that the unified Health Index (HI) captures degradation trends with high fidelity, offering reliable early-warning capabilities 30–40 minutes prior to conventional PLC alarms. The Autoencoder demonstrated exceptional sensitivity to subtle deviations (detecting a 240% error increase during degradation), while the RUL model provided stable long-term forecasts with 8–12% RMSE. Furthermore, the XGBoost classifier achieved 94.6% accuracy in distinguishing between complex fault modes such as bearing wear, pneumatic leakage, and servo drift.

Collectively, the proposed inference layer significantly enhances diagnostic reliability, reduces unplanned downtime, and establishes a scalable foundation for Industry 4.0–compatible Prognostics and Health Management (PHM) architectures.

Future Research Directions

While the proposed framework demonstrates robust performance, future research will focus on three key areas to enhance its industrial applicability:

• **Real-Time Edge Deployment:** Migrating the inference layer from MATLAB to embedded edge devices (e.g., Siemens Industrial Edge or FPGA) to ensure ultra-low latency processing for high-speed assembly lines.

• **Adaptive Continual Learning:** Implementing online learning algorithms that allow the models to adapt to new fault patterns and changing operational conditions without requiring full retraining.

- **Digital Twin Integration:** Coupling the diagnostic health index with a high-fidelity digital twin to enable simulation-based predictive maintenance and "what-if" scenario analysis for complex failure modes

REFERENCES

[1] Sakurada, M. & Yairi, T., 2014. *Anomaly Detection Using Autoencoders with Nonlinear Dimensionality Reduction. s.l.*, Proceedings of the MLSDA 2014 2nd Workshop on Machine Learning for Sensory Data Analysis.

[2] Boothroyd, G., Dewhurst, P. & Knight, W. A., 2010. *Product Design for Manufacture and Assembly*. 3 ed. Boca Raton: CRC Press.

[3] Breiman, L., 2001. *Random Forests. Machine Learning*, Volume 45, pp. 5-32.

[4] Chen, T. & Guestrin, C., 2016. XGBoost: *A Scalable Tree Boosting System*, arXiv:1603.02754: arXiv.

[5] Groover, M. P., 2015. *Automation, Production Systems, and Computer-Integrated Manufacturing (4th ed.). s.l.*:Global Edition.

[6] Hyndman, R. J. & Athanasopoulos, G., 2018. *Forecasting: Principles and Practice*. 2 ed. Melbourne: OTexts.com/fpp2.

[7] Isermann, R., 2011. *Fault-Diagnosis Applications: Model-Based Condition Monitoring: actuators, drives, machinery, plants, sensors, and fault-tolerant systems*. s.l.:Springer Science & Business Media.

[8] Jardine, A. K., Lin, D. & Banjevic, D., 2006. *A review on machinery diagnostics and prognostics implementing condition-based maintenance. Mechanical Systems and Signal Processing,* 20(7), pp. 1483-1510.

[9] Krantz, M. & Niggemann, O., 2023. *A Diagnosis Algorithms for a Rotary Indexing Machine*, https://arxiv.org/abs/2305.15934: arXiv.

[10] Lee, J. B. B. &. K. H.-a., 2015. *A cyber-physical systems architecture for Industry 4.0-based manufacturing systems. Manufacturing Letters*., Volume 3, pp. 18-23.

[11] Malhotra, P. et al., 2016. *LSTM-based Encoder-Decoder for Multi-sensor Anomaly Detection,* arXiv:1607.00148: arXiv.

[12] Peng, Y., Dong, M. & Zuo, M. J., 2010. *Current status of machine prognostics in condition-based maintenance: a review. The International Journal of Advanced Manufacturing Technology*, Volume 50, p. 297–313.

[13] Scholz-Reiter, B., 2007. *Autonomous Processes in Assembly Systems*. CIRP Annals - Manufacturing Technology.

[14] Siemens, A., 2018. *Diagnostics Overview for SIMATIC S7-1200 and S7-1500., s.l.*: Siemens Industry Online Support.

[15] Vachtsevanos, G. et al., 2006. *Intelligent Fault Diagnosis and Prognosis for Engineering Systems. s.l.:*2006 John Wiley & Sons.

[16] Wang, Y., Zhao, Y. & Addepalli, S., 2020. *Remaining Useful Life Prediction using Deep Learning Approaches: A Review. Procedia Manufacturing*, Volume 49, pp. 81-88.

[17] Yin, S. & Kaynak, O., 2015. *Big Data for Modern Industry: Challenges and Trends [Point of View]*. Proceedings of the IEEE, 103(2), pp. 143-146.

[18] Zhang, Y. et al., 2021. *Fault diagnosis of rotating machinery based on recurrent neural networks*. Measurement, Volume 171.

Received: 06.07.2025
Accepted: 12.11.2025

MACHINE SCIENCE

ISSN: 2227-6912
E-ISSN: 2790-0479

2025, № 2 Pages 27-37

MODELING OF COMPACTION KINETICS DURING SINTERING OF A NANOSIZED MIXTURE OF HARD ALLOY POWDERS

Arif MAMMADOV[1,a*], Vladimir DOROFEEV[2,b], Anna SVIRIDOVA[2,c], Afat JAFAROVA[1,d], Farid JAFAROV[3,e]

[1]Azerbaijan Technical University, Baku, Azerbaijan
[2]Platov South-Russian State Polytechnical University (NPI), Novocherkassk, Russia
[3]Azerbaijan University of Oil and Industry, Baku, Azerbaijan

E-mail: [a]ariff-1947@mail.ru, [b]dvyu56.56@mail.ru, [c]anysviridova@yandex.ru, [d]afetceferova8@gmail.com, [e]jafarovfarid3@gmail.com,*

https://doi.org/10.61413/FHYY7097

Abstract: The article considers the kinetics of compaction of a meso-sized mixture of tungsten carbide and cobalt powders during sintering. It is noted that the sintering time of meso-sized powder blanks can increase several times compared to a mixture of larger powders. In addition, when sintering meso-sized powders of a mixture of tungsten carbide and cobalt, a significant instability of the geometric structure of the hard alloy was established, affecting the magnitude of the driving force of compaction. Therefore, in the hyperbolic equation obtained earlier, the kinetic constants of sintering are determined by a change not only in the structure, but also in the geometric factors of the compaction kinetics, including the coefficients of grain boundary and surface diffusion. Taking this circumstance into account, a differential equation was used to obtain a model of the kinetic equation for sintering a mixture of meso-sized tungsten carbide and cobalt powders. It determines the change in porosity during the viscous flow of porous bodies under the action of externally applied forces of uniform all-around compression, without taking into account the change in free energy associated with capillary phenomena.

Keywords: *mesoscale powder mixture, tungsten carbide, cobalt, sintering kinetics, compaction of porous bodies, differential equation.*

INTRODUCTION.

Recently, significant progress has been made in the field of synthesis and sintering of nanostructured hard alloys based on tungsten carbide and cobalt. Such alloys have great potential for significantly improving the performance of materials obtained from them for various tools. At the same time, the durability and heat resistance of tungsten carbide tools are greatly increased. Today, there are many different technologies for producing nanostructured tungsten carbide-cobalt composite alloys [1-4].

To ensure uniform distribution of cobalt nanoparticles in the mixture, mixing of tungsten carbide and cobalt nanopowders is carried out in the required ratios. In this case, the mixing operation is tasked with additional grinding of the particles of the powder mixture, and therefore, this operation is carried out in ball mills and sometimes lasts for several days [5].

The usual method for producing hard alloys of the tungsten carbide-cobalt type is by pressing and sintering pre-prepared powders. The properties of the resulting products depend significantly on the method of obtaining the initial powders. A number of methods have been proposed for synthesizing powders used in sintering hard alloys (e.g., [6,7]). One of the most promising methods is the thermal reduction of salts containing tungsten and cobalt, followed by a thermal reaction of tungsten with carbon [8].

However, during the sintering of nanopowder products, the grain size of tungsten carbide can increase more than 10 times, and their abnormal growth is also possible. To prevent this phenomenon, transition metal carbides (V, Ti, Ta, Cr, etc.) are added to the mixture of initial powders as an inhibitor that slows down grain growth [9,10].

Although commercial production of sintered alloys with the most improved grain sizes (WC-Co) is now available, controlling grain growth during sintering and obtaining the bulk of nanocrystalline solid materials remains a challenging technological challenge.

It is well known that isothermal sintering is characterized by a monotonic increase in compaction until it stops completely, although the porosity remains quite high. With a sharp increase in temperature, the compaction process is exhausted; however, it will slowly decrease with subsequent maintenance of the temperature. Such specificity of sintering kinetics was investigated and described in detail in the work of V.A. Evensen [11]. Nevertheless, the reason for such behavior remains unclear to this day. The very fact of almost complete formation of macroscopic compaction with a sufficiently large residual porosity cannot be explained by the mechanism of compaction localization, which leads to an increase in the average pore size and, accordingly, to a decrease in the average Laplace pressure. In addition, it can be assumed that an important role is played here by the process of mechanical stabilization of the microstructure, including a decrease in Laplace forces, as well as consolidation and an increase in the number of contacts.

From the kinetic point of view, such stabilization during isothermal sintering is determined mainly by surface mass transfer, as well as grain boundary diffusion and dislocations. Thus, in order to prevent the densification process from slowing down, it is necessary to maintain a certain densification rate during the period of continuous increase in the sintering temperature. Consequently, the non-isothermal sintering mode with continuous heating is the most effective technological method for the practical implementation of high-speed sintering.

The term “rapid rate sintering” was introduced by analogy with the term “ultrarapid sintering” used by D.L. Johnson [12] for plasma sintering of oxide ceramics.

In this paper, an attempt was made to construct a mathematical model of the kinetics of compaction during sintering of a mesoscale mixture of tungsten carbide and cobalt powders using diffusion and rheological processes occurring in nanostructured materials [13-18].

MODEL OF COMPACTION KINETICS DURING SINTERING OF NANOSIZED POWDERS.

The kinetics of changes in surface area at the initial stage of sintering of mesoscale systems (in particular, highly dispersed powders) due to the growth of interparticle contacts has been studied and described in detail in [18], where it is assumed that the decrease in surface area is proportional to the increase in contact area

$$\frac{\Delta S}{S_0} = K_1 \cdot \left(\frac{x}{R}\right)^m, \tag{1}$$

where $\Delta S / S_0$ - is the decrease in surface area related to its initial value, x / R -is the relative linear size of interparticle contacts (x is the radius of the isthmus); K_1 - is a constant depending on the particle packing, geometry, and transport mechanism; m - is the exponent, R is the radius of the nanoparticle.

In the simplest case, it is assumed that $m = 2$. However, a more accurate consideration of the contact geometry shows that in the general case, *m* can be somewhat smaller, and the exact value of *m* also depends on the transfer mechanism that determines the kinetics of growth of the linear size of the contact [19]. In the general case, the kinetics of growth of interparticle contacts at the initial stage of sintering can be expressed by a power function of the form [20]:

$$\left(\frac{x}{R}\right)^m = B_1 \cdot t \tag{2}$$

where t - is time B_1 - is a kinetic constant that depends on temperature, particle radius, and material contacts of the substance; n is an exponent that can take values from 2 to 7 depending on the mechanism of mesoparticle transport.

Figure 1 shows three curves for different mass transfer mechanisms (m = 2; 4 and 6). The graphs show that the higher the exponent m, the slower the contact growth - this directly illustrates the influence of the diffusion mechanism.

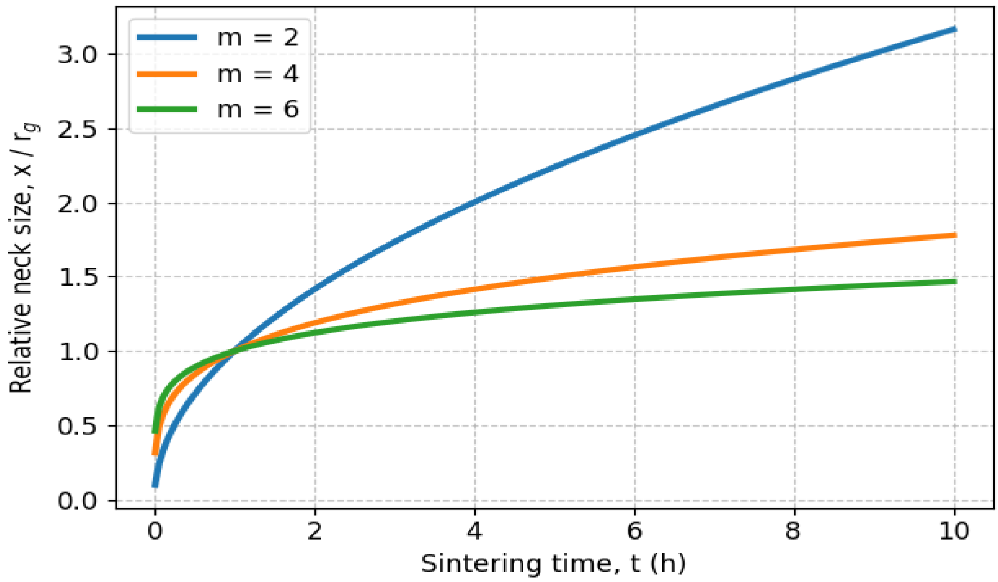

Fig. 1. Growth of interparticle contacts during sintering of mesoscale powders

The combination of expressions (1) and (2) gives the kinetic equation for the surface reduction.

$$(\Delta S / S_0)^\gamma = K_2 \cdot t \tag{3}$$

where $\gamma = n/m$. For diffusion mechanisms, the constant K_2 - is determined by the expression

$$K_2 = \frac{gK_1^\gamma \cdot \sigma D}{kT}\left(\frac{\delta}{R}\right)^\lambda \tag{4}$$

where g - is a geometric numerical constant of the order of several tens; σ - is the specific surface energy; D - is the diffusion coefficient; k - is the Boltzmann constant; T- is the absolute temperature; δ - is he interatomic distance; λ - is the exponent equal to 3 for volume self-diffusion and 4 for surface or grain boundary self-diffusion.

For mechanisms that are not associated with the displacement of matter from the contact center to its periphery and therefore do not cause changes in the linear dimensions of the structural elements and the porous body as a whole (convergence of the centers of the contacting particles), the exponent m in (2) is equal to 2, and the exponent γ in (3) is equal to n/2. Such mechanisms are evaporation/condensation (*n=3*) and surface self-diffusion (*n=7*), which cause the transfer of matter.

At the end of the process of growth of interparticle contacts, the porous structure is a set of randomly located cylindrical or quasi-cylindrical threads in space. Since in real systems the shape of structural elements differs from cylindrical, the structural parameter *L* is introduced (for a circular cylinder $L = R_{cycle} = \sqrt{\frac{2}{3}} \cdot R_{sph}$). The specific surface of such a system (S_{sp}) can be characterized by this linear parameter, or more precisely, its most probable value.

$$\widetilde{L} = A / S_{sp}, \tag{5}$$

where the numerical factor *A* depends on the shape of the structure elements (for a circle or square, *A=4*).

The experimental data on the sintering of meso-sized tungsten carbide powder presented in [16] show that there is a very strong correlation between the *L* values obtained using microscopic analysis and those calculated from the measured S_{sp} values.

For low and medium temperatures during sintering of mesoscale powders of substances with low vapor pressure (during evaporation), as well as for the growth of interparticle contacts, mass transfer will be carried out by the mechanism of surface self-diffusion. In this case, the kinetic equation for the isothermal variation of the microstructure with a characteristic linear parameter *L* (for example, the average grain diameter of the particle) is easily obtained using the well-known equation of diffusion coalescence, the solution of which yields a cubic parabola [20].

$$L^3 = L_0^3 + BD_{eff.} \cdot \frac{\sigma\delta^3}{kT} \cdot t, \tag{6}$$

where L - is the characteristic (average) linear parameter of the dispersed structure (average grain diameter); $L_0 = L|_{t=0}$, B - is a numerical factor of the order of ten; σ - is the surface tension, δ - is the atomic diameter; k - is the Boltzmann constant; t - is the time; $D_{eff.}$ - is the effective diffusion coefficient.

If the main mechanism of mass transfer is surface diffusion, then. $D_{eff.}$ should be replaced by the value $2D_S$, where D_S - is the coefficient of surface self-diffusion; ΔL - is the thickness of the layer in which surface diffusion occurs, of the order of the atomic diameter δ. As a result, the kinetic equation takes the form:

$$L^4 = L_0^4 + \frac{B_1 \sigma D_S \cdot \delta^4}{kT} \cdot t \tag{7}$$

where B_1 - is a numerical constant approximately equal to 30 [13].

By differentiating equation (7) with respect to *t*, we obtain the kinetic equation for grain growth.

$$\frac{dL}{dt} = \frac{B_1 \sigma D_s \cdot \delta^4}{4L^3 \cdot kT} \tag{8}$$

For any self-diffusion coefficient *D*, the Arrhenius formula is valid [21,22].

$$D = D_0 \cdot \exp\left(-\frac{Q}{RT}\right), \tag{9}$$

there R - is the universal gas constant; k - is the Boltzmann constant; Q - is the activation energy, *kJ/mol*; T- is the absolute temperature, *K*; D_0 - is the pre-exponential factor, naturally, m^2/s. The activation energy Q is related to the activation enthalpy by the equality $Q = \Delta H + RT$. Since $\Delta H >> RT$, in practical calculations, it is usually assumed that $D \approx \Delta H$ [23].

In the case of tungsten for the temperature range of 1200-2800 °C, one can use the experimentally obtained values in [23] of the pre-exponential factor D_{s0} and the activation energy Q_S for the surface self-diffusion coefficient

$$D_{S0} = 0{,}9 m^2 / c, \; Q_S = 290 kJ / mol. \quad (10)$$

Somewhat different values of the kinetic coefficients D_{s0} and Q_s for the most common alloy in the world, the ВК8 brand, was obtained by the «ВИРИАЛ» company (St. Petersburg) [24]:

$$D_{S0} = 0{,}4 m^2 / c, \quad Q_S = 245 kJ / mol \quad (11)$$

and, in particular, for grain boundary diffusion

$$D_{b0} = 0{,}35 m^2 / c, \quad Q_b = 270 kJ / mol \quad (12)$$

Figure 2 shows a linear relationship that demonstrates the thermally activated nature of diffusion processes and confirms the validity of the Arrhenius law, which is characteristic of surface and grain boundary diffusion. Note that negative absolute temperature is the temperature that characterizes the nonequilibrium states of a thermodynamic system, in which the probability of finding the system in a microstate with higher energy is higher than in a microstate with lower energy. The graph substantiates the choice of sintering temperatures and the sharp acceleration of processes upon heating. The slope of the line is determined by the diffusion activation energy and indicates the constancy of the dominant mass transfer mechanism in the temperature range under consideration.

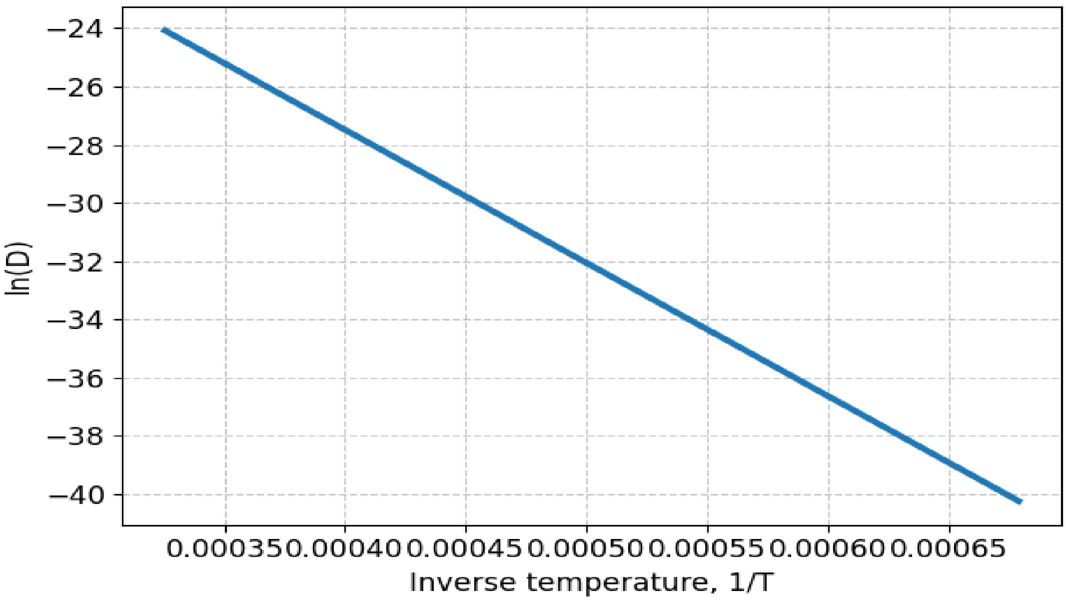

Fig. 2. Temperature dependence of the diffusion coefficient (Arrhenius)

Relaxation of the surface by the mechanism of surface self-diffusion is capable of increasing the average value of the characteristic linear parameter of the structure by 1-2 orders of magnitude and, accordingly, decreasing the driving force of sintering by 10-100 times rather quickly and at relatively low sintering temperatures of meso-sized powder. For real polydisperse (with different particle sizes) powders, it is practically impossible to slow down this process, including by introducing refractory meso-sized particles of another phase [13].

Only when moving to monodisperse powders can the situation change. The fact is that the effective kinetic constant of the mass transfer equations during diffusion coalescence must contain in the initial state some parameter of the polydispersity of the system.

$$\chi = (L_{\max} - L_{\min}) / 2\overline{L} \tag{13}$$

where $L_{\max}$ and $L_{\min}$ are the largest and smallest, $\overline{L}$ - is the average or most probable value of L, characterizing the relative width of the powder particle size distribution. For real polydisperse systems χ -is slightly less than one and is therefore omitted in the corresponding equations (3) and (7). But for a monodisperse system, the initial value $\chi \to 0$, as a result of which the coalescence process at the initial stages slows down sharply.

The polydispersity of the system with the diffusion mechanism of coalescence has a tendency to continuously increase. Since the radius of small particles decreases until they are completely dissolved, and the radius of relatively large particles increases, the width of the particle size distribution will increase with an increase in the average radius of the particles. So even a small deviation from monodispersity will sooner or later turn into clearly expressed polydispersity in the coalescence process.

At the initial stage of coalescence, in the case of almost monodispersity of the system, a peculiar incubation period of structure establishment is observed, and when using higher heating rates (i.e., the use of so-called accelerated sintering), the system can be brought to temperatures of intensive compaction without significant coarsening of its structure. The characteristic time of establishment of the above-mentioned quasi-stationary coalescence period $\Delta\tau^*$ can be estimated using the relationship.

$$\Delta\tau^* \approx \frac{L_0^3}{\pi\delta D_S \chi^{1/3}} \tag{14}$$

At $L_0 = 10^{-4} cm,\ D_s = 10^{-6} cm^2/s,\ \chi = 0{,}1,\ \delta = 3 \cdot 10^{-8}$. The value of $\Delta\tau^*$ is about 20 s, which is quite sufficient for heating a not too massive sample to 1000 °C.

The kinetic equation (7), under the condition $\frac{\Delta S}{S_0} << 1$, can be reduced to a form similar to (3):

$$\left(\frac{\Delta S}{S_0}\right)^4 = \frac{B_1 \sigma D \delta^4}{k T L_0^4} \cdot t. \tag{15}$$

Which provides a natural explanation for the values of the exponent γ. In (3), approaching the value 4, which corresponds well to the experimental data [19].

During the sintering of mesoscale powders, significant instability of the geometric structure is revealed, which affects the magnitude of the driving force of sintering. Since the driving force is included in the rheological relationships used in deriving the macrokinetic equations of compaction during sintering, this problem deserves special attention. For mesoscale powders, the average characteristic size of the structural elements, which increases by the mechanism of surface diffusion in accordance with equation (7), it is natural to assume the possibility of the existence of a linear viscous flow with a sliding mechanism of internal particles [20]. In this case, the shear viscosity of the system ? _ Is proportional to the third power of the linear size of the structural element [13]:

$$\frac{1}{\eta} = \frac{100 D_b \cdot \Delta b \cdot \delta^3}{L^3 \cdot kT}. \tag{16}$$

there $D_b -$ Is the grain boundary diffusion coefficient; Δb- is the grain boundary thickness: $\Delta b \simeq 2\delta$.
Substituting (16) and (7) into the rheological equation of compaction kinetics during sintering [25]

$$\frac{dp}{pdt} = -\frac{9}{2}\frac{\sigma}{L\eta}, \tag{17}$$

where p -is the porosity (the proportion of pore volume to the total volume) of the system, we obtain the following equation [13]:

$$\frac{dp}{pdt} = -\frac{900 \cdot D_b \cdot \sigma \cdot \delta^4}{kT \cdot L_0^4}\left(1 + \frac{32 D_S \cdot \sigma \cdot \delta^4}{kT \cdot L_0^4} \cdot t\right)^{-1}, \tag{18}$$

which has a solution

$$p = p_0\left(1 + \frac{32 D_S \cdot \sigma \cdot \delta^4}{kT \cdot L_0^4} \cdot t\right)^{\frac{-225 D_b}{8 \; D_S}}. \tag{19}$$

where $p_0 -$ Is the porosity before sintering (at t=0).

In the work of V.A. Ivensen [26], a kinetic equation for compaction during sintering was obtained

$$\upsilon = \upsilon_0 (qmt + 1)^{-1/m}, \tag{20}$$

where $\upsilon -$ is the pore volume at time t, $\upsilon_0 -$ is the initial pore volume; q - is the rate of decrease of the relative pore volume at time zero; m - is some constant.

Equation (20) can be written in the form.

$$\frac{\alpha}{1-\alpha} = (1 + qmt)^{1/m} - 1, \tag{21}$$

where $\alpha -$ is the compaction parameter

$$\alpha = \frac{V_0 - V}{V - V_\infty}, \tag{22}$$

V - is the volume of the sintered body; indices 0 and ∞ Refer to the initial state and infinite time.

Equation (21) under the condition $qmt >> 1$ practically coincides with the equation of M.Tikkanen [27]

$$\frac{\alpha}{1-\alpha} = (Kt)^n, \tag{23}$$

However, it remains correct for small t when equation (23) is not applicable, since $\frac{d\alpha}{dt} \to \infty$. at $t \to 0$.

The hyperbolic equation (19) is similar to the Ivensen equation (20), but has a completely different physical meaning: its kinetic constants are determined by changes not only in the structure, but also by geometric factors of the compaction kinetics, including the coefficients of grain boundary and surface diffusion.

Figure 3 shows the decrease in porosity, with rapid compaction occurring at the beginning of the sintering process and slowing down at longer times. The graph is fully consistent with Ivensen's phenomenology and highlights the difference with the proposed model.

To derive the kinetic equation for compaction during sintering using external pressure p, instead of the rheological equation (17), we will use a differential equation that determines the change in porosity during viscous flow of porous bodies under the action of externally applied forces of uniform all-around compression, without taking into account the change in free energy associated with capillary phenomena [20]:

$$\frac{dp}{dt} = \frac{-3\rho\, p}{4\eta} \tag{24}$$

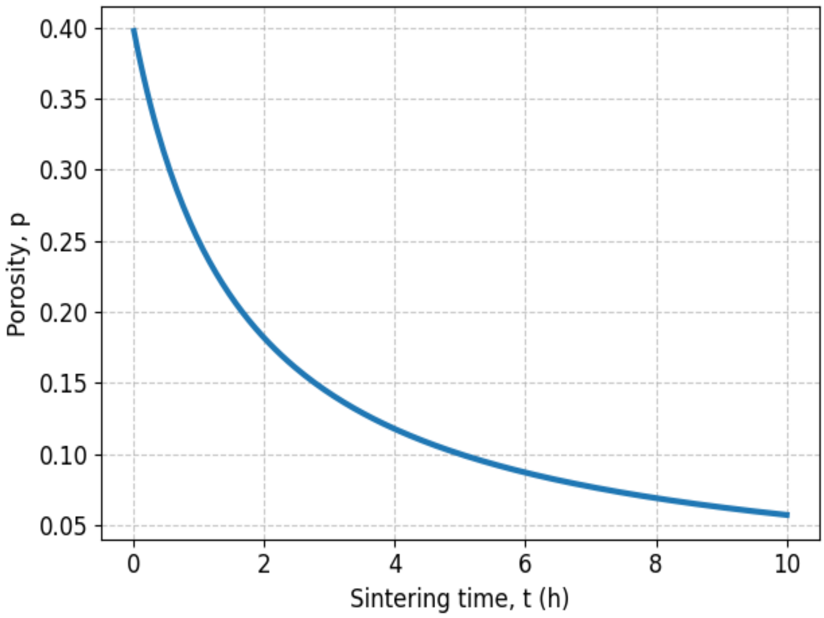

Fig. 3. Kinetics of compaction during sintering

Substituting (16) into (24), taking into account (7), we obtain

$$\frac{dp}{p} = \frac{-150 D_b \cdot \delta^4}{Kt} \frac{dt}{\left(L_0^4 + \frac{30\sigma D_S \delta^4}{kT} \cdot t\right)^{3/4}}. \tag{25}$$

Integrating (25), we obtain

$$p = p_0 \cdot \exp\left\{\frac{-20 D_b}{\sigma D_S}\left[\left(L_0^4 + \frac{30\sigma D_S \delta^4 \cdot t}{kT}\right)\right]^{1/4} - L_0^{1/4}\right\}. \tag{26}$$

If in equation (21), along with the external applied force, we take into account the effective Laplace pressure p_l, then equation (21) takes the form

$$\frac{dp}{pdt} = -\frac{3}{4}\frac{\rho - \rho_l}{\eta}. \tag{27}$$

We use the simplest dependence of p_l on porosity

$$\rho_l = \frac{3\sigma}{r_0}(1-p)^2, \tag{28}$$

where r_0 - is the average radius of particles.

Substituting (16) and (28) into (27), taking into account (7), we obtain

$$\frac{dp}{p\left[\rho+\frac{3\sigma}{r_0}(1-p)^2\right]}=\frac{-1500D_b\,\delta^4\cdot dt}{kt\left(L_0^4+\frac{30\sigma D_S\,\delta^4}{kT}\cdot t\right)^{3/4}}. \tag{29}$$

Let us denote $\lambda=\frac{pr_0}{3\sigma}$ and integrate (29)

$$\int_{\theta_0}^{\theta}\frac{dp}{p\left[\lambda+(1-p)^2\right]}=\frac{-50r_0}{\sigma}\int_{t_0}^{t}\frac{D_b\,\delta^4\cdot dt}{kT\left(L_0^4+\frac{30\sigma D_S\,\delta^4}{kT}\cdot t\right)^{3/4}}. \tag{30}$$

As a result of integration, we obtain an implicit solution to the differential equation (29):

$$\varphi(\rho)=\frac{-20r_0D_b}{3\sigma^2 D_s}\left[\left(L_0^4+\frac{30\sigma D_S\,\delta^4}{kT}\cdot t\right)^{1/4}-L_0^{1/4}\right]. \tag{31}$$

Where $\varphi(\rho)=\frac{1}{\lambda+1}\left[\ln\frac{p}{p_0}-\frac{1}{2}\ln\frac{p^2-2p+(\lambda+1)}{p_0^2-2p_0+(\lambda+1)}+\frac{1}{2}\text{arctg}\frac{p-1}{\sqrt{\lambda}}-\frac{1}{2}\text{arctg}\frac{p_0-1}{\sqrt{\lambda}}\right]$. (32)

Let $\{t_i\}$ $i=0,1,2,....$- be a given sequence of times. For $t=t_1$ we solve the nonlinear equation (31) for p with the initial condition $p=p_0$; $p_0=p\big|_{t=t_0}$. For any $t=t_{i+1}$ we solve equation (31) with the initial condition. $p_0=p\big|_{t=t_i}$. We find the solution to equation (31) for a given initial condition using the MATCAD system.

CONCLUSION

A kinetic equation of compaction during sintering of mesoscale powders of a mixture of a hard alloy based on tungsten carbide is obtained. In this case, the influence of external pressure in the differential equation is used instead of a realistic equation. By integrating, an implicit solution of the differential equation is obtained, which, for a given initial condition, can be found using the MATCAD program.

ACKNOWLEDGEMENT

This work was supported by the Azerbaijan Sciense Fondation Grant № AEF – MGC – 2024 - 2(50) – 16/01/1 – M – 01.

REFERENCES

[1] Mammadov Arif, Mammadov Vugar. *Comparative Analysis of Diffusion Metallization Coatings Applied on Steel Parts. Metallurgical and Materials Engineering. https://doi.org/10.56801/MME1020.31.10.2023.https://metallmatereng.com/index.php/home/article/view/1020/523.P.43-54.*

[2] Raqulya A.V., and Skorokhod V.V. *Consolidated nanostructured materials [in Russian],* Nauk. Dumka, Kiev, 2007). – 373p.

[3] Nikolenko S.V., Dvornik M.I., Pugachevsky M.A. et al. *Use of Al_2O_3 nanopowder as a grain growth inhibitor in BK8 alloy* // Materials Science Issues, 2008, 2 (54). p.100-105.

[4] 4. Antsiferov V.I., Antsiferova I.V. *Features of sintering processes using nanosized carbide powders (scientific review)* // Bulletin of PNIPU. Mechanical engineering, materials science, 2015, v.17, no.2, pp.66-77.

[5] *Production and application of Advanced W-based Nanopowders* /O.Tolochko [et al.] //9th Conference on Solid State Chemistry: conf. Mater. Prague, Czech Republic, Sept. 10-15, 2019, p.58-62.

[6] *Synthesis and Characterization of Nanoscale Tungsten Carbide Powder* /O.G.Klimova [et. al] //XIXth International Baltic Conference Materials Enfineering 8t Balttrib – 2010: conf.mater., Riga, Latvia, Oct.28-29, 2010, c.41.

[7] Langbauer, R., Nunner, G., Zmek, T., Klarner, J., Prieler, R., Hochenauer, C. Investigation of the temperature distribution in seamless low-alloy steel pipes during the hot rolling process. *Journal of Advances in Industrial and Manufacturing Engineering*, 2021, 2, 100038. https://doi.org/10.1016/j.aime.2021.100038.

[8] Vasileva K., Tolochko O., Kaidash E., Kim D., Lee D.-W. *Production and Application of Advanced W-based Nanopowders* //EDA Publishings/ENS 2007 – p.53-56.

[9] Fang Z.Z., Wang X., Ryu T., Hwang K.Sa., Sohn H.Y. *Synthesis, sintering, and mechanical properties of nanocrystaline cemented tungsten carbide – A review.* //Int. Journal of Refractory Metals 8τ Hard Materials 27 (2009) 288-299.

[10] Yamamoto T., Ikuhara Y., Sacuma T. *High resolution transmission electron microscopy study in VC doped WC-Co compounds* //Science and technology of advanced materials. – 2000. – vol.1. – p.97-104.

[11] 11. Ivensen V.A. *Phenomenology of sintering and some theoretical issues.* – M.: Metallurgy, 1985. – 247 p.

[12] Jhonson D.L. *"Ultrarapid sintering of ceramics" in D.P.Uskokovic, Hayne Palmour III, and R.M. Spriggs (eds.), Science of Sintering.* New Directions for Materials Processing and Microstructural Control, Plenum Press, New York, London (1989), pp.497-506.

[13] Karimov, R.I. Features of removal of phosphorus and sulfur from remelting stock during electric arc melting of steel. *International Journal of Control and Automation,* 2020, 13 (1), p.137–159. Available at: http://sersc.org/journals/index.php/IJCA/ article/view/5090

[14] Skorokhod V.V. "*The main trends in study and quantitative description of the sintering processes*", in: D.P.Uskokovic, Hayne Palmour III, and R.M.Spriggs (eds.) Science of Sintering. New Directions for Materials Processing and Microstructural Control, Plenum Press, New York, London (1989), pp.39-54.

[15] Rozhkova, O. V. Investigation of the nature of defects on the outer surface of heat-treated seamless pipes. *Journal of Foundry Production and Metallurgy*, 2020, 4, 90–93. https://doi.org/10.21122/1683-6065-2020-4-90-93

[16] Skorokhod V.V., Solomin Yu.M., and Uvarova L.V. *Chemical, Diffusional, and Rheological Processes in Powder Materials Technology* [in Russian]; Nauk. Dumka, Kiew (1990). – 247p.

[17] Skorokhod V.V. and Ragulya A.V. *"Futures of nanocrystalline structure formation on sintering of ultrafine powders",* in: Gan Mog.Chow and N.I.Noskova (eds.), Nanostructured Materials. Science and Technology, NATO ASI. Ser.3.High Technology, Kluwer Academic Publishers, Dordrecht, Boston, London, vol.50, 378-404 (1998).

[18] German R.M. *A Sintering Parameter for Submicron powders* //Sci.Sintering. – 1978. – 10, N1. – P.11-25.

[19] Geguzin Ya.E. *Physics of sintering. – 2nd ed.* – M.: Nauka, 1984. – 312 p.

[20] Gottstein G. *Physicochemical foundations of materials science* / Translated from English. – M.: BINDM; laboratory of knowledge, 2011. – 402 p.

[21] Mehrer H. *Diffusion in solids / Springer Science & Business Media*, 2007 – 654 p.

[22] Stromberg A.G., Semchenko V.P. Physical Chemistry.–M.:Higher School, 2006. – 527s.

[23] Mean D.M., Koe R.C. *Mechanism and Kinetics of Hole Formation in Added Tungsten* //Metall.Trans. – 1971. – 2. – P.2115-2122.Virial.

[24] Virial. Materials [Electronic resource]: Virial company *website*. – Access mode: http: //www.virial.ru/materials/92.

[25] Skorokhod V.V. *Rheological foundations of sintering theory.* – Kyiv: Naukova Dumka, 1976. – 151 p.
[26] Ivensen V.A. *Kinetics of compaction of metal powders during sintering*. – M.: Metallurgy, 1971. – 272 p.
[27] Tikkanen M.H., Makipiritti S.A. //*International J. of Powder Metallurgy*, 2005, №1, issue 15, 382p.

Received: 05.04.2025
Accepted: 12.10.2025

MACHINE SCIENCE

ISSN: 2227-6912
E-ISSN: 2790-0479

2025, № 2 Pages 38-49

SCIENTIFIC AND METHODOLOGICAL SUPPORT FOR DESIGNING GRINDING OPERATIONS USING AN ACOUSTIC INDICATOR

Aleksandr ZHUKOV[1,a], Dmitriy ARDASHEV[1,b], Viktor KULYGIN[1,c], Viktor BATUEV[1,d], Nizami YUSUBOV[2,e], Heyran ABBASOVA[2,f*]

[1]South Ural State University, Chelyabinsk, Russia
[2]Azerbaijan Technical University, Baku, Azerbaijan

*E-mail: [a]zhukovas@susu.ru, [b]ardashevdv@susu.ru, [c]kulyginvl@susu.ru, [d]batuevvv@susu.ru, [e]nizami.yusubov@aztu.edu.az, [*f]abbasova.heyran@aztu.edu.az*

https://doi.org/10.61413/CXZB2097

Abstract: This article describes a methodology for designing grinding operations that employs an acoustic indicator and outlines the main stages of its development. The methodology was developed to enhance the productivity of grinding operations. The efficiency criteria are defined as the minimization of: operational time, setup and teardown time, the residual service life of the grinding wheel, and the consumption of the wheel's useful volume and mass. The methodology is implemented at the grinding process design stage and is based on a computer simulation model of the sound pressure parameters generated by the grinding process, developed in specialized software. This model enables the calculation of sound pressure amplitude values at an informative frequency for specified technological conditions. A crucial element of the methodology is the application of an integrated model. This comprehensive modeling approach allows for the formation of a data cell containing values for the grinding sound pressure amplitude and the topographical quality parameters of the machined surface for specific technological conditions. The development of the integrated model involves coupling data from three sources: the described model of the grinding acoustic signal parameters, and existing models for determining the values of surface roughness (Ra) and deviation from cylindricity (Δ) of the ground surface. Based on the integrated model, prediction maps for the defect-free operation zone of the grinding wheel have been developed within the coordinates of processing regime and time. These maps facilitate the determination of rational processing regimes and grinding wheel characteristics. The main industrial scenarios where the application of this methodology yields the most significant effect are also considered. The intended area of application for the methodology is high-variety manufacturing, which holds a leading position in the modern machine-building industry.

Keywords: *Grinding, grinding process design, acoustic monitoring of grinding, acoustic criterion for grinding wheel performance.*

INTRODUCTION

In modern mechanical engineering, grinding operations hold a unique position as the final machining stage, defining the key performance characteristics of components. The technological significance of grinding is rooted in its ability to provide high dimensional accuracy and surface quality across a multitude of industries, such as mechanical engineering, automotive, aviation, medical, military, and aerospace [1].

The efficiency of a grinding operation is determined during its design stage, which involves specifying optimal characteristics for the grinding wheel (GW) and machining parameters to achieve the required product quality with maximum productivity.

One of the significant challenges in grinding that must be considered during operation design is the inevitable wear of the GW during the process, which can negate the aforementioned advantages of grinding. An approach to solving this problem involves, in part, developing and implementing methods for monitoring the current performance of the GW.

Methods for assessing the technical condition of the GW are categorized as direct and indirect [2, 3].

Direct monitoring methods provide a wealth of information and can ensure high measurement accuracy; however, they involve substantial costs for expensive equipment and specialized instrumentation required for the direct measurement of wear parameters. These methods are primarily suited for controlled laboratory environments, as their application requires interrupting the manufacturing process, which limits their use in production settings.

An approach based on the use of indirect indicators of GW wear offers significant advantages (high informativeness [4], sensitivity [5, 6], and cost-effectiveness) and a key benefit over direct methods: the ability to be used for in-process monitoring.

When implementing monitoring systems (MS) for the grinding process, various evaluation criteria and instrumentation are employed, and different aspects of the process can be observed. For instance, the degree of GW wear is assessed based on optical criteria using a laser sensor [7] and a chromatic confocal sensor [8]; by the spindle motor current [2]; and using the acoustic emission (AE) signal [9, 3].

A promising direction for the development of monitoring systems is the integrated analysis of multiple technological criteria. The combined processing of data on vibrations, drive power, temperature in the grinding zone, and acoustic characteristics enables the development of a digital tool wear model with high predictive capability. The implementation of such systems is particularly relevant in automated manufacturing environments, where the ability to predict the remaining tool life becomes crucial for optimal replacement scheduling. In [10, 11], the indirect monitoring parameters used are grinding force (measured by a dynamometer), vibrations of the technological system (TS), and the AE signal; in [12], TS vibration parameters and the AE signal; and in [13], TS vibration parameters, grinding power, the AE signal, and grinding zone temperature.

This literature review demonstrates a significant reduction in equipment downtime, improved machining accuracy, and lower maintenance costs resulting from the use of monitoring systems (MS) [13-22], and highlights the high level of interest among researchers in their application to grinding operations [1].

An analysis of the monitoring criteria reviewed above reveals that most of them require costly additional hardware and software upgrades to the production equipment. In this context, the vibration and acoustic characteristics of machining processes are of particular interest, as their application does not involve significant costs.

Monitoring the acoustic signal offers several key advantages over other criteria. The acoustic signal contains information about the state of the equipment or tool, machining quality, and incipient defects, which enables a prompt assessment of the system's technical condition [23, 24]. Monitoring systems based on the registration and analysis of the acoustic signal do not require major equipment overhauls, which indicates the simplicity and cost-effectiveness of their implementation.

Moreover, it is well-known that in a production setting, the subjective experience of a grinding operator allows them to determine when to dress the GW and adjust machining parameters based on audible cues from the process. This fact provides a strong rationale for using acoustic monitoring to control the grinding process. This is supported by scientific research in which vibro-acoustic parameters are used as the criterion for assessing the system's technical condition [25-28].

The characteristics of the acoustic signal accompanying the grinding process can also be used for the design of grinding operations. A significant advantage of this approach is the ability to assess the *actual* current state of the system. Unlike an approach based on mathematical models, acoustic monitoring provides precise values for the criterion parameters, which are determined not by computational methods containing inherent errors, but through direct recording via specialized instrumentation. By correlating the criterion values of the recorded process parameter with the required output parameters of the grinding operation, it becomes possible to control the process more effectively and achieve superior results.

An approach that combines the monitoring and simulation of the process's vibro-acoustic parameters, while considering machining quality requirements, is highly promising for designing grinding operations. Simulation during the process planning (PP) stage allows for the selection of rational GW characteristics and machining parameters, while process monitoring enables the assessment of the GW's current technical condition based on an indirect acoustic indicator linked to the quality requirements.

Collectively, this will make it possible to predict important tool performance indicators, select rational technological conditions (TC) for its application, and track actual parameters in real time to control machining quality, reduce resource consumption, increase productivity, and improve overall production efficiency, etc.

Thus, the aim of this work is to develop a methodology for designing grinding operations using an acoustic indicator. The paper outlines the main stages of developing this methodology:

- selection and justification of the initial data for design;
- modeling of grinding parameters;
- establishing a correlation between grinding quality parameters and the process's acoustic criterion;
- development of application guidelines in the form of special documents (KPOBR)*;
- techniques for applying the recommendations and the main expected benefits.

Table 1 lists the notations used in this paper.

Table 1. List of used symbols

Notation	Definition
Ap, f_{inf}	sound pressure amplitude, informative frequency;
Ap^{cur}, Ap^{crit}	current and critical value of the sound pressure amplitude;
$Ap^{crit}_{Ra}, Ap^{crit}_{\Delta}$	critical values of sound pressure amplitude for the specified roughness and out-of-roundness criteria;
Ap^{crit}_{min}	the lowest sound pressure amplitude value, selected by comparing Ap^{crit}_{Ra} and Ap^{crit}_{Δ}, GW tool life criterion;
D×T×H	outer diameter, width, and bore diameter of the GW, respectively;
H_CS×W_CS	dimensions of the contact area between the GW and the workpiece;
L_g	length of the abrasive grain wear flat;
V_{Srad}	plunge (radial) feed rate, mm/min;
V_{Srad_rat}	rational plunge feed rate for the specified TC;
n_{GW}, n_{wp}	rotational speed of the GW and workpiece;

P_Y, P_Z	radial and tangential components of the grinding force;
j	stiffness of the TS;
E	Young's modulus of the GW;
ν	Poisson's ratio of the GW;
ρ	density of the GW;
k	set of grinding quality parameters;
m	set of grinding parameters (radial feed rates);
n	set of time instances τ;
i	set of GW characteristics;
IT	dimensional accuracy of the ground surface;
Ra	surface roughness parameter of the ground surface;
Δ	out-of-roundness of the ground surface;
T	grinding time;
T_{op}, T_{main}, T_{aux}	operating, main, and auxiliary machining time for one part;
T_{s-t}	setup and teardown time for a batch of parts;
T_{tl}	GW tool life;
R, R^{rem}	GW service life and remaining GW service life;
μ	coefficient of friction between the abrasive grain and the workpiece material;
σ_i	stress intensity in the volume of deformed metal, characterizing the resistance of the workpiece material to plastic flow;
z	acoustic impedance.

Methodology for Designing Grinding Operations Using an Acoustic Indicator. The practical significance of using an indirect acoustic indicator for grinding lies in the ability to determine rational operating conditions during the process planning (PP) stage (Table 2). In this context, acoustic monitoring acts as a process control tool, making it possible to avoid machining with a tool that cannot ensure the required quality parameters (Ra and Δ). This is achieved by monitoring the current sound pressure amplitude and comparing it to a critical value ($Ap^{cur} \leq Ap^{crit}$).

Table 2. Indicators of grinding efficiency improvement through the application of a grinding process design methodology

Paths to Increased Efficiency	Methods for Increasing Efficiency
$\Sigma T_{op} = \Sigma T_{s-t} + \Sigma T_{aux} \rightarrow \min$	Determining the rational grinding parameters
$\Sigma T_{op} + T_{s-t} \rightarrow \min$	Determining the rational GW characteristics
$R^{rem} \rightarrow \min$	Determining the rational sequence for feeding workpieces to the machine

Figure 1 presents a diagram of the methodology for designing grinding operations, which includes five main stages: selection and application of initial data; modeling of grinding process parameters; establishing a correlation between machining quality parameters and the process's acoustic characteristics; development of guideline documentation for process parameters and tooling; and practical implementation of the methodology.

The fifth stage of the methodology is implemented during operation design and production (Fig. 1, stage 5). Monitoring the acoustic signal that accompanies the grinding process enables the indirect assessment of current quality indicators at the production stage without interrupting the manufacturing process. The technical condition of the GW is monitored by continuously comparing the current value of the sound pressure amplitude with its predetermined critical value (Fig. 1, stage 5).

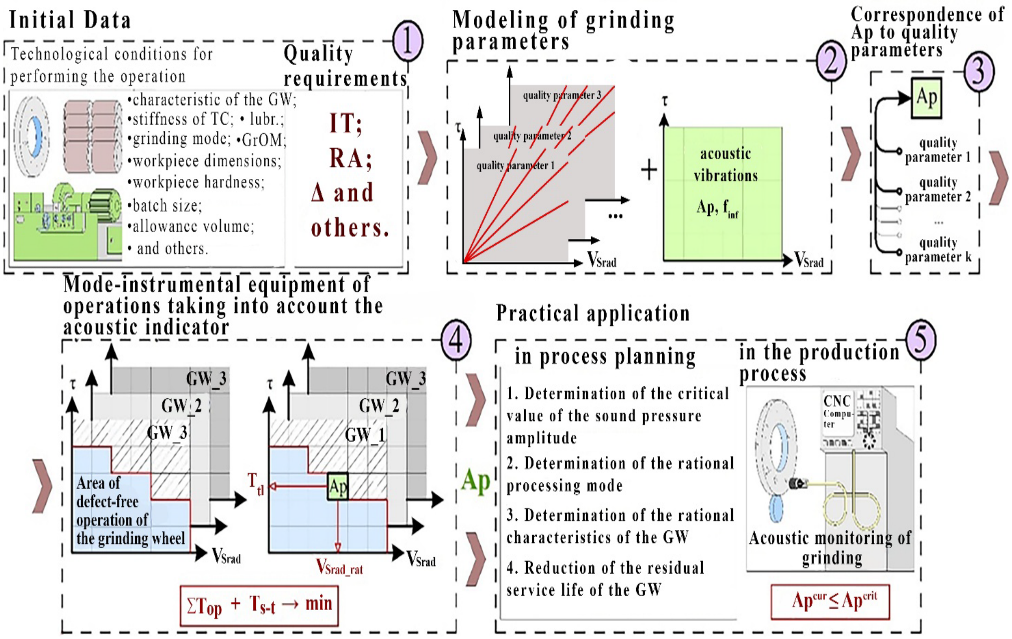

Fig.1. General framework of the grinding process design methodology using an acoustic process indicator

The design of grinding operations involves specifying the tooling and process parameters based on the process's acoustic indicator. Through simulation in the "grinding parameter–time" coordinate plane, a defect-free operating region for the GW is predicted, within which the machining quality requirements will be met. The boundaries of this region are defined based on the specified quality requirements for specific TC (for a GW with particular characteristics and a batch of workpieces with particular properties) and are compiled into a set of predictive charts for the defect-free operating region (KPOBR) of the GW. This enables the use of an optimization approach to determine the most productive machining parameters and GW characteristics, guaranteeing compliance with product quality requirements (Fig. 1, stage 4).

The development of the KPOBR for the GW requires establishing a correlation between the acoustic signal parameters and the machining quality parameters—this is the most crucial stage of the methodology (Fig. 1, stage 3). The acoustic indicator of the grinding process, which serves as the criterion for GW performance, cannot be used without establishing such a correlation.

Correlating machining quality parameters with acoustic parameters through mathematical relationships is possible only if the models share common process parameters as inputs. These parameters are selected based on their suitability for constructing the defect-free operating region of the GW. Therefore, it is appropriate to select the machining parameters and time as the variables linking the quality and acoustic characteristics, as they account for the current technical state of the tool. The result of this correlation is a comprehensive model that establishes a relationship be-tween quality parameter values and acoustic parameters for similar TC.

The current performance of the GW can be characterized by the current values of the grinding process parameters. These values can be obtained through modeling and/or monitoring of the machining process. A sufficiently accurate mathematical model of the acoustic signal generated dur-ing grinding makes it possible to predict it in accordance with the specified TC (Fig. 1, stage 1). The established correlation between the acoustic indicator and machining quality parameters, combined with the use of acoustic monitoring, enables a reliable assessment of the GW's current technical condition.

Thus, the need to create a mathematical model of the acoustic signal that accompanies the process is justified for the development of the proposed methodology (Fig. 1, stage 2).

Simulation Model of Sound Pressure Parameters Generated by the Grinding Process. The model of sound pressure parameters generated by the grinding process was developed using the specialized software COMSOL Multiphysics®, which is designed for solving multiphysics problems. The model describes the vibrations of the GW caused by the grinding force, taking into account initial and boundary conditions such as the mounting of the GW on the machine head-stock, rotation at 1590 rpm, damping, and the dimensions of the contact area between the GW and the workpiece. Subsequently, the parameters of the acoustic field created by the mechanical vibrations of the GW are calculated, considering the properties of the surrounding medium (acoustic impedance). To determine the GW vibration parameters, it is necessary to specify its integral elastic constants, which are related to the tool's characteristics (abrasive material, grit size, grade, structure, and bond type). When specifying the grinding force, the dynamic TC of the operation are taken into account, including machining parameters, GW wear, and the stiffness of the technological system (TS). The two problems are coupled through a multiphysics interface.

The frequency and amplitude of the sound pressure are determined by the following TC: cutting parameters (VS_{rad}, n_{GW}, n_{wp}); GW characteristics (D×W×H, ν, E, ρ); GW technical condition (lg, PY, PZ); workpiece material (WM) properties (μ, σ_i); and environmental properties (z).

The frequency used for acoustic monitoring during the grinding process is referred to as the informative frequency (f_{inf}). The frequency distribution in the spectrum of acoustic vibrations is uniquely determined by the geometric dimensions, integral elastic properties, and boundary conditions of the GW. The value of f_{inf} corresponds to the frequency of the lowest mode of the GW's bending vibrations. This bending mode of vibration provides a convenient basis for acoustic diagnostics.

Figure 2 shows a structural diagram of the sound pressure simulation model, outlining the implemented processes, intermediate results, and the connections between them. The model's structure is organized into three levels: the input data level, the data adaptation level for calculations, and the results level.

The input data required for the simulation are grouped according to the elements of the system being considered: the GW, the equipment, the workpiece, and the surrounding environment. These properties are used to define the technological conditions (TC) for which the simulation is performed. Establishing the input data is a straightforward task handled by a process engineer during the process planning (PP) stage; however, not all input data can be used to calculate the desired parameters directly. For instance, to account for the GW's properties when calculating its vibration parameters, a quantitative description of its characteristics is required. The data adaptation level is intended to prepare data for direct use in COMSOL Multiphysics®. This involves defining and/or describing:

- the elastic properties of the vibrating body—the GW;
- the boundary conditions under which the system's vibrations are calculated;
- the region over which the excitation load is distributed—the dimensions of the contact area;
- the characteristics of the excitation force (the grinding force)—its magnitude and direction.

At the results level, the informative frequency and sound pressure amplitude are calculated based on the adapted input data. This requires the correct configuration of the software's interfaces to reflect the interactions between the elements of each level and the data transformation paths.

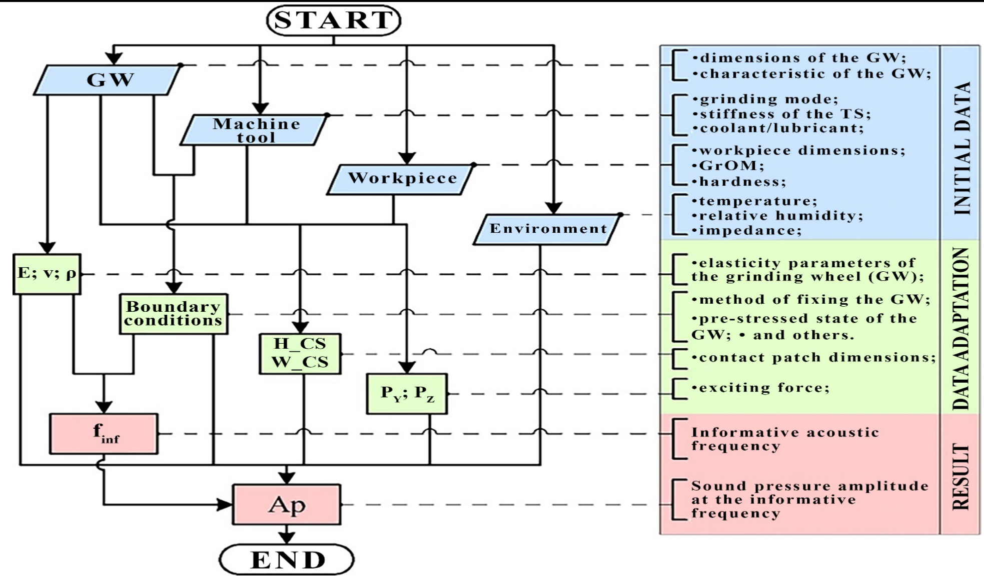

Fig.2. The structure of the simulation model for sound pressure parameters

Thus, the model enables the calculation of sound pressure amplitude values generated during grinding at the specified informative frequency under given TC. Variable process factors, such as the technical condition of the tool, are accounted for through the excitation force—the grinding force. The established relationship between the TC and the sound parameters of the grinding process becomes a useful tool only after a strict correlation is established between the process's acoustic parameters and the machining quality parameters—namely, surface roughness (Ra) and out-of-roundness (Δ) of the ground workpiece surface.

To establish this correlation, mathematical models describing the topographical parameters of the machined surface are coupled with those describing the acoustic parameters of the process for the specified TC. The model resulting from this coupling will be referred to as the **comprehensive model**.

COMPREHENSIVE MODEL CORRELATING TOPOGRAPHICAL QUALITY PARAMETERS OF THE GROUND WORKPIECE SURFACE WITH THE PROCESS'S ACOUSTIC PARAMETERS

The justification for developing a comprehensive model to determine actual current quality parameters lies in the ability to use an indirect acoustic indicator for monitoring, instead of relying on direct measurements. The primary requirement for developing this comprehensive model is the fundamental ability to establish a correlation between quality parameters and the process's acoustic characteristics. Meeting this requirement necessitates that the arguments used in the quality parameter models coincide with the arguments that determine the sound pressure parameter values obtained from the simulation.

To enable dynamic monitoring of machining quality parameters, the function must directly depend on time or contain an argument linked to the grinding duration. In the computer simulation of sound pressure parameters, the degree of tool wear, which is dependent on machining time, was taken into account by adjusting the magnitude of the excitation force (the grinding force).

Therefore, the mathematical models for the quality parameters must include:

•arguments describing the technological conditions (TC) of the operation, to establish a correspondence between these models and the results of the sound pressure simulation;

• a time argument, to enable the discrete calculation of the parameter's change at any given moment.

These requirements are fully met by the geometric model of ground surface formation and stock removal by L.V. Shipulin [29] and the model of the force interaction between the GW and the workpiece during external cylindrical plunge grinding by A.Kh. Nurkenov [30].

Figure 3 presents the structure of the comprehensive model as a diagram correlating the simulation results for sound pressure amplitude with the topographical parameters of grinding quality. The parameters (Ap, Ra, Δ), calculated for identical TC, are combined into a coupled data cell. A set of these cells is distributed in the machining parameter–time coordinate plane. An additional third axis characterizes the GW properties for which the simulation was performed. As a result, a data array is formed for multiple TC, correlating the machining quality parameters with the acoustic characteristics of the grinding process.

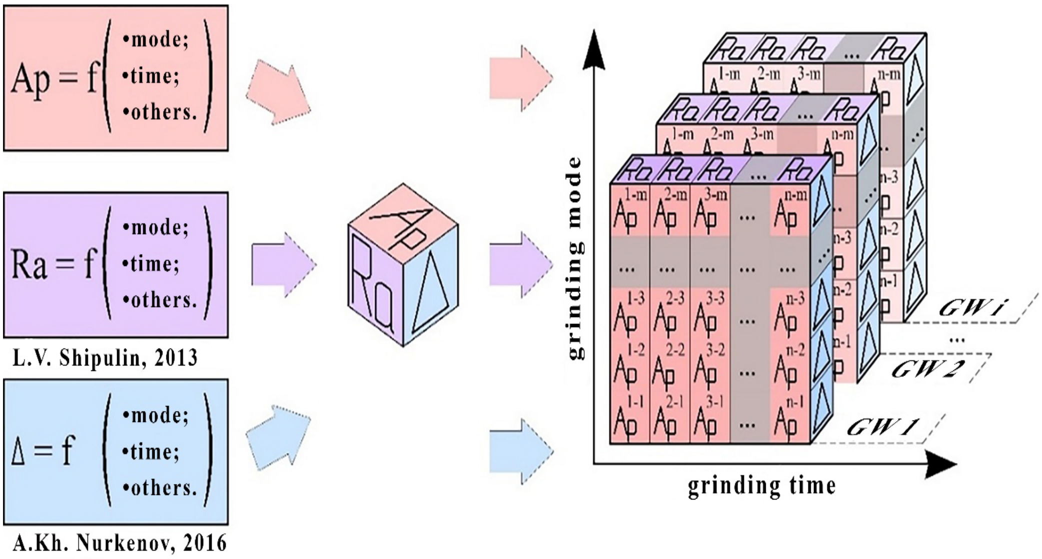

Fig.3. The structure of a comprehensive compliance model of processed surface topographical parameters with an acoustic process indicator

For practical application in a manufacturing environment, the data array is organized into sets of KPOBR charts for the GW. Using these charts, a grinding operator or process engineer can determine the sound pressure amplitude value that corresponds to the specified quality requirements for specific GWs and workpiece materials, across a range of applicable machining parameters.

RESULTS AND DISCUSSION

The simulation results for the sound pressure parameters were verified (Fig. 4). A high degree of correspondence was found between the frequency spectra of the experimentally recorded acoustic signal and the signal calculated by the model. The discrepancy in the frequency spectra does not exceed 3.5%, while the difference between the informative frequency values is 0.5%.

The experimental graph contains two frequency ranges with peak Ap values that are absent from the calculated graph. It has been established that the frequency component in the 700-800 Hz range is generated by the rotation of the grinding headstock with the GW mounted on it. In the 2200-2300 Hz range, a spike occurs, caused by the hydraulic pump. These components are present during the machine's idle operation and should not be considered when analyzing the frequency spectrum of the grinding acoustic signal.

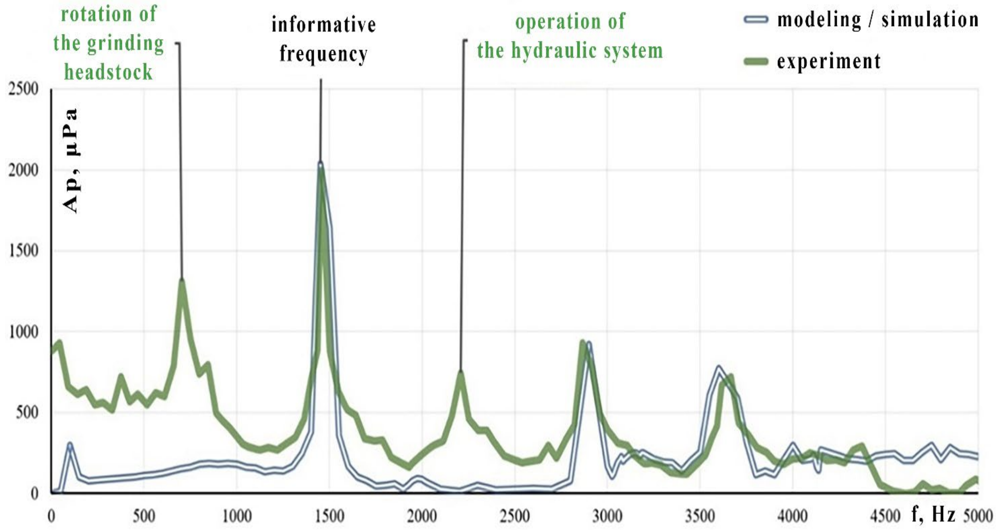

Fig.4. Comparison of the frequency spectra of acoustic grinding signals obtained from simulation and experiment

A method is proposed for determining the rational machining parameters for batches of workpieces, based on the application of the grinding process's acoustic indicator.

Within the parameter-time domain of the defect-free operating region, there are multiple potentially applicable machining parameters. Each parameter corresponds to a specific machining time during which quality requirements are met—the tool life period. Based on the batch characteristics (batch size, average stock removal), the methodology allows for the determination of the most rational machining parameter that will minimize the total operating time.

A method is also proposed for determining the rational GW characteristics for machining multiple batches of workpieces.

In high-mix manufacturing environments, a simulation of grinding sound pressure parameters is performed during the PP stage for several GWs (those available in stock or planned for purchase) to determine the rational tool characteristics. The rationality criterion is the minimum standard time, encompassing the total operating time (Σ Top) and setup/teardown time (Ts-t) required to machine all planned batches, while meeting quality requirements and minimizing the number of GW changes on the machine.

A method is also proposed for determining the rational sequence for feeding workpieces to the machine.

In high-mix manufacturing environments, during the PP stage, the time intervals required for the sound pressure amplitude to reach its critical values for each batch are predicted; these intervals represent the theoretically possible tool life periods.

Based on the stock allowance for each batch, the number of parts that can be machined within a single tool life period is calculated. This makes it possible to determine the actual GW tool life periods for each batch and the corresponding values of the remaining service life (R_{rem}). Through an exhaustive search, the rational sequence for machining the workpiece batches is determined based on the criterion of minimizing the total remaining GW service life.

CONCLUSIONS

1.The developed simulation model of the acoustic parameters of the grinding process makes it possible to determine sound pressure amplitude values at the informative frequency for multiple combinations of technological conditions (TC). These values are suitable for use in acoustic monitoring for the indirect assessment of the GW's current technical condition.

2.The comprehensive model enables the use of the simulation model of grinding's acoustic parameters to indirectly assess the current quality of the machined surface (roughness and out-of-roundness) under the specified TC.

3.The application of the proposed methodology improves the efficiency of grinding operations by optimizing several aspects of the production process: grinding parameters, tool characteristics, and the rational sequence for feeding workpiece batches to the machine. The methodology is expected to reduce the total operating, auxiliary (time for GW dressing), and setup/teardown times; decrease the consumption of the GW's effective mass and volume; and lead to a more complete utilization of the GW's service life.

ACKNOWLEDGEMENTS

This work was supported by the Russian Science Foundation (Grant No. 25-29-20029, https://rscf.ru/project/25-29-20029/).

REFERENCES

[1]. Kacalak W., Lipinski D., Szafraniec F., Wieczorowski M., Twardowski P. *Metrological Aspects of Assessing Surface Topography and Machining Accuracy in Diagnostics of Grinding Processes.* Materials, 2023, 16(2195), pp.1-26. https://doi.org/10.3390/ma16062195

[2]. Si S., Mu D., Tang H.A. *Hybrid CBiGRUPE Model for Accurate Grinding Wheel Wear Prediction.* Sensors, 2025, 25 (2935), 1-21. https://doi.org/10.3390/s25092935

[3]. Kon T., Mano H., Iwai H., Ando Y., Korenaga A., Ohana T., Ashida K., Wakazono Y. *Effect of Acoustic Emission Sensor Location on the Detection of Grinding Wheel Deterioration in Cylindrical Grinding.* Lubricants, 2024, 12(100), pp. 1-12. https://doi.org/10.3390/lubricants12030100

[4]. Bezzubceva M.M., Volkov V.S. *Analytical review of the package of application programs for modeling of energy processes of consumer energy systems agro-industrial complex*. International journal of applied and fundamental research, 2015, vol. 6, pp. 191-195

[5]. Lu Z.-J., Xiang Q., Xu L. *An application case study on multi-sensor data fusion system for intelligent process monitoring*. Procedia CIRP, 2014, 721-725. https://doi.org/10.1016/j.procir.2014.01.122

[6].Liu C.-S., Ou Y.-J. *Grinding Wheel Loading Evaluation by Using Acoustic Emission Signals and Digital Image Processing*, Sensors, 2020, vol. 20, no. 15, p. 4092, ISSN: 1424-8220. https://doi.org/10.3390/s20154092

[7]. Wang Ch-Y., Huang Ch-Y., Chiang Y-H. Novel, *High-precision, on-machine approach for measuring cup grinding wheel wear using a moveable laser displacement sensor*. Journal of Manufacturing and Material Processing, 2025, 9(122), 1-15. https://doi.org/10.3390/jmmp9040122

[8]. Lishchenko N. O'Donnell G.E., Culleton M. *Contactless method for measurement of sur-face roughness based on a chromatic confocal sensor. machines*, 2023, 11(836), 1-26. https://doi.org/10.3390/machines11080836

[9]. Xu K., Feng D. A *Method for identifying the wear state of grinding wheels based on VMD denoising and AO-CNN-LSTM*. Applied sciences, 2024, 14(3554), 1-20, https://doi.org/doi.org/10.3390/app14093554

[10]. Duan J., Cao G., Ma G., Yu Z., Shao C. *Research on on-line monitoring of grinding wheel wear based on multi-sensor fusion*. Sensors, 2024, 24(5888), 1-15. https://doi.org/10.3390/s24185888

[11]. Yusubov N.D., Abbasova H.M., Dadashov R.Y. the influence of cutting conditions and tool wear on machining efficiency in CNC machine tools. Machine science, 2025, no.1, pp. 4-19. https://doi.org/10.61413/IYJP4291

[12]. Zhuo R., Deng Z., Ge J., Liu W., Lu L., Yan C. *Research on cloud-edge-device collaborative intelligent monitoring system of grinding wheel wear state for high-speed cylindrical grinding of bearing rings*. Actuators, 2024, 13(327), pp. 1-25. https://doi.org/10.3390/act13090327

[13]. Rodriguez-Fortun J-M., Alvarez J., Monzon L. et al. *Digitalization of an industrial process for bearing production*. Sensors, 2024, 24 (7783), 1-17. https://doi.org/10.3390/s24237783

[14]. Sevastyanov A.A., Selivanov A.S. *Monitoring of tool wear during turning on CNC lathes*. Symbol of the science, 2016, No. 11-3(23), pp.144-148.

[15]. Yusubov N.D. *Fundamentals of matrix theory of accuracy of multi-tool turning, (principles and structure of the theory) design and management of multi-tool machining processes*. Omni-Scriptum GmbH and Co. KG / LAP LAMBERT Academic Publishing, 2013, 216 p, Saarbrucken, Germany.

[16]. Yusubov N.D. *Matrix models of working accuracy at single-cutter turning*. Tekhnologiya Mashinostroeniya, 2009, no. 1, pp. 41-45.

[17]. Yusubov N.D., Khankishiyev I.A., Abbasova H.M., Mammadov E.D., Huseynov R.A. *Matrix Models of Machining Errors in Multi-Tool Multi-Carriage Adjustments*, International Journal on Technical and Physical Problems of Engineering (IJTPE), September 2023, issue 56, vol. 15, no. 3, pp. 309-315.

[18]. Bogatenkov S.A., Sazonova N.S., Yusubov N.D., Abbasova H.M., Badalova B.B., Bazhenov R.I., *Decision making in the conditions of introduction of automated design systems of technological processes*, Socar Proceedings, 2022, special issue 1, pp. 006-010.

[19]. Yusubov N.D., Abbasova H.M., Dadashov R.Y. *Theoretical basis for the development of an algorithmic unified complex of mathematical models of cutting forces*. Machine science, 2023, no.1, pp. 55-60. https://doi.org/10.61413/pydj5288

[20]. Yusubov N., Abbasova H. *Models of cutting forces in the matrix theory of multitool machining accuracy*. Key Engineering Materials, 2024. Vol. 979, pp. 27-38. https://doi.org/10.4028/p-bw48sb

[21]. Zhmurin V.V., Khryachkova V.V. *Improving the quality of processing parts from stainless steels on medium-sized multi-purpose milling machines of the milling group*. Proceedings of Tula State University. Technical Sciences, 2021, no. 8, pp. 309-313.

[22]. Bogatenkov S.A., Sazonova N.S., Guzeev, V.I., Yusubov N.D., Abbasova G.M. Increasing the productivity of multitool machining on automated lathes by optimizing the tool positions. Russian Engineering Research, 2021. Vol. 41, pp.1075-1079 https://doi.org/10.3103/S1068798X21110058

[23]. Glagovskiy B.A., Moskovenko I.B. *Low-frequency acoustic testing methods in mechanical engineering*. Leningrad, Mashinostroyeniye, 1977, 208 p.

[24]. Oglezneva L.A., Kalinichenko A.N. *Acoustic Methods of Inspection and Diagnostics. Part 2: Textbook*. National Research Tomsk Polytechnic University, 2009, 292 p.

[25]. Kurchenko P.S. *Experimental studies of the spectral composition of vibrations and noise of*

coordinate and profile grinding machines. NOISE Theory and Practice, 2021, iss. 7, no. 5, pp. 78-91.

[26]. Kovarskaya YE. Z., Moskovenko I.B. *Use of natural oscillation technique in nondestructive evaluation of physical mechanical properties of materials and products*. In the world of non-destructive testing, 2012, no. 4 (58), pp. 5-8.

[27]. Ignat'yev S.A., Vasin M.P. *Bearings' rings multi parameter in-process grinding within the technological process monitoring system*. Bulletin of the Saratov State Technical University, 2008, no 1, iss. 2, pp. 67-74.

[28]. Gur'yanikhin V.F., Agafonov V.V., Pankov A.A. *Control of the plunge-cut external cylindrical grinding process using an acoustic signal*. STIN (Machines and tools), 2009, no. 2, pp. 35-40.

[29]. Shipulin L.V. *Improving method of design of operations flat grinding based on complex imitating modeling*. Modern problems of science and education, 2013, no. 2, pp C. 1-8.

[30]. Nurkenov A.KH., Gerenshteyn A.V., Mashrabov N.M. *Methodology for modeling plunge-cut cylindrical grinding considering the actual stiffness of the technological system***.** Proceedings of the LIV International Scientific and Technical Conference "Achievements of Science for the Agro-Industrial Production", 2015, pp. 92-98.

Received: 24.07.2025
Accepted: 04.11.2025

MACHINE SCIENCE

ISSN: 2227-6912
E-ISSN: 2790-0479

2025, № 2 Pages 50-60

A STUDY ON INTEGRATING DIGITAL TWIN PIPELINES USING USD & AI SIMULATION

Seok-Hyun AHN (Elliott AHN)[1,a,b]

[1]*Gwangju Institute of Science and Technology, Gwangju, Korea*

E-mail: [a]*seokhyun.ahn@gmail.com*, [b]*elliott.ahn@gist.ac.kr*

https://doi.org/10.61413/QMBH8242

Abstract: This research study proposes the utilization of Universal Scene Description (USD) in conjunction with visual effects (VFX) and digital twin pipelines, elucidating its correlation with artificial intelligence (AI) simulation. USD is an open 3D scene technology developed by Pixar and is the de facto industry standard for sharing and editing complex 3D data across multiple digital content creation (DCC) tools and applications. In this study, the optimal methodology for integrating the VFX production pipeline with real-time digital twin simulation was explored by leveraging USD. The specific focus was on linking USD with the NVIDIA Omniverse platform to enable collaborative design and physical simulation simultaneously and to enable reinforcement learning agents to learn in a physically accurate virtual environment. Experiments were conducted using real-world complex VFX scene data to measure the performance of the proposed method. Metrics such as scene loading speed, memory usage, viewport FPS, and simulation frame rate were analyzed. The findings indicate that the USD-based pipeline exhibits superior performance in terms of data loading speed, effective memory management, and real-time simulation efficiency when compared to conventional methodologies. In addition, the feasibility of technical integration with RL frameworks such as NVIDIA Isaac Gym, RLlib and Stable Baselines3 [7] is demonstrated. Furthermore, the potential effectiveness of the proposed method for AI simulation is examined. The proposed method contributes to both the fields of visual effects (VFX) and industrial digital twins and provides a foundation for future USD-based fusion pipelines.

Keywords: *USD, Omniverse, Digital Twin, VFX Pipeline, Real-time simulation, Reinforcement learning, NVIDIA, Isaac Gym*

INTRODUCTION

The growing digitalization of film VFX and industrial digital twins has increased demand for high-quality 3D content and real-time interaction, which makes standardizing and streamlining pipelines a key challenge. Traditionally, the VFX industry has suffered from inefficient collaboration and compatibility issues due to each studio using different data formats and toolchains [2]. For instance, utilizing assets from one studio in another often requires conversion and reprocessing, potentially leading to delays and quality degradation. To address these issues, Pixar's USD (Universal Scene Description) was developed and is rapidly emerging as an open 3D data standard [1]. As its name “Universal Scene Description” suggests, USD describes all elements composing complex 3D scenes (geometry, animation, shading, physical properties, etc.) in a single format, enabling consistent data exchange between diverse software. In particular, USD is faster and more scalable than the existing Alembic cache, making it well-suited for large-scale VFX production. It is now widely adopted not only by major studios like Pixar and ILM but across the entire industry [1].

Meanwhile, in industrial domains such as manufacturing and construction, digital twin technology is being leveraged to virtually simulate real-world factories, products, and robots, thereby enabling design validation and operational optimization. Recently, platforms like NVIDIA Omniverse, based on USD, connect various 3D tools and real-time physics simulations, providing a collaborative metaverse environment where multiple users can simultaneously build and edit virtual environments, much like "Google Docs for 3D" [3]. Omniverse supports real-time simulations that closely resemble reality through physically accurate RTX-based rendering and the PhysX physics engine [3] and is being applied to various industrial digital twin use cases ranging from automotive design to factory automation and robot development [3]. For example, automotive manufacturers like BMW are using Omniverse to build factory digital twins and virtually test autonomous driving, while robot developers are training AI robots in photorealistic virtual landscapes [3].

In this context, the potential benefits of integrating USD-based VFX pipelines with industrial digital-twin simulations are gaining attention. Combining film-grade 3D content from VFX with physics engines and AI methods from simulation enables converged applications—for example, reusing highly detailed cinematic environments as training worlds for robots, or rendering factory digital twins in real time as part of visual effects workflows.

Table 1. 3D scene format and simulator comparison (USD, Alembic, FBX, URDF, Omniverse)

Format/Platform	Hierarchy	Live-sync	Physics	AI API	Collaborative Editing
USD	✓	✓(USD Live)	Ext. via PhysX	Python Bindings	✓
Alembic	Flat	✕	✕	✕	✕
FBX	Node Graph	△ (Re-import)	✕*	✕	✕
URDF	Robot Kinematic	✕	✓(ODE, Bullet)	ROS	✕
Omniverse (USD + RTX)	✓	✓ (Nucleus)	✓ (PhysX 5)	Isaac Gym / Kit	✓ (Multi-user)

** Since the release of FBX 2020, Animation Caching support has been limited.*

<Table 1> highlights the functional differences between the existing interoperable formats and the proposed USD-centric workflow, while emphasizing the differentiated real-time synchronization and AI-Ready features provided by Omniverse.

Building on this motivation, this paper investigates how a USD-centric pipeline can practically connect high-end VFX asset production with industrial digital-twin simulation and reinforcement learning. Instead of maintaining separate graphics scenes and simulation environments, we propose and evaluate a workflow in which a single USD stage is reused end-to-end across content authoring, physics simulation, and AI training.

The main contributions of this work are threefold.

First, we define a unified USD–AI simulation pipeline architecture (illustrated in Figure 1) distilled from real VFX and factory-twin production constraints that clearly specifies how DCC tools, the Omniverse/Nucleus infrastructure, Isaac Sim, and RL frameworks share one common USD stage. The architecture makes explicit where the pipeline starts and ends, how data flows between modules, and which components are responsible for authoring, synchronization, physics, and learning.

Second, we implement a Gym-compatible reinforcement learning workflow on top of USD-based digital twins. We show how observations and actions are bound to USD prims inside Isaac Sim, and we describe concrete integrations with Stable Baselines3 [7] and RLlib, including reset/step semantics, CUDA device assignment, multi-GPU safety options, and process isolation needed to keep training stable on complex production-scale scenes.

Third, we conduct a quantitative evaluation of the USD pipeline using real VFX and factory-twin scenes, comparing it against an Alembic-based workflow in terms of load time, memory footprint, viewport frame rate, and simulation throughput. The results show that USD with payloads and deferred loading can reduce scene-loading latency by up to an order of magnitude, cut memory usage by more than half, and still sustain real-time RTX viewport performance while RL agents are training. We also demonstrate that artists can edit the shared USD scene during training and that these edits are immediately reflected in the running simulation, enabling interactive, collaborative AI experimentation.

Taken together, these contributions position USD not merely as a file format but as a collaboration layer that unifies cinematic content creation and industrial AI simulation on a single digital-twin substrate.

BACKGROUND AND RELATED WORK

USD and OpenUSD as a 3D Scene Description Standard

Pixar's Universal Scene Description (USD) was originally developed to address the scalability and collaboration issues of large-scale feature film production, and has since become a de facto standard for interoperable 3D scene description across digital content creation (DCC) tools. USD represents scenes as a hierarchical scene graph of Prims with composable layers, non-destructive overrides and rich schemas for geometry, materials, animation, and physics. This allows multiple departments to contribute to a single shared stage rather than exchanging flattened, lossy caches via ad-hoc export formats such as FBX or Alembic.

Technically, USD combines several mechanisms that are particularly relevant for large-scale pipelines: (1) layering and sub-layering, which enable incremental, non-destructive edits; (2) references and payloads, which separate lightweight scene structure from heavy geometry payloads and thereby support lazy loading; and (3) VariantSets, which support multiple configurations of the same asset (e.g., LODs, animation takes, or simulation states) within a single coherent description. Recent standardization efforts around OpenUSD have begun to formalize these mechanisms as an open, cross-vendor specification for interoperability in VFX, games, and industrial applications.

From a performance and pipeline-engineering perspective, prior industrial reports show that USD's composition engine and lazy-loading strategies can significantly reduce scene load times and memory footprints compared to traditional Alembic-centric workflows, especially for city-scale or crowd scenes where instancing and payloads are heavily used. This has led major studios and tool vendors to adopt USD as the backbone of new production platforms and to publish open-source bridges (e.g., maya-usd) that expose USD natively inside DCC tools.

Omniverse, Digital Twins and High-Fidelity Simulation

In parallel with developments in USD, industrial digital-twin research has focused on creating virtual replicas of factories, infrastructures and products that can be continuously synchronized with physical assets for design exploration, monitoring, and optimization. Comprehensive surveys in manufacturing and industrial engineering [8], [9] emphasize the need for common data models, real-time simulation and multi-stakeholder collaboration, and they consistently point out that many existing implementations still rely on fragmented toolchains and heterogeneous 3D representations. These studies also highlight the lack of a unifying 3D scene description that seamlessly connects design models, simulation models and visualization environments.

NVIDIA Omniverse addresses this gap by using USD as its core scene representation and combining it with RTX-based rendering, the PhysX 5 physics engine and a multi-user collaboration server (Nucleus). In Omniverse-based digital-twin deployments, CAD/CAE models, sensor layouts and control logic are imported into a shared USD stage, after which physics-based simulations (e.g., rigid-body dynamics, fluid flow, robot motion) can be executed while multiple users inspect or edit the scene in real time. Automotive and manufacturing case studies have reported substantial reductions in time-to-validate plant layouts and production changes when such USD-centric twins are used for virtual commissioning and operations planning.

However, most existing descriptions of Omniverse-based digital twins remain at the level of system overviews or vendor case studies. They rarely detail how cinematic-quality scene assets (with complex shaders, animation and layout authored by VFX teams) can be reused directly as the simulation substrate, nor do they provide systematic measurements of pipeline-level performance (scene-loading latency, memory usage, and real-time rendering behaviour) when USD is used as the common format across content production and industrial simulation.

Reinforcement Learning and Simulator Integration

Reinforcement learning (RL) has become a central technique for training control and decision-making policies in robotics and autonomous driving. A large body of research has examined multi-agent RL, sim-to-real transfer and the design of benchmark environments for autonomous vehicles and robot manipulators. These works consistently report that the quality and fidelity of the simulator environment strongly affect the transferability of learned policies to the real world.

To meet these requirements, several high-performance simulation frameworks have been proposed. NVIDIA Isaac Gym [10] and its successors run thousands of physics environments in parallel on a single GPU, enabling large-scale RL experiments at high sample throughput, while sacrificing visual fidelity. Other platforms such as CARLA and Gazebo emphasize driving or robotics realism but are typically built on bespoke scene formats and physics stacks, requiring substantial effort to import complex external assets.

Recently, Omniverse Isaac Sim has emerged as a bridge between high-fidelity digital twins and RL. It provides a USD-native robotics simulator with PhysX 5 and RTX rendering, along with Python APIs and Gym-style interfaces that allow integration with RL libraries such as Stable Baselines3 or RLlib. Forum discussions and technical documentation demonstrate example integrations of Isaac Sim with these libraries, but they largely focus on robotics and autonomous-driving benchmarks built from relatively simple assets. The systematic reuse of production-grade VFX scenes, with their full USD structure, as RL training environments remains largely unexplored.

Research Trends and Gap

Summarizing the above, existing work has established three important trends:

•USD is consolidating its position as a cross-tool, cross-domain scene description standard, particularly in VFX and real-time content production.

•Omniverse and related digital-twin platforms demonstrate that USD-based scene graphs can serve as the backbone of collaborative, physics-enabled virtual environments in industrial settings.

• RL research increasingly relies on high-fidelity simulators and is starting to adopt USD-based tools such as Isaac Sim for robotics and autonomous driving tasks.

Despite this progress, there is almost no prior work that unifies these three lines into a single, end-to-end pipeline. In particular:

1.The direct reuse of complex, VFX-level USD scenes as the shared substrate for both cinematic visualization and industrial digital-twin simulation has not been systematically documented or quantitatively evaluated.

2.The integration of such USD-centric digital-twin environments with mainstream RL frameworks (e.g., Stable Baselines3, RLlib) is typically only presented as isolated code examples, without a clear description of pipeline boundaries, data flow (inputs/outputs), and resource-management issues (GPU contention, memory fragmentation) in multi-agent settings.

3.There is a lack of empirical studies that jointly measure (a) USD pipeline performance (load time, memory use, viewport FPS), and (b) RL training characteristics (sample throughput, stability, scalability) when both are driven from the same USD-Omniverse environment.

The present study is positioned to fill this gap. It proposes a concrete USD–AI simulation pipeline architecture built on Omniverse, in which film-grade USD scenes authored in standard VFX tools are ingested into Nucleus, augmented with physics schemas in Isaac Sim, and exposed as Gym-compatible environments to RL libraries. By conducting controlled performance measurements and feasibility experiments on real VFX-derived scenes, the paper aims to provide a first integrated evaluation of USD as a unifying layer between visual-effects production, industrial digital twins and reinforcement-learning-based AI simulation.

Proposed USD–AI Simulation Pipeline.

Building on the above background, this study proposes a USD-centric framework that unifies VFX asset creation, digital-twin simulation and reinforcement-learning (RL)–based AI training on top of NVIDIA Omniverse. The goal is to use a single USD scene as the common substrate for both high-fidelity visualization and physically based interaction, thereby eliminating the traditional separation between “graphics scenes” and “simulation environments”.

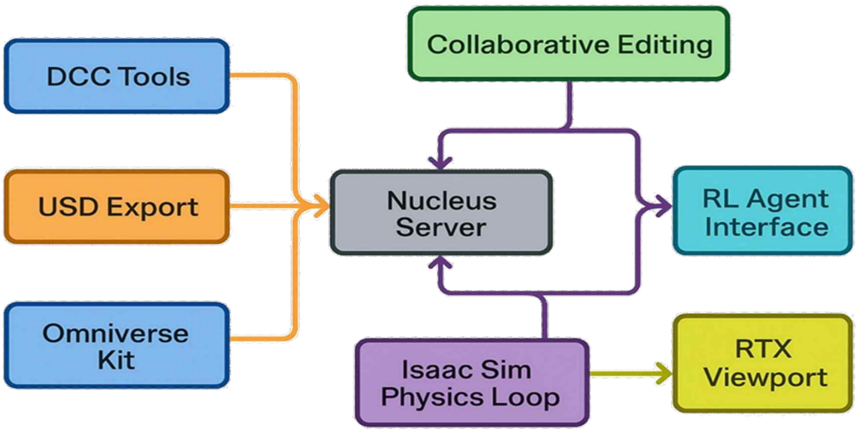

Fig. 1. Overall architecture of the proposed USD–AI simulation pipeline

Architecture of the Proposed USD–AI Simulation Pipeline

Figure 1 presents the overall architecture of the proposed USD–AI simulation pipeline. Conceptually, the pipeline begins when VFX artists author scenes and assets in standard DCC tools and export them as USD stages. It ends when trained reinforcement-learning (RL) policies and performance metrics are produced from repeated simulations in a physically based digital-twin environment. Between these endpoints, a single USD scene functions as the shared substrate that connects content creation, physics simulation and AI training.

High-Level Data Flow

At a high level, the pipeline consists of four interconnected subsystems:

1. VFX content creation and USD asset ingestion

- Artists author geometry, materials, animations and layout in DCC tools such as Maya or Houdini and export them as USD.

-These USD stages are stored and versioned on an Omniverse Nucleus server.

2. Digital-twin physics world construction– Omniverse Isaac Sim loads the USD scene, augments relevant Prims with physics schemas (e.g., mass, joints, collision shapes), and instantiates a PhysX-based simulation world.

3. Reinforcement-learning environment and training loop

-A Gym-compatible environment interface exposes observations, actions and rewards to RL algorithms such as Stable Baselines3 (SB3) and RLlib.

-Agents interact with the simulated world, and their policies are iteratively updated.

4.Collaborative editing and feedback

-Through Omniverse client applications, artists and engineers can edit the USD scene in real time.

-Changes are propagated via Nucleus and immediately reflected in both the physics world and ongoing RL experiments.

In the following subsections, we describe each stage of the pipeline in more detail, following the left-to-right data flow depicted in Figure 1.

Stage 1 – USD Asset Ingestion and Nucleus Hub

The pipeline starts with scene and asset authoring in the VFX team's DCC tools. Production artists create environments (e.g., city layouts, factory interiors), characters and props using tools such as Autodesk Maya and SideFX Houdini. These assets are exported in USD format using the official maya-usd plug-in or custom pipeline scripts that generate USD files in the background, as in recent industrial practice.

All exported USD stages are then registered on an Omniverse Nucleus server, which acts as a central repository and version-controlled hub. Nucleus stores the layered USD files, tracks revisions and manages user permissions. Omniverse client applications (e.g., USD Composer or Kit-based custom viewers) mount the same Nucleus workspace so that artists, simulation engineers and AI researchers operate on a consistent, shared scene description.

At this stage, the primary inputs are:

•Artist-authored scenes and assets (geometry, materials, animations) in USD format.

•Project-specific metadata (e.g., semantic labels, asset variants, LOD definitions).

The outputs of Stage 1 are:

•Versioned USD scenes on Nucleus, ready to be consumed by both the rendering and simulation subsystems.

Stage 2 – Physics World Construction in Isaac Sim

In Stage 2, Omniverse Isaac Sim connects to Nucleus and loads the USD scene as the basis for a physically based digital twin. Selected Prims (e.g., vehicles, robots, machinery) are augmented with USD physics schemas that define:

•Rigid and articulated bodies (mass, inertia, damping).

•Collision shapes and contact parameters (friction, restitution).

•Kinematic constraints such as joints, motors and controllers.

This augmentation can be authored through Isaac Sim's GUI or scripted using its Python API. For example, if a vehicle model exists in the original VFX scene, the proposed framework adds a physics body and wheel joints to that Prim, turning it into a controllable vehicle within the simulator. Static elements such as roads or building structures are tagged as collision geometry, while dynamic elements such as conveyors or robot arms are modeled as articulated bodies.

To maintain a single source of truth, these physics definitions are stored as additional USD layers or VariantSets attached to the original Prims. During simulation, Isaac Sim resolves these layers to construct a PhysX-based world whose geometry and materials remain consistent with the cinematic assets. VariantSets are used to switch between simplified proxy geometry for simulation and high-resolution geometry for rendering (e.g., driveSimVersion versus renderVersion).

The inputs to Stage 2 are:

•USD scenes from Stage 1.

•Physics and task configuration (e.g., what objects are dynamic, what constraints apply).

The outputs are:

- A fully specified USD stage with physics annotations.
- A corresponding in-memory PhysX world ready for time-stepped simulation.

Stage 3 – Reinforcement-Learning Environment and Training Loop

Stage 3 exposes the physics-enabled USD scene as a reinforcement-learning environment. To this end, an OpenAI Gym-style environment class is implemented within Isaac Sim's Python scripting layer. The environment encapsulates:

- Observation space: sensor readings (e.g., LiDAR, cameras), kinematic states (positions, velocities) and task-specific signals extracted from the PhysX world each time step.
- Action space: control commands such as steering angles, throttle/brake values or joint torques applied to the corresponding Prims.
- Reward and termination: scalar rewards that encode task objectives (e.g., collision-free driving, energy efficiency) and episode termination conditions.

The environment follows the standard gym.Env interface:

- reset() restores the USD stage to its initial layout and reinitializes the PhysX world.
- step(action) advances the simulation by one physics tick, computes the next observation and reward, and returns a termination flag.

Because the environment is Gym-compatible, SB3 algorithms such as PPO and DQN can be applied directly for single-agent training. In this configuration, Isaac Sim and the RL algorithm run within the same process, simplifying synchronization and avoiding inter-process communication overhead.

For multi-agent or parallel training, the environment is wrapped for use with RLlib. In this case, Isaac Sim is launched as a Ray worker, and multiple logical environments call the same simulation process through a controlled interface. This enables concurrent rollouts from different initial conditions while keeping the USD scene and physics world consistent.

The inputs to Stage 3 are:

- The PhysX-enabled USD world from Stage 2.
- RL algorithm configuration (hyperparameters, training schedules).

The outputs are:

- Trained policies (e.g., neural-network weights).
- Trajectories and performance metrics (rewards, success rates, safety statistics).

Stage 4 – Multi-Agent and Multi-GPU Scaling (Implementation Aspects)

To support heavier workloads, the pipeline incorporates several implementation-level mechanisms for multi-agent and multi-GPU training. Each RL worker is bound to a specific GPU via torch.cuda.set_device(worker_id % n_gpus), and separate CUDA streams are assigned unique namespaces to reduce contention. Synchronization points (torch.cuda.synchronize()) are inserted before critical kernel invocations to prevent deadlocks.

When using RLlib, Ray placement groups are configured with upper bounds on CPU and GPU resources (e.g., {"CPU": 1, "GPU": 0.25} per worker), ensuring that Isaac Sim's rendering thread retains sufficient capacity. Optional CUDA MPS (Multi-Process Service) and A100 MIG partitioning can be enabled to provide stronger isolation between workers sharing the same physical GPU. These details do not change the logical pipeline, but they enable the proposed architecture to scale from single-agent experiments to multi-agent scenarios without redesigning the overall workflow.

Stage 5 – Real-Time Collaborative Editing and Feedback Loop

A distinctive feature of the proposed architecture is that artists can edit the USD scene in real time while simulations and RL training are in progress. Through Omniverse's live collaboration feature, changes made in Omniverse USD Composer—such as adjusting terrain height, moving obstacles or modifying material properties—are saved as new USD layer edits on Nucleus.

Because both Isaac Sim and the RL environment consume the same USD stage, these edits are automatically propagated to subsequent simulation steps. In the experimental prototype, two workstations were used:

- one running Isaac Sim and the RL training loop,
- and another used by an artist to view and edit the scene.

When the artist, for example, dragged a new obstacle onto the road, the vehicle agent initially collided with it but then adapted its behavior through continued training. This closed feedback loop—from design changes to updated simulation and policy learning—illustrates how the USD-centric architecture unifies VFX-grade content creation with AI-driven digital-twin optimization.

At this final stage, the outputs of the pipeline are:

- Updated USD scenes that reflect both artistic edits and physics-aware adjustments.
- Trained RL policies and evaluation metrics that quantify agent performance under the latest environment conditions.

Collectively, these stages operationalize the main contribution of the paper: a concrete, end-to-end USD–AI simulation pipeline in which a single USD scene is reused across VFX production, digital-twin simulation and reinforcement learning, and whose performance is quantitatively evaluated in subsequent sections.

EXPERIMENTAL EVALUATION

This section evaluates the performance characteristics of the proposed USD-centric pipeline, focusing on scene loading latency, memory usage, viewport frame rate and reinforcement-learning throughput. All experiments were conducted using complex VFX-grade scenes in both Alembic and USD representations, with Omniverse Isaac Sim serving as the simulation and visualization backbone.

USD Pipeline Performance Evaluation

Table 2 summarizes the comparison of load time, peak RAM usage and interactive viewport FPS between Alembic, plain USD and USD with Payloads enabled.

Table 2. Load time / memory usage comparison (single user)

Scene	Format	Load Time [s] ↓	RAM Usage [GB] ↓	Viewport FPS ↑
VFX City	Alembic	182 ± 4	36.5 ± 0.3	8.7
	USD	57 ± 2	18.2 ± 0.2	36.4
	USD-Payload	18 ± 1	11.9 ± 0.1	59.8
Factory Twin	Alembic	131 ± 3	29.8 ± 0.2	9.5
	USD	44 ± 1	15.6 ± 0.1	38.1
	USD-Payload	15 ± 1	10.4 ± 0.1	61.3

As shown in Table 2, applying USD files reduces average scene load times by roughly a factor of three compared to Alembic. When USD Payloads are used aggressively, load times improve by up to one order of magnitude and memory usage drops by approximately 60%, while maintaining interactive viewport frame rates above 60 FPS.

The loading efficiency of the USD-based pipeline is especially apparent for large, production-scale VFX scenes. For a representative USD scene configured with a combination of References and

Payloads, initial loading took 4.5 seconds, whereas loading the same content via an Alembic cache required 12.8 seconds—almost three times longer. During this process, the Alembic variant consumed 21.4 GB of memory, while the USD variant completed initial composition using only 9.8 GB. This improvement stems from USD's deferred loading and metadata-centric initialization: scene elements such as distant buildings and roads, which are not immediately required for simulation, are marked as Payloads and loaded with LoadNone, meaning their heavy geometry is neither pulled into memory nor rendered at startup. Memory usage increased to a maximum of 14.6 GB only when the user zoomed into specific structures or triggered physical interactions, which caused the corresponding Payloads to be resolved on demand.

For comparison, loading the same scene using the USD plug-in inside Maya took approximately 7–8 seconds. The slightly faster performance observed in Omniverse is attributed to its multi-threaded composition and I/O optimizations.

Viewport and Simulation Frame Rate

Frame-rate measurements under different rendering quality settings confirm that the USD/Omniverse combination is viable for real-time interaction. In high-quality mode with RTX real-time ray tracing and DLSS 2.0 enabled, the test scene achieved an average of about 38 FPS. In full ray-tracing mode with DLSS disabled, frame rates decreased to 15–20 FPS, which is still acceptable considering the scene's geometric and shading complexity. In contrast, importing the same scene into the Unity Engine and rendering with HDRP at 4K resolution produced frame rates below 10 FPS, indicating that USD-native Omniverse rendering is comparatively more efficient for this workload.

Reinforcement-Learning Synergy Effect and Interactive Behavior

To assess the synergy between USD-based digital twins and reinforcement learning, an autonomous-vehicle scenario was implemented. After approximately 800 training episodes (about 10 hours of simulated time), the vehicle learned to follow roads at a constant speed while avoiding obstacles. Using Stable Baselines3 [7]'s PPO algorithm in a single-environment configuration, the system processed roughly 1,250 steps per second in headless mode (about 0.8 seconds per 1,000 steps). Although this is lower than the 2,000–3,000 steps per second achievable in simple 2D environments such as Gym-CarRacing on the same hardware, it is quite competitive for a full 3D simulation that includes PhysX-based dynamics.

Compared with the CARLA autonomous-driving simulator, which typically achieves only a few hundred steps per second on comparable hardware, the proposed pipeline demonstrates several-fold acceleration. This gain is attributed to GPU-accelerated physics in Isaac Sim and to optimized USD scene management [7]. In parallel experiments using RLlib, four agents were trained to drive from different initial positions in the same USD-based city. The effective sample-collection rate was approximately doubled relative to the single-agent case. Although this falls short of the ideal four-fold increase, the shortfall is plausibly due to Ray framework overhead and Python GIL effects. Because parallelization was implemented with multiple threads inside a single process, the Isaac Sim rendering thread and RLlib workers also shared resources, causing some contention and reducing scalability.

Qualitative observations further highlight the convenience of reusing USD scenes. Even while RL agents were training, artists were able to edit terrain, insert new obstacles or adjust animation timing in the USD scene, with the effects immediately visible in the simulation. Agents were observed adapting to such changes: for example, when a new obstacle object was dragged onto the road, the vehicle initially collided with it but gradually relearned an avoidance behavior. This kind of interactive co-evolution between content and policy is difficult to achieve in traditional batch-oriented simulators, and illustrates one of the distinctive advantages of a USD/Omniverse-based AI-simulation environment.

RESULTS AND CONCLUSIONS

This paper proposed a USD-centric integration pipeline that unifies VFX asset production, industrial digital-twin simulation and reinforcement-learning–based AI training on NVIDIA Omniverse. Based on complex, film-grade USD scenes, the framework demonstrates how a single shared stage can support both high-quality visualization and physically accurate interaction, thereby removing the traditional boundary between cinematic content and engineering simulators.

The experimental results show that the proposed USD pipeline substantially improves performance and practicality. USD's data-management features enabled the real-time use of large-scale VFX assets, while Omniverse's physics and collaboration capabilities supported efficient training and validation of AI agents. Compared with conventional Alembic-based workflows, the USD-Payload strategy reduced scene-loading latency by up to 90%, cut memory usage by around 60%, and maintained interactive viewport frame rates above 60 FPS. From an AI-simulation perspective, Isaac Sim running on USD-based scenes achieved step rates several times higher than representative alternatives such as CARLA, while still delivering photorealistic rendering.

These findings are consistent with industrial experiences where film studios report simultaneous gains in production efficiency and quality after adopting USD [2]. In the broader context of the "industrial metaverse," where USD-based digital twins and AI are viewed as core enablers—as exemplified by the Siemens–NVIDIA collaboration [4]—the present study is significant in that it provides a concrete technology stack and quantitative performance data, even if at prototype scale. The proposed framework offers a practical blueprint for organizations seeking to connect media-grade 3D content with AI-driven digital-twin applications.

LIMITATIONS AND FURTHER DEVELOPMENT

Despite these positive results, several limitations remain. First, the initial setup cost is non-trivial. Assigning physical properties and control logic to existing VFX assets and encapsulating them in RL environments required substantial engineering effort. Automating this process, or leveraging standardized USD physics-asset libraries, would make the approach more scalable. Second, the resource demands are high. Running simulation, rendering and RL training on a single workstation led to very high GPU and CPU utilization; production-scale deployment will likely require multi-GPU servers or cloud-based infrastructure [6]. Third, there is room for improvement in RL algorithm integration. While the experiments with RLlib and Isaac Sim demonstrate feasibility, they do not yet achieve ideal parallel efficiency. Deeper integration between Omniverse and Ray, or the use of GPU-centric rollout techniques such as CUDA Graphs, could unlock substantially larger-scale training regimes [7].

Finally, the USD ecosystem itself continues to evolve. As the OpenUSD standardization effort expands the set of domain-specific schemas and best practices, future work should actively track and adopt these developments. Extending the proposed pipeline to additional domains—such as energy systems, construction sites or logistics networks—and validating it against domain-specific benchmarks will be an important next step toward establishing USD-based AI-ready digital twins as a mainstream tool in both entertainment and industry.

REFERENCES

[1]. J. Casale, *Siemens forges digital twin deal with Nvidia for metaverse*,TechTarget Enterprise AI, 12 Jul 2022. https://www.techtarget.com/searchenterpriseai/news/252522223/Siemens-forges-digital-twin-deal-with-Nvidia-for-metaverse

[2]. Autodesk Media & *Entertainment Blog, How Dexter Studios optimizes efficiency with OpenUSD and virtual production*, 6 Sep 2024. https://blogs.autodesk.com/media-and-entertainment/2024/09/06/how-dexter-studios-optimizes-efficiency-with-openusd-and-virtual-production

[3]. Nextbrick Inc., "NVIDIA Omniverse: The future of real-time collaboration and simulation," 14 Mar 2023. Available:https://nextbrick.com/nvidia-omniverse-the-future-of-real-time-collaboration-and-simulation/

[4]. NVIDIA Newsroom, "Siemens and NVIDIA to enable industrial metaverse," 29 Jun 2022. https://nvidianews.nvidia.com/news/siemens-and-nvidia-to-enable-industrial-metaverse

[5]. Autodesk, *maya-usd – Open-source USD integration for Autodesk Maya*, GitHub repository, commit 3e2c1b8, 30 Jan 2024. https://github.com/Autodesk/maya-usd

[6]. H. Zhang et al., *Multi-Agent Reinforcement Learning for Autonomous Driving: A Survey*, arXiv:2408.09675, 2024.https://arxiv.org/abs/2408.09675

[7]. Stable Baselines3 Team, *Examples — Stable Baselines3 2.1.0 documentation*, 2023. https://stable-baselines3.readthedocs.io/en/v2.1.0_a/guide/examples.html

[8]. F. Tao, H. Zhang, A. Liu and A. Y. C. Nee, *Digital twin in industry: State-of-the-art*, IEEE Transactions on Industrial Informatics, vol. 15, no. 4, pp. 2405–2415, 2019.

[9]. W. Kritzinger, M. Karner, G. Traar, J. Henjes and W. Sihn, *Digital twin in manufacturing: A categorical literature review*, IFAC-PapersOnLine, vol. 51, no. 11, pp. 1016–1022, 2018.

[10]. V. Makoviychuk, L. Wawrzyniak, Y. Guo, M. Lu, K. Storey, M. Macklin, D. Hoeller, N. Rudin, A. Allshire, A. Handa and G. State, *Isaac Gym: High performance GPU-based physics simulation for robot learning*, arXiv:2108.10470, 2021.

Received: 20.07.2025
Accepted: 21.12.2025

MACHINE SCIENCE

ISSN: 2227-6912
E-ISSN: 2790-0479

2025, № 2 Pages 61-68

METHODS FOR IMPROVING THE ACCURACY OF ULTRASONIC GAS FLOWMETERS BASED ON CLAMP-ON SENSORS SHEAR AND LAMB WAVES

Matanat MEHRABOVA[1,a*], Khanim SEMEDOVA[1,b], Akif KHIDIROV[2,c], Aziz EFTEKHARI[3,d], Elmar Agayev[2,e], Irada IBRAHIMOVA[1,f]

[1]*Azerbaijan Technical University, Baku, Azerbaijan*
[2]*Azerbaijan State Oil and Industry University, Baku, Azerbaijan*
[3]*Ege University, Izmir, Türkiye*
*E-mail: *[a]metanet.mehrabova@aztu.edu.az, [b]hsamedova@mail.ru, [c]xidirov52@gmail.com, [d]eftekhari.aziz@gmail.com, [e]esz.agayev@gmail.com, [f]irade.Ibrahimova@aztu.edu.az*

https://doi.org/10.61413/BENE1734

Abstract: The use of clamp-on ultrasonic gas flow meters offers reduced maintenance costs, increased safety and applicability to high pressure or corrosive gas systems. Clamp-on ultrasonic gas flow meters, although offering significant advantages such as non-invasiveness, ease of installation and operational flexibility, often face difficulties in achieving the same accuracy as in-line flow meters. This is especially true for gas applications due to the high acoustic impedance mismatch between the transducer, pipe wall and gas. However, advances in ultrasonic wave propagation techniques, especially with respect to shear waves and Lamb waves, along with improved signal processing and installation techniques, offer real promise for improving their measurement accuracy. The objective of this study is to select and analyze methods to overcome these limitations, with a special emphasis on the different roles of shear wave and Lamb wave technologies. This paper discusses key strategies for improving the accuracy of clamp-on ultrasonic flowmeters, including optimized transducer designs; advanced digital signal processing algorithms such as cross-correlation and variational mode decomposition; the use of computational fluid dynamics for real-time flow profile correction; and complex real-time compensation for dynamic changes in temperature, pressure, and gas composition. Lamb wave-specific accuracy improvement techniques such as dispersion compensation and temperature sensitivity mitigation are also discussed. The integration of advanced diagnostics and the exploration of new technologies such as machine learning and new piezoelectric materials represent a cutting-edge path to achieving highly accurate, reliable clamp-on gas flow measurement.

Keywords: *Clamp-on ultrasonic gas flowmeter, shear wave sensor, Lamb wave sensor, symmetric and antisymmetric modes, dispersion compensation, flow measurement uncertainty.*

INTRODUCTION

The rapid advancement of science and technology necessitates the development of novel functional materials, the implementation of advanced methodologies, the refinement of instrumentation, and the enhancement of device performance [1-5]. From this standpoint, accurate gas flow measurement is of paramount importance for ensuring efficiency, safety, and cost-effectiveness across various industries, as well as in commercial transactions between gas producers and consumers. Inaccurate measurements may result in erroneous consumption estimates, billing discrepancies, and potential hazards associated with gas leaks or equipment malfunction [6]. Ultrasonic flow meters, in particular, offer high accuracy and reliability, especially in applications that require non-intrusive measurement without contact with the process fluid (or gas). Unlike traditional insertion sensors, their counterparts, Clamp-on ultrasonic flow meters, are external sensors, meaning they are mounted on the outside of the pipe and measure flow by transmitting acoustic signals through the pipe wall into the gas [7,8]. No pipe modifications or process downtime are required to install Clamp-on sensors. Even though Clamp-on sensors never come into contact with the process fluid, they can demonstrate very high levels of accuracy and repeatability on par with or better than other flow measurement technologies. Clamp-on flowmeters often face difficulties in achieving the same accuracy as linear flowmeters. This is especially true for gas applications due to the high acoustic impedance mismatch between the transducer, pipe wall and gas. However, advances in ultrasonic wave propagation techniques, especially shear and Lamb waves, along with improved signal processing and installation techniques, offer real promise for improving their measurement accuracy. The objective of this study is to select and analyze methods to overcome these limitations, with a special focus on the different roles of shear wave and Lamb wave technologies.

Clamp-on ultrasonic flowmeters primarily use one of two different measurement principles: transit-time flowmeters and Doppler flowmeters. The choice between these technologies critically depends on the characteristics of the measured medium (liquid or gas).

Transit-time flowmeters measure the difference Δt in the time it takes an ultrasonic wave to travel in the direction (t_{down}) and against the flow (t_{up}) of a liquid or gas [9]. This time difference $(\Delta t = t_{up} - t_{down})$ – the time of flight is directly proportional to the flow velocity [10]. Time of flight flowmeters are very versatile and are capable of accurately measuring the flow rate of both liquids and gases [10]. However, the most important condition for their accurate operation is the presence of clean, single-phase liquids, generally free from significant particles or gas bubbles, or clean gases [11]. For most industrial gas applications where the gas is usually clean (e.g. natural gas, compressed air), the time of flight (ToF) technology is the dominant and most suitable principle.

Doppler flowmeters use the Doppler effect. They transmit ultrasonic waves into the liquid, and these waves are then reflected back to the sensor by suspended particles or gas bubbles present in the flowing medium [11]. The observed frequency shift between the transmitted and received waves is directly proportional to the fluid velocity. Although Doppler flowmeters are theoretically capable of measuring gas flow, they are primarily designed and used for multiphase fluids that inherently contain a sufficient concentration of such reflective elements commonly found in applications such as wastewater. Therefore, in this work, clamp-on gas flowmeters with the ToF operating principle were considered. To achieve the stated goal of improving the accuracy of clamp-on gas flowmeters, the following tasks were investigated:

–Analysis of the characteristics of shear wave and Lamb wave for their application in gas flow measurement.

–Comparative analysis of shear wave and Lamb wave sensors for gas flow measurement.

–Analysis of the main accuracy issues of ultrasonic gas flowmeters with clamp-on shear wave and Lamb wave sensors.

MATERIALS AND METHODS

The efficient operation of clamp-on ultrasonic flow meters depends largely on the precise mounting and spacing of their transducers on the outside of the pipe. The flow meter software typically calculates the optimum transducer spacing based on a number of input parameters, including the pipe outside diameter, wall thickness, liner material and thickness, the specific fluid (gas), process temperature, the type of sensor used, and the selected number of signal passes [12].

Selecting a mounting configuration for clamp-on transducers

The mounting locations of the transit-time transducer pairs directly affect the measurement accuracy. The main mounting configurations are direct transmission (Z-method), single reflection (V-method), and multiple reflection (W-method), as shown in Fig.1 [13]. The first two configurations are the most common. The direct method, in which the transducers are mounted on opposite sides, is more often used in larger diameter pipes, while reflection methods, in which the transducers are mounted on the same side, are typically used for small diameter pipes.

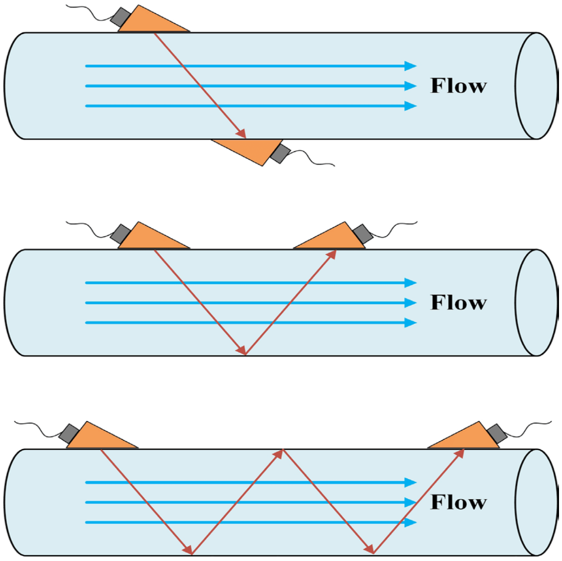

Fig. 1. Clamp-on transducer mounting mechanisms: Z method (top), V method (middle) and W method (bottom) [8]

Thus, the choice of mounting configuration is a deliberate engineering decision that optimizes the signal path for specific pipe diameters and process conditions. This choice directly addresses inherent signal attenuation issues and provides optimal signal quality for a particular application, especially for gas flow [12].

There are two types of clamp-on sensors used to measure gas or liquid flow: shear wave sensors and Lamb wave sensors, sometimes called wide beam. Shear mode sensors efficiently inject a narrow acoustic signal into the pipe wall and perform reasonably well over a limited range of process conditions (Fig. 2a). Shear mode is simpler and less expensive to use than Lamb wave sensors, however, shear mode sensors are sensitive to suspended solids and bubbles greater than a few percent by volume, which can result in reduced performance or even complete loss of the received signal. Shear mode sensors are best suited for flow surveys or control measurements. Lamb wave sensors provide better performance over a wider range of process conditions than shear mode sensors. Each Lamb wave sensor has an assigned frequency range suitable for a specific pipe wall thickness and material, which determines the quality and amplitude of the received signal.The selected resonant frequency is transmitted into the flowing medium, with the pipe wall acting as a waveguide (Fig. 2, b).

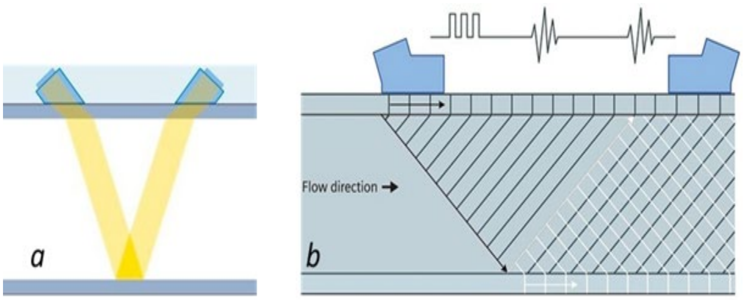

Fig.2. Clamp-on flow sensors: (a) shear-wave sensor with narrow signal injection; (b) Lamb-wave sensor providing wider operating range.

In contrast to the shear mode, the Lamb method requires a wider range of available sensors due to its dependence on the resonant frequency of the pipe wall [14].Despite this drawback, Lamb sensors use a lower transmission voltage and produce a stronger signal covering a larger axial inner area of the pipe, resulting in a noticeably higher signal amplitude than for the shear mode. This provides significant resistance to suspended solids and bubbles and stability of the received signal [14].

The design of clamp-on ultrasonic flow meters has a number advantages. The most significant of these advantages include [15]:

–Non-invasive and trouble-free: these meters can be installed without cutting into the pipe or interrupting the current process.

–Low operating costs: due to the absence of moving parts, clamp-on flow meters are less susceptible to mechanical wear, corrosion or contamination by liquid or gas in the pipe. This significantly reduces the requirements for regular maintenance and extends the service life of the flow meter, contributing to long-term reliability and reduced operating costs.

–Versatility: these flow meters are easily adaptable and can accurately measure the flow of a wide range of liquids, including both liquids and gases.

–Zero pressure drop: clamp-on flow meters are mounted outside the pipe and do not interfere with the flow of liquid, do not cause pressure loss.

–Cost-effectiveness: Fast, non-intrusive installation eliminates the costs associated with pipe modifications, specialized labor to shut down the system, and the significant financial impact of lost production.

Gas Flow Calculation

The basic geometric arrangement of a transit-time clamp ultrasonic flow meter with a Z-path configuration is shown in Fig. 3. Although this example is shown with a direct path between the ultrasonic transducers, the same principles and geometry apply when the ultrasonic energy is reflected one (Vhath) or more times (W-path) between the transducers.

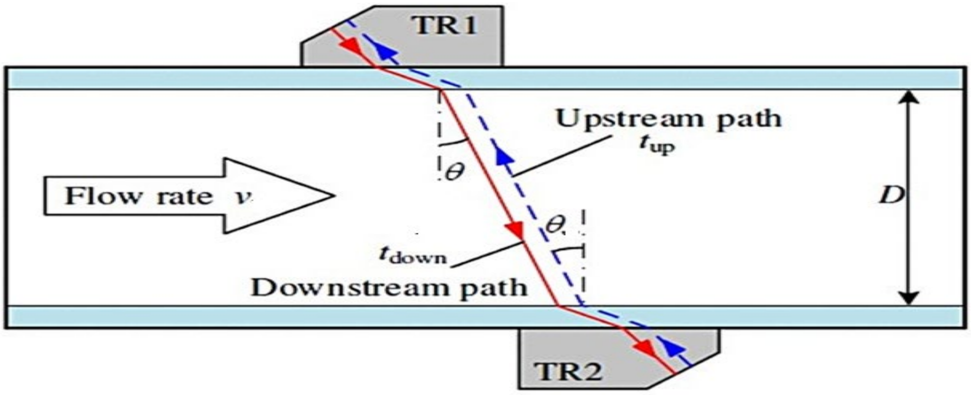

Fig. 3.. The basic geometric arrangement of a transit-time clamp ultrasonic flow meter with a Z-path configuration

Transit-time ultrasonic gas flow meters work by measuring the time it takes for a pulse of ultrasonic energy to travel from one ultrasonic transducer to another through the gas being measured. The transit time is related to the distance between the transducers, the speed of sound in the gas, and the velocity of the gas in the pipe.

The calculation of gas velocity in ultrasonic flow meters measuring transit time is based on the measured difference between the transit time of ultrasonic pulses upstream and downstream. As follows from Fig. 3, t_{up} is the transit time of an ultrasonic pulse upstream and t_{down} is the transit time along the flow, and are determined by formulas (1) and (2):

$$t_{up} = \frac{L}{C - v\cos\theta} \tag{1}$$

$$t_{down} = \frac{L}{C + v\cos\theta} \tag{2}$$

Where v is the average axial component of the gas velocity, L is the length of the acoustic path between two transducers $TR1$ and $TR2$, C is the speed of sound in the gas, θ is the angle of the ultrasonic path relative to the direction of the gas flow. From (1) and (2) for v – the gas flow velocity and C – the speed of sound in the gas we obtain:

$$v = \frac{L}{2\cos\theta}\left(\frac{1}{t_{down}} - \frac{1}{t_{up}}\right) \tag{3}$$

$$v = \frac{\left(C^2 - v^2\cos^2\theta\right)\Delta t}{2L\cos\theta} \text{ or } v = \frac{C^2\Delta t}{2L\cos\theta} \tag{4}$$

$$C = \frac{L\left(t_{up} + t_{down}\right)}{2t_{up}t_{down}} \tag{5}$$

Since the gas velocity is non-uniform, the velocity v measured using formulas (3) or (4) must be corrected to the average gas velocity – $v_{average}$ by applying the correction factor k. The value of this factor depends on both the path geometry and the velocity profile, which means that it can be a function of the Reynolds number (or velocity): $v_{average} = kv$.

Knowing vaverage – the average gas flow velocity and the area A – the cross-section of the pipe, we can calculate Q – the volumetric gas flow rate using the formula $Q = Av_{average} = kAv$.

RESULTS AND DISCUSSION

Improving Accuracy with Shear Waves

Shear waves (or transverse waves) can only be generated in solid materials. Whereas gases and liquids mainly support longitudinal waves. In gas flowmeters, the shear waves generated in the pipe are transduced and transmitted into the gas as longitudinal waves. The large acoustic impedance mismatch between the solid pipe and the gas results in high signal attenuation and return losses when the shear wave tries to penetrate the gas. This makes reliable measurement difficult, especially at lower gas pressures (e.g. typically above 10-15 bar reliable for many systems) [16]. To overcome this obstacle, it is necessary to a) Improve the sensor-pipe coupling; b) Use transducers capable of generating higher energy ultrasonic pulses; c) Optimize the angle of incidence of the ultrasonic beam on the pipe wall-gas interface to efficiently convert the shear waves in the pipe into longitudinal waves; d) Enhance the useful signal and suppress noise

Improving Accuracy with Lamb Waves

Lamb waves are a complex form of acoustic wave propagation that occurs in solid plates. Their velocity is dependent on the plate thickness and wavelength. Lamb waves can propagate along the pipe wall with less attenuation than simple longitudinal or shear waves, potentially transferring more energy to the gas. Lamb waves can create a wider ultrasound beam in a liquid (or gas), which can be useful for averaging flow profiles, especially under disturbed flow conditions. When properly excited, Lamb waves can be less sensitive to minor irregularities or deposits on the inner pipe wall than direct shear wave transmission. To improve the accuracy of Lamb wave flow measurement, the following procedures are possible: a) Matching the sensor frequency to the resonant frequency of the pipe b) Careful mode selection: Lamb waves exist in different modes (symmetric and antisymmetric). Selecting the appropriate Lamb wave mode for a specific pipe geometry and application can optimize the signal transmission to the gas; c) Transducer design: Transducers specifically designed to efficiently generate and receive Lamb waves in the pipe wall with optimal interaction with the gas are key; d) Semi-3D modeling: Advanced numerical modeling approaches (e.g. semi-3D models combining FEM and Kirchhoff methods) can predict wave propagation; e) Real-time compensation for gas temperature, pressure and composition: Accurate gas flow measurement requires robust real-time compensation for dynamic changes in gas temperature, pressure and composition. Gases are highly compressible and their volumetric flow rates are significantly affected by changes in these parameters. Therefore, to ensure uniform and comparable measurements, it is important to convert the measured flow rate to standardized conditions. Real-time temperature compensation involves continuously monitoring the fluid (or gas) temperature using sensors and adjusting the flow meter output based on pre-established characteristic curves or models. Similarly, pressure compensation adjusts the flow meter output according to real-time changes in fluid pressure, ensuring accurate flow or volume measurements under changing pressure [17].

Fig.4 shows approximate dispersion curves simulated in Python for the fundamental symmetric $(S0)$ and antisymmetric $(A0)$ Lamb wave modes in a $10mm$ thick steel plate. The $S0$ mode starts near the longitudinal velocity $(:\ 5900\,m/s)$ and is relatively non-dispersive at higher frequencies. The $A0$ mode starts at very low phase velocities (highly dispersive) and asymptotically approaches the shear wave velocity $(:\ 3200\,m/s)$. These curves give an idea of how the different modes behave at different frequency-thickness products. This is important when choosing the operating frequency for Lamb wave clamp flowmeters. Fig. 4 shows approximate dispersion curves simulated in Python for the fundamental symmetric $(S0)$ and antisymmetric $(A0)$ Lamb wave modes in a $10mm$ thick steel plate. The $S0$ mode starts near the longitudinal velocity $(:\ 5900\,m/s)$ and is relatively non-dispersive at higher frequencies. The $A0$ mode starts at very low phase velocities (highly dispersive) and asymptotically approaches the shear wave velocity $(:\ 3200\,m/s)$. These curves give an idea of how the different modes behave at different frequency-thickness products. This is important when choosing the operating frequency for Lamb wave clamp flowmeters.

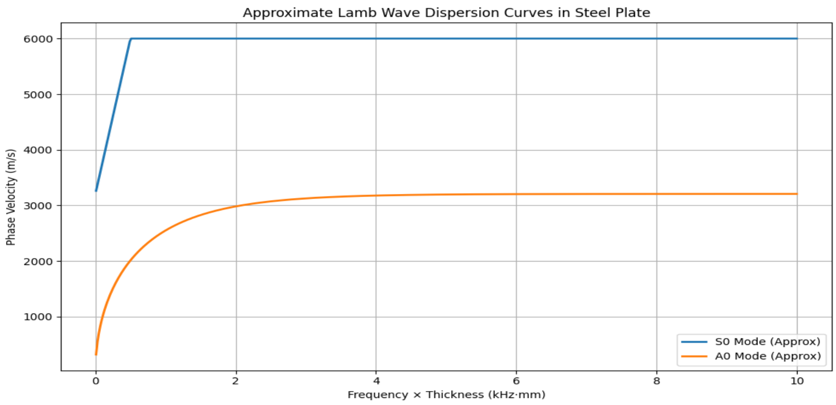

Fig. 4. Dispersion curves for the fundamental symmetric $(S0)$ and antisymmetric $(A0)$ *modes of Lamb waves in a 10 mm thick steel plate.*

Lamb waves are dispersive, i.e. different frequency components propagate at different speeds (group velocity varies with frequency). This results in the pulse propagating over a distance. To simulate dispersion, the following steps were performed:

–Simulation assumptions

–Center frequency: $f0 = 1MHz$: Frequency range: $0.5 - 2.5MHz$

–Dispersion: Linear drop from $2200\,m/s$ to $1800\,m/s$ across the frequency band

–Propagation distance: $d = 1.0m$

–Fourier transform of the input signal is performed

–Frequency-dependent phase shifts are applied to simulate dispersion.

–Reconstruct the signal in the time domain using inverse FFT.

The simulation result is shown in Fig. 5.

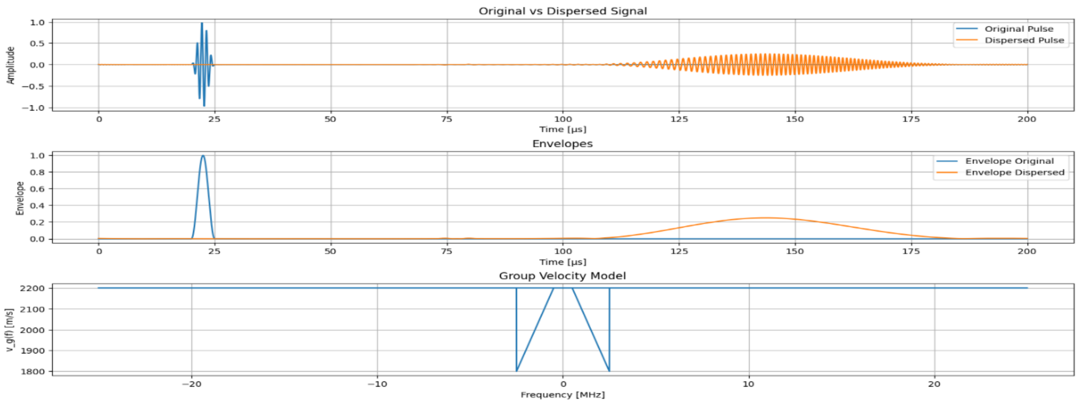

Fig. 5. Results of modeling linearly dispersive group velocity of Lamb waves in Python

Developed Python script that Models linearly dispersive group velocity; Applies dispersion via FFT → phase shift → IFFT, plots graphs of the original and dispersive signal and envelopes, visualizes the group velocity model.

CONCLUSIONS

Clamp-on ultrasonic gas flow meters offer compelling advantages in non-invasive installation and operational flexibility, making them a valuable tool in a variety of industrial sectors. However, achieving high accuracy gas flow measurement presents significant technical challenges, primarily stemming from the profound acoustic impedance mismatch between the pipe wall and the gas, resulting in strong signal attenuation and a low signal-to-noise ratio. The analysis highlights that while traditional shear wave sensors face fundamental physical limitations in gas due to high attenuation characteristics, advanced Lamb wave technology provides a transformative solution. Lamb waves ingeniously exploit the resonant properties of the pipe wall, acting as an acoustic transformer to efficiently couple ultrasonic energy to the gas. This not only significantly improves signal strength, but also provides the critical capability of non-invasive velocity profile measurement, a function previously limited to expensive and invasive inline meters. This advance fundamentally elevates clamp meters from simple spot-checking devices to precision instruments capable of performing specialized measurements.

REFERENCES

[1]. Mehrabova M.A., Mammadova S.I., Kerimov F. Sh., Safarova S.I., Gulmamedov K.J., Hamdillayeva I.H. Influence of discharges and UV irradiation on the electrical properties of high pressure polyethylene and compositions on its base. Polymer-Plastics Technology and Materials. 2024, 63,16, 2237-2245.

https://doi.org/10.1080/25740881.2024.2369677

[2]. Mehrabova M.A., Huseynov N.I., Asadullayeva S.G., Nazarov A.M., Poladova V.N., Suleymanli S.P. Photoelectrical properties of CdMnSe thin films. Advanced Physical Research. 2024, 6, 3, 203-210. https://doi.org/10.62476/apr63203

[3]. Nuriyev I.R., Mehrabova M.A., Nazarov A.M., Sadigov R.M. Growth of epitaxial $Cd_{1-x}Mn_xTe$ films. Inorganic materials. 2016,52,9, 886-889. https://doi.org/10.1134/S0020168516090132

[4]. Mekhrabov A.O., Mehrabova M.A.. Effect of gamma irradiation on optical properties of CdMnTe thin films. 2024, 1119, 3-12. https://doi.org/10.4028/p-bUt1qb

[5]. Mehrabova M.A,. Mekhrabov A.O. Effect of gamma irradiation on electrical and photoelectrical properties of Cd1-xMnxTe thin films. Machine Science. 2023, 2, 70-77. http://dx.doi.org/10.61413/GDKV8772

[6]. Techniques, Importance, and Challenges of Natural Gas Flow Measurement https://sino-inst.com/ (Accessed: May 22, 2025)

[7]. US20200056917A1 - Leaky Lamb Wave Flowmeter - Google Patents, https://patents.google.com/patent/US20200056917A1/en (Accessed: May 20, 2025)

[8]. All About Ultrasonic Flow Meters - KOBOLD USA, https://koboldusa.com/articles/type-of-flow-meters/all-about-ultrasonic-flow-meters/ (Accessed: May 15, 2025)

[9]. Clamp-on flow meters and Alicat portable flow meters - Alicat Scientific, https://www.alicat.com/support/choosing-an-instrument-clamp-on-flow-meters/ (Accessed: May 25, 2025)

[10]. The Two Types of Ultrasonic Flow Meters - Coltraco, https://coltraco.com/what-are-the-two-types-of-ultrasonic-flow-meters/ (Accessed: April 15, 2025)

[11]. The Two Types of Ultrasonic Flow Meters - Coltraco, https://coltraco.com/what-are-the-two-types-of-ultrasonic-flow-meters/ (Accessed: April 15, 2025)

[12]. Operating Instructions Ultrasonic Flowmeter - Arkon Flow Systems is , https://www.arkon.co.uk/dokumenty/arkon-uscx150-user-guide.pdf (Accessed: April 18, 2025)

[13]. Masasi B., Frazier R., Taghvaeian S. Review and Operational Guidelines for Portable Ultrasonic Flowmeters. Oklahoma Cooperative Extension Service 2017, Id: BAE-1535 p.1-8 https://www.researchgate.net/publication/318472016 (Accessed: April 28, 2025)

[14]. James D. A Perfect Match: Optimizing clamp-on flow measurement with Lamb-wave sensors, Siemens Process Instrumentation BY SIEMENS AG October 29, 2018 https://www.pcne.eu/article/a-perfect-match-optimizing-clamp-on-flow-measurement-with-lamb-wave-sensors (Accessed: April 18, 2025)

[15]. Ultrasonic Water Flow Meter Design and Testing — MSP430 Academy, Texas Instruments 2024. https://dev.ti.com/tirex/explore/node?node=A__AUxLkAvzLrljvLBB0bSqSw__MSP430-ACADEMY__8HaEUeq__LATEST (Accessed: May 18, 2025)

[16]. Funck B., Baldwin P. Challenges for ultrasonic flow meters in wet gas applications FLEXIM GmbH, Berlin, Germany, https://nfogm.no/wp-content/uploads/2014/02/FLEXIM-GmbH-2012-NFOGM_01.pdf (Accessed: May 18, 2025)

[17]. Guo K. What is temperature compensation and pressure compensation Flow Meters Supplier, China,22024 https://sino-inst.com/temperature-compensation-and-pressure-compensation-flow-meters/ (Accessed: May 18, 2025)

Received: 01.02.2025
Accepted: 14.10.2025

MACHINE SCIENCE

ISSN: 2227-6912
E-ISSN: 2790-0479

2025, № 2 Pages 69-73

APPLICATION PROSPECTS OF $Bi_{1-x}(Ni_3Sn)_x$ ALLOYS IN THERMOMAGNETIC ENERGY CONVERTERS

Chingiz ABILOV[1,a*], Mehriban HASANOVA[1,b], Seyyare SADIGOVA[1,c], Elmira GASIMOVA[1,d], Nigar HUSEYNOVA[1,e]

[1]Azerbaijan Technical University, Baku, Azerbaijan

*E-mail: [*a]chingiz.ebilov@aztu.edu.az, [b]mehriban.hesenova@aztu.edu.az, [c]seyyare.sadiqova@aztu.edu.az, [d]elmira.qasimova@aztu.edu.az, [e]nigar.huseynova@aztu.edu.az*

https://doi.org/10.61413/YFTS8016

Abstract: The temperature dependence of the transverse and longitudinal Nernst-Ettingshausen coefficients was studied in the $Bi_{0,995}\left(Ni_3Sn\right)_{0.005}$ eutectic alloy. It has been shown that the transverse Nernst-Ettingshausen coefficient, which is a dimensionless quantity, has a negative sign throughout the entire measured temperature range, and the invariance of this sign with increasing temperature is due to the stability of the charge carriers. It has been established that the magneto-thermoelectric coefficient does not exhibit a strong temperature dependence, which is also considered promising for creating an infrared detector based on the synthesized eutectic composition. Using this alloy, the active part of a thermal radiation receiver/detector was designed, and its parameters, such as voltage responsivity and the thermomagnetic quality factor, were calculated.

Keywords: *eutectic alloy, Nernst-Ettingshausen coefficients, thermomagnetic energy converter*

INTRODUCTION

Thermomagnetic and thermoelectric materials are widely used in modern converter technology $[1-4]$. These types of materials ideally possess a complex band structure so that intrinsic conductivity decreases when the charge carrier concentration is high enough. Such a situation often leads to enhanced performance in materials with a narrow band gap. This class of materials includes bismuth and its alloys. Bismuth belongs to the group of semimetals characterized by equal concentrations of electrons and holes and high electrical conductivity, leading to prominently observed thermomagnetic effects. These and other unique properties of bismuth are also observed in bismuth-rich solid solutions and eutectic alloys.

It was first shown in $[5]$ that bismuth single crystals can be used to create thermoelectric and thermomagnetic energy converters operating in the infrared range. The high mobility of charge carriers in this material makes its thermomagnetic properties particularly interesting. Bismuth is also promising for the development of infrared detectors. According to studies of its electrophysical properties, bismuth would be considered an excellent material for devices designed to measure heat flow if its valence and conduction bands did not overlap, as band overlap increases the concentration of intrinsic charge carriers, leading to weaker thermomagnetic properties. Such shortcomings can be partially mitigated by forming bismuth-based solid solution compositions. For example, adding small percentages of antimony to bismuth in the $Bi-Sb$ system partially reduces band overlap, decreases the intrinsic charge carrier concentration, increases electrical conductivity, and decreases lattice thermal conductivity. Despite these changes, the performance metrics of thermomagnetic converters made from this solid solution were not sufficiently high.

Since the other component of the object under study, the compound Ni_3Sn, possesses high mechanical strength and microhardness, its alloys can be used to produce solid-state lubricants and rolling bearings in mechanical engineering. The incorporation of such nickel compounds into metallic bismuth not only improves its mechanical properties but also increases its heat resistance.

The study of $Bi-Ag$ system eutectics aimed at increasing thermomagnetic efficiency is also of interest $[5]$. In this bismuth-rich eutectic, the metallic silver phase has a needle-like arrangement. Studies have shown that a longitudinal electric field applied along the silver needles strongly increases the Nernst-Ettingshausen $(N-E)$ field. However, it was found that the value of the $N-E$ coefficient in this case is not very large and is no higher than that of pure bismuth. This is likely because prior to eutectic formation, silver atoms dissolve in the bismuth matrix, creating impurity levels and increasing the charge carrier concentration above the intrinsic level. This high concentration of charge carriers does not produce the desired enhancement of the $N-E$ effect. Better performance is expected when the second phase in the eutectic composition does not behave as a dopant.

This paper presents the results of the study of a promising bismuth-based composition for thermomagnetic energy converters. Studies of the Ni_3Sn-Bi system established that a bismuth-based eutectic forms at the composition $Bi_{0,995}(Ni_3Sn)_{0.005}$. This eutectic is in a degenerate state and melts at $\sim 543K$. The relatively low melting temperature of the eutectic allowed for crystallization of a needle-like eutectic structure using zone melting. To evaluate the potential of this material for IR radiation receivers operating via the thermomagnetic effect, the temperature dependence of the Nernst-Ettingshausen coefficients were determined. The sensitivity and thermomagnetic quality factor of potential thermomagnetic receiver based on this material were calculated. The calculations took into account the effect of magnetic field strength on the values of electrical conductivity, thermal conductivity, heat capacity, and the $N-E$ coefficient.

MATERIALS AND METHODS

Thermomagnetic properties were measured on polycrystalline samples obtained using single-temperature synthesis technology. The samples were prepared using bismuth (Bi) and tin (Sn) of $B4$ purity, as well as carbonyl nickel (Ni) of $TU-6-09$ grade, in a furnace with a vibratory mixer at temperatures ranging from 573 to $1223°C$, depending on the composition. The purpose of increasing the synthesis temperature to $\sim 1223°C$ was to achieve complete melting of nickel.

To ensure equilibration in the alloys, the samples were subjected to heat treatment (annealing) at a temperature of $\sim 253°C$ for ~ 480 hours. The resulting polycrystalline alloys had a dense structure and were dark gray in color with a metallic luster.

After characterizing the physicochemical properties of the eutectic material, parallelepiped-shaped samples were prepared, and their thermomagnetic properties were measured.

To prepare the active part of the thermomagnetic converter, a $K-208$ glass substrate coated with a thin conductive layer of SnO_2 was used. A thin layer of $Bi_{0,995}(Ni_3Sn)_{0.005}$ was deposited onto the oxide layer using magnetron sputtering. The substrate temperature was maintained at $\sim 180°C$. Pure nickel was subsequently deposited to serve as ohmic contacts. Appropriate masks were used to pattern both the active eutectic layer and the ohmic contacts. The resulting structure was placed in a non-ferrous metal case.

RESULTS AND DISCUSSION

It is known that in addition to galvanomagnetic properties, thermomagnetic effects in materials are also of great importance for scientific and applied purposes $[6,7]$. These effects are primarily related to the fundamental properties of the materials. Since the potential applications of thermomagnetic effects can be determined from the temperature dependencies of these effect parameters, we investigated the temperature dependence of the transverse and longitudinal Nernst-Ettingshausen coefficients in the synthesized $Bi_{0,995}(Ni_3Sn)_{0.005}$ eutectic alloy.

When a heat flow passes along the $x-axis$ and a magnetic field is applied along the $z-axis$, an electric field is generated along the $y-axis$, given by:

$$E_y = -QH\frac{dT}{dx},$$

where, Q is the transverse Nernst-Ettingshausen coefficient, H is the magnetic field strength, and dT/dx is the temperature gradient.

Fig. 1 shows the temperature dependence of the dimensionless transverse Nernst-Ettingshausen coefficient ε_y of the $Bi_{0,995}(Ni_3Sn)_{0.005}$ alloy:

$$\varepsilon_y = E_y \Big/ \frac{k}{e}\frac{dT'}{dx}$$

where k is the Boltzmann constant, and e is the elementary charge. As can be seen, ε_y tends to decrease monotonically from liquid nitrogen temperature up to $: \; 600K$. ε_y has a negative sign that does not change as temperature increases. The constant sign may indicate the dominance of a single type of charge carrier or scattering mechanism over this temperature range [8].

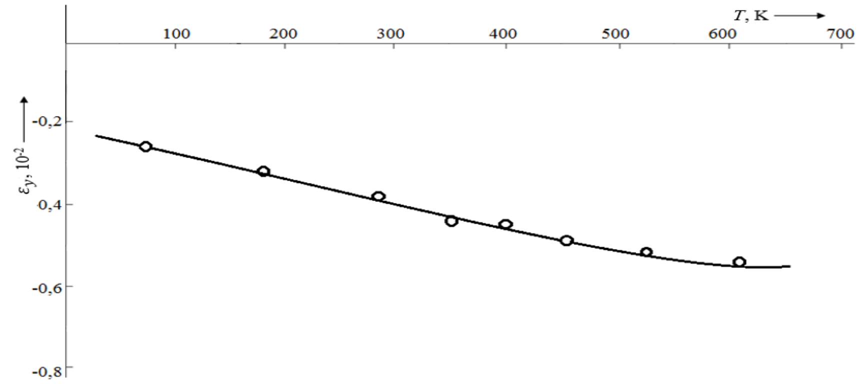

Fig.1. Temperature dependence of the dimensionless transverse Nernst-Ettingshausen coefficient ε_y of the $Bi_{0,995}(Ni_3Sn)_{0.005}$ eutectic alloy

The longitudinal Nernst-Ettingshausen effect, also known as the magnetothermo-emf, describes how the thermopower (Seebeck coefficient, α) of a material changes when a magnetic field is applied, i.e., $\Delta\alpha = \alpha(H) - \alpha(0)$. The temperature dependence of the longitudinal Nernst-Ettingshausen coefficient is shown in Fig. 2. As can be seen, the value of this coefficient begins to increase with increasing temperature and tends to remain relatively constant above $: \; 523K$.

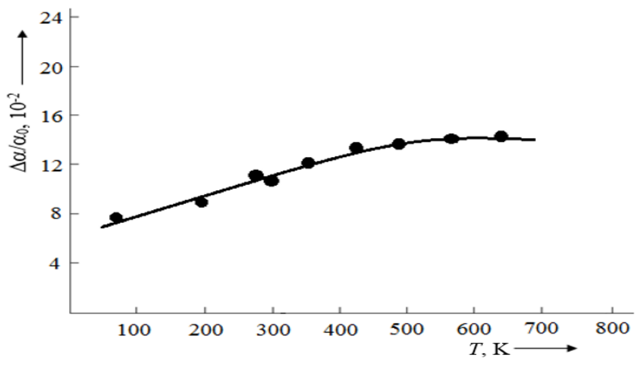

Fig. 2. Temperature dependence of the longitudinal Nernst-Ettingshausen coefficient of the $Bi_{0,995}(Ni_3Sn)_{0.005}$ eutectic alloy

The relatively weak temperature dependence of the magnetothermo-emf is considered a positive indicator of the suitability of this eutectic composition for use in infrared receivers [9].

Using these results, along with measurements of other thermophysical and galvanomagnetic properties of the $Bi_{0,995}(Ni_3Sn)_{0.005}$ alloy, an infrared receiver/detector based on the Nernst-Ettingshausen effect was designed (Fig. 3).

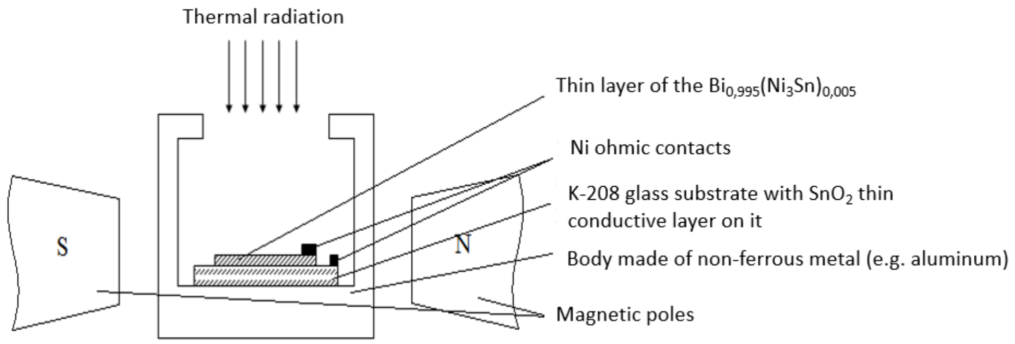

Fig.3. Schematic of the thermal radiation receiver/detector with a $Bi_{0,995}(Ni_3Sn)_{0.005}$ *active layer*

The main parameters of the developed thermal radiation receiver/detector were calculated as follows:

1. The specific sensitivity (voltage responsivity) δ was calculated using the formula:

$$\delta = \frac{E_y}{W/S} = \frac{QH}{æ},$$

where W/S is the absorbed irradiance, and æ is the thermal conductivity of the sample (æ=3.2 $W/(m\cdot K)$ at zero field). This value is known to decrease in a magnetic field, primarily due to the suppression of phonon thermal conductivity. This reduction in thermal conductivity is advantageous for increasing the efficiency of thermomagnetic converters. From the calculations, it was found that at a temperature of $300K$, δ has a value of $2.5\cdot 10^{-5} V\cdot m/W$.

2. The thermomagnetic quality factor F of the receiver was estimated using the expression:

$$F = \frac{QB}{æ^{3/4}\cdot C_P^{1/4}\cdot \rho^{1/2}}.$$

Here B is magnetic field, C_p is the specific heat capacity and ρ is the electrical resistivity. According to the calculations, a parameter $F = 3\cdot 10^{-4} W^{-1/2}\cdot m\cdot s^{1/2}$.

3. The distance between the thin layer of the eutectic alloy $Bi_{0,995}(Ni_3Sn)_{0.005}$ (the active working material) and the SnO_2 contact material was calculated as:

$$d_{cont} = \sqrt{\frac{\varepsilon k'T}{2\pi e^2 n_{cont}}} = 2,5\cdot 10^{-7}\, cm.$$

ε is the absolute permittivity of the alloy.

When calculating this value, the concentration of charge carriers (electrons) near the contact, the density of states (N_c), and the height of the potential barrier (φ) between the contact layer and the active working layer were taken into account. These values are exponentially related as follows:

$$n_{cont} = N_c \exp\left(-\frac{\chi-\varphi}{kT}\right),$$

there χ is electron affinity.

4. Effective transparency coefficient in the contact gap (D_{cont}) for a surface recombination velocity $V_0 = 2\cdot 10^3\, cm/\sec$ was:

$$D_{cont} = \exp-\left[\left(\frac{32m^*V_0}{h}\right)\right]\cdot \pi d_{cont} = (4\div 6)\cdot 10^{-4}.$$

5. The concentration of recombination centers (N_{rec}) was calculated as:

$$N_{rec} = \frac{2D_{cont}}{d_{cont}S_m} = 10^{12}\,cm^{-3},$$

where S_m is the capture cross-section of centers exhibiting Coulomb capture.

CONCLUSION

Considering the prospects of using bismuth and some solid solutions based on it in thermomagnetic converters, the thermomagnetic effects and the temperature dependence of the transverse and longitudinal Nernst-Ettingshausen coefficients in the synthesized eutectic alloy $Bi_{0,995}(Ni_3Sn)_{0.005}$ were investigated. Using this eutectic alloy, an active layer for a thermomagnetic energy converter was developed, and key performance parameters were calculated. The obtained results suggest that the eutectic alloy $Bi_{0,995}(Ni_3Sn)_{0.005}$ is a promising material for developing thermomagnetic energy converters based on the Nernst-Ettingshausen effect.

REFERENCES

[1]. Singh, R., Dogra, S., Dixit, S., Vatin, N., Bhardwaj, R., Sundramoorthy, A. K., Perera, H.C.S., Patole, Sh. P., Mishra, R. K., Arya, S. (2024). *Advancements in thermoelectric materials for efficient waste heat recovery and renewable energy generation*. Hybrid Adv. 5, 100176. https://doi.org/10.1016/j.hybadv.2024.100176

[2]. Zulkepli N., Yunas J., Mohamed M. A., Hamzah A. A. (2021). *Review of Thermoelectric Generators at Low Operating Temperatures: Working Principles and Materials*, Micromachines 12(7), 734. https://doi.org/10.3390/mi12070734

[3]. Hendricks, T., Caillat, T., Mori, T. (2022) *Keynote Review of Latest Advances in Thermoelectric Generation Materials, Devices, and Technologies,* Energies 15(19), 7307. https://doi.org/10.3390/en15197307

[4]. Zoui, M. A., Bentouba, S., Stocholm, J. G., Bourouis, M. (2020). *A review on thermoelectric generators: progress and application*, Energies 13(14), 3606.

[5]. Washwell, E., Hawkins, S., Cuff, K. (1970). *The Nernst detector: fast thermal radiation detection.* Appl. Phys. Lett., 4(17), 164-169. https://doi.org/10.1063/1.1653349

[6]. Aliyev, S. A., Zulfigarov, E. I. (2009). *Thermomagnetic and thermoelectric phenomena in science and technology*, Elm, Baku.

[7]. Iordanishvili, E., Babin, V. (1983). *Non-stationary processes in thermoelectric and thermomagnetic energy conversion systems.* Nauka, Moscow.

[8]. Abilov, Ch., Guliyev, A., Gasanova, M., Gasimova, E. (2017). *The features of thermomagnetic properties of solid solution $Cu_{1-x}In_xCr_2S_4$.* Int. J. of Sci. Eng. and Appl. Science (IJSEAS) 3(11), 54-57.

[9]. Katrich, A., Kuz'michev, V. (1978). *Radiation detectors based on the Nernst–Ettingshausen effect.* Sov. J. of Quantum Electron., 8(9), 1102-1105. https://doi.org/10.1070/QE1978v008n09ABEH010733

Received: 17.03.2025
Accepted: 19.11.2025

MACHINE SCIENCE

ISSN: 2227-6912
E-ISSN: 2790-0479

2025, № 2 Pages 74-87

SUSTAINABLE SELF-COMPACTING CONCRETE WITH PVC WASTE AS AN ALTERNATIVE TO NATURAL SAND

Talha WAHEED[1,a*], Atif MEHMOOD KHAN[1,b], Muhammad USMAN[1,c], Muhammad SOHAIL[1,d], Qasim BILAL[1,e]

[1]National University of Sciences and Technology, Islamabad, Pakistan

E-mail: [*a]twaheed.bece22nice@student.nust.edu.pk, [b]amehmood.nice@nust.edu.pk, [c]ausman.bece22nice@student.nust.edu.pk, [d]msohail.bece22nice@student.nust.edu.pk, [e]mqasim.bece22nice@student.nust.edu.pk

https://doi.org/10.61413/LJEP7867

Abstract: The placement of fresh concrete in congested rebar leads to honeycombing, thus compromising the quality of concrete. SCC resolves this issue by introducing a higher ratio of fines. Since plastic requires hundreds of years to degrade and contributes to long-term environmental pollution, its reuse in concrete provides a sustainable solution. This study investigates the use of Polyvinyl Chloride (PVC) scrap as a partial replacement of fines aggregate in the development of ecofriendly SCC. The primary objective of this research is to develop an eco-friendly mix that replaces fines while maintaining desirable workability and mechanical strength. For this purpose, various trial mixes were made and tested to achieve the desired workability without compromising strength. Fresh properties of the concrete mix were evaluated by tests, including the V-Funnel test, L-Box test, and slump flow test, to ensure that the concrete mix has the required flowability. Optimum results were achieved with 10-20% replacement of fine aggregates with PVC scrap, with 28-day strength more than 3000 psi (20.68 MPa) and passing ability greater than 80% along with acceptable value of v funnel test, showing that the mix has desired mechanical and flow properties thus 10–20% PVC replacement SCC is suitable for precast non-structural elements opens pathways for energy-efficient precast panels. Research concludes that the addition of PVC scrap is an eco-friendly alternative to develop green concrete. The reuse of PVC (a plastic material) in concrete not only reduces environmental pollution but also proves to be an innovative material in the construction industry, contributing to plastic waste management and green construction practices.

Keywords: *Self-compacting concrete, Polyvinyl Chloride (PVC), Eco-friendly concrete, green construction, Plastic waste management.*

INTRODUCTION

The construction industry has wide applications from small to large infrastructure projects of Concrete as a building material due to its strength, versatility, and low cost. (Ètcin, n.d.) Traditional Concrete mix comprises cement, sand, aggregates, admixtures, and water(Babor et al., n.d.) . However, the large-scale production of these constituents has considerable environmental consequences. Cement alone is highly carbon-intensive: concrete contributes 0.05–0.13 tons of CO_2, contributing to 5% of total CO_2 emissions worldwide (Obla, 2009). Sand is the world's second most consumed natural resource after water. 50 billion tons of sand are used on a yearly basis. China used more sand than the United States did throughout the entire 20th century. Countries like the UAE, that are desert-rich, export sand for construction(*Why the World Is Running out of Sand*, n.d.). Such over-extraction of natural materials damages the ecosystem, highlighting the need to explore sustainable alternatives for concrete production.

To address these environmental challenges, the concept of green concrete has emerged, focusing on reducing carbon (Obla, 2009) . Supplementary cementitious materials (SCMs) have been used such as Fly ash(FA), Silica fume(SF), Ground granulated blast furnace slag (GGBS), Rice husk ash(RHA), Waste glass powder(WGP), and red mud(RM) to replace cement. Self-compacting concrete (SCC) has been developed to improve workability, eliminating the need for vibration(Shi et al., 2015) . Researchers have also investigated various SCMs as substitutes for fine and coarse aggregates, including quarry dust, foundry sand, glass powder, marble dust, ceramic waste and steel slag,(Sun et al., 2020). Cement kiln dust (CKD), foundry sand, ladle furnace slag (LFS), Microcellulose Fibers (from recycled paperboard), nylon sisal fibers, waste foundry sand, coal bottom ash, waste tire rubber, copper slag and waste glass have also been incorporated (Kannan et al., 2015) (Gupta et al., 2021) (Devi & Vivek, 2024).

In recent years, plastic has been used as a potential concrete material (Hamzeh, n.d.; Manjunatha et al., 2023; Naidu Gopu et al., 2022).Plastics have been extensively used in different industries since World War II and have earned the name of “material with 100 uses”. Its global plastic production exceeded 359 million tons per year, but plastic is a non-biodegradable material and degrades slowly, taking up to 100-1000 years(Nayanathara Thathsarani Pilapitiya & Ratnayake, 2024). Among plastics, PVC is the third most widely produced, accounting for around 10% of global plastic production (Campisi et al., 2025) and is extensively used in the construction industry, especially in PVC pipes, windows, and flooring(Miliute-Plepiene et al., 2021). PVC used in pipes is highly resistant naturally due to its strong covalent bonding and high molecular weight, but these pipes, once used, are left free on landfills, releasing gases that cause serious ecological concerns(Nayanathara Thathsarani Pilapitiya & Ratnayake, 2024). PVC can be recycled mechanically, chemically, by incineration, and landfilling but each recycling process involves adverse effects (Kudzin et al., 2024) (Campisi et al., 2025)(Lu et al., 2023). This makes reuse of PVC in construction particularly attractive. Several studies have explored the incorporation of PVC as a partial replacement for sand in concrete(Miliute-Plepiene et al., 2021)(Kudzin et al., 2024) , but many studies lack proper evaluation of mechanical and flow properties, and combined environmental benefits of simultaneously reducing sand depletion and reusing PVC waste remain underexplored.

Given the dual challenges of unsuitable sand consumption and plastic waste management, this study aims to systematically asses the feasibility of effect of PVC waste as a partial replacement for sand in SCC, especially mechanical and flow properties of modified mixes. Thermal conductivity tests are conducted to assess the thermal performance highlighting its potential as an insulating material in sustainable construction application

Polyvinyl chloride (PVC) is widely used in Pakistan’s construction sector, particularly in the manufacturing of water supply, sewerage, and drainage pipes due to its durabil-ity, corrosion resistance, and cost-effectiveness. During PVC pipe manufacturing, a significant amount of waste is generated in the form of off-cuts, defective pipes, trimming residues, and rejected products. This waste is typically classified as post-industrial PVC waste.

In Pakistan, PVC pipe manufacturing is largely concentrated in small- to medium-scale industrial units, where waste management practices are often limited. A consid-erable portion of PVC waste is either stockpiled, sold at low value, or disposed of through landfilling, leading to environmental concerns and inefficient resource utiliza-tion. Although mechanical recycling of PVC waste is technically feasible, its reuse in high-value engineering applications remains limited.

The PVC waste considered in this study represents mechanically processable PVC waste typically generated during pipe manufacturing operations in the Pakistani con-struction industry.

Such waste possesses stable chemical composition and predictable physical properties, making it a suitable candidate for evaluation as a partial re-placement of natural fine aggregates in concrete.

This study addresses the engineering feasibility of valorizing PVC pipe waste by incorporating it into self-compacting concrete (SCC), thereby contributing to sustaina-ble material utilization and reduction of construction-related environmental impacts.

MATERIALS AND METHODS

For this study, we carefully selected materials that met the necessary ASTM standards and performance expectations. We used Ordinary Portland Cement (OPC), which is in line with ASTM C150 specifications. This cement was made up of 95% clinker and 5% gypsum, providing the strength and setting properties needed for SCC. With a specific gravity of 3.16, it took 160 minutes for initial setting and 180 minutes to fully set. After 7 days, the compressive strength reached 16.28 MPa, ensuring the material met the required performance standards.

Fine aggregates used were natural sand with a maximum size of 4.75 mm. The sand was air-dried prior to use and exhibited a specific gravity of 2.6, a fineness modulus of 1.95, and an absorption capacity of 2 percent, all within the limits specified by ASTM C33. Coarse aggregates comprised crushed stone with a nominal size of 25 mm, retained on a 3/8-inch sieve and passing through a 1/2-inch sieve. These aggregates had an absorption capacity of 1 percent and an aggregate crushing value of 22.66 percent, also conforming to ASTM C33 requirements. A summary of the main properties is presented in the Table 1

Table 1. Physical and Mechanical Properties of Fine and Coarse Aggregates

Property	Fine Aggregates	Coarse Aggregates
Specific Gravity	2.6	-
Fineness Modulus	1.95	-
Absorption Capacity (%)	2	1
Nominal Size	4.75 mm max	25 mm
Aggregate Crushing Value	-	22.66%

Tap water was used for both mixing and curing of concrete. The curing process was standardized using a water bath maintained at 15°C in line with ASTM C192 recommendations.

To enhance the workability and self-compacting behavior of the concrete mix, a high-range water-reducing admixture (HRWRA), SP-435 Super-plasticizer, was incorporated at a dosage of 1.75% by weight of cement. This admixture fulfilled ASTM C494 Type F specifications. Though specific physical parameters were not tabulated in this version, it demonstrated standard density and pH values suitable for SCC applications.

Polyvinyl chloride (PVC) waste in the form of scrap grounded pipes was introduced as a partial replacement for sand. The PVC particles, irregular in shape and passing through a 2 mm sieve, exhibited zero water absorption due to their hydrophobic nature. This influenced the mix design and fresh concrete properties, notably reducing workability and altering capillary action within the concrete matrix.

PVC Material Specifications

The PVC material used in this study was rigid polyvinyl chloride (R-PVC), commonly sourced from post-consumer construction waste, such as discarded pipes and profiles. No flexible PVC (F-PVC) products were included, as rigid PVC is preferred for concrete applications due to its dimensional stability and limited deformation under stress. Where available, the PVC conformed to industrial standards for construction-grade PVC (e.g., ISO 1452-1 for PVC pipes), ensuring consistency in material properties.

Before processing, the PVC had a bulk density of approximately 1.35–1.45 g/cm³, which is slightly lower than that of natural sand, contributing to its lightweight nature. The particle size of the PVC waste was initially irregular and ranged from a few millimeters to several centimeters. No additional additives were present beyond the original formulation, which may include typical stabilizers, plasticizers, or fillers inherent to rigid PVC. These additives influence thermal stability, brittleness, and mechanical strength, and were accounted for in the grinding process to ensure consistent particle behavior in the concrete mix.

The physical and chemical properties of PVC have direct implications for concrete performance. Its hydrophobic nature affects water absorption, potentially influencing the water-to cement ratio and workability. The particle shape and density contribute to the packing density, which is critical in self-compacting concrete (SCC) for maintaining flowability and preventing segregation. Additionally, uniform particle size and clean surfaces improve interfacial bonding with the cement matrix, ensuring acceptable mechanical performance in hardened SCC.

Fig. 1. Industrial PVC Scrap Collected for Laboratory Processing

PVC Waste Generation in Industrial and Construction Processes

PVC waste in industrial and construction settings primarily originates from pipe cutting, trimming, and the production of defective or off-specification products. During manufacturing and installation, surplus PVC materials such as pipe stubs, profile offcuts, and rejected items are generated and often discarded. In literature, studies estimate that construction and manufacturing activities can produce up to 5–15% of total PVC production as waste, depending on the scale of operations and quality control measures For example, a medium-sized PVC pipe manufacturing facility may generate several hundred kilograms of scrap PVC per day, while large-scale operations can produce several tons monthly.

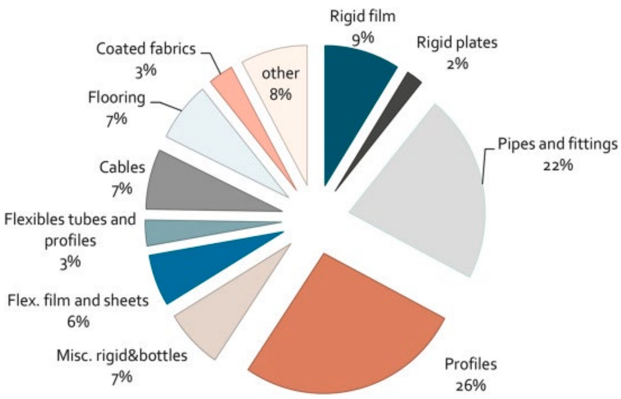

Fig. 2. Typical Sources of PVC Waste for Concrete Experiment

Processing of PVC Waste

The processing of PVC waste was carried out to obtain particles suitable for use as a partial replacement of fine aggregates in self-compacting concrete (SCC). The PVC waste was processed to obtain particles suitable for partial replacement of fine aggregates in SCC through the following steps:

- Collection of industrial PVC scrap from cutting, trimming, and defective pipes.
- Manual sorting to remove contaminants.
- Cutting into smaller chips for uniform grinding.
- Mechanical grinding to reduce particle size to 0.5–2 mm.
- Sieve analysis to retain particles passing through a 2 mm sieve.
- Air-drying and storage for later use in concrete mixes.

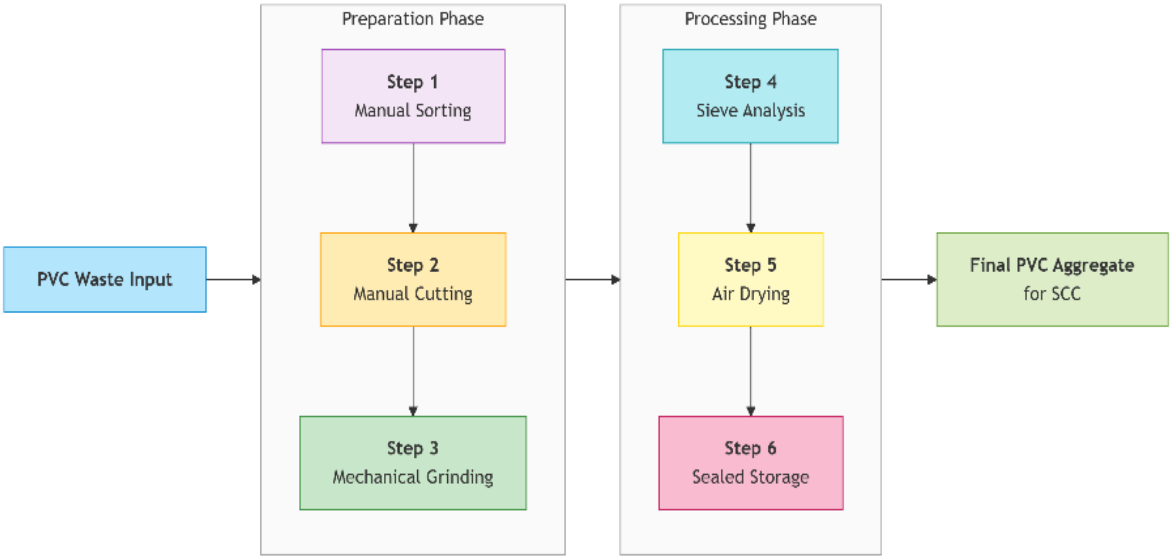

Fig. 3. Schematic Workflow of PVC Waste Processing for Self-Compacting Concrete

Initially, PVC scrap was collected, representing rigid industrial pipe waste typically generated during pipe cutting, trimming, and rejection of defective products. The collected material was first sorted manually to remove any non-PVC contaminants, including metal fittings, adhesives, or rubber residues. Only clean PVC segments were selected to ensure uniformity and prevent contamination in the concrete matrix. Proper sorting is critical as the presence of foreign materials can compromise the performance of the concrete mix

After sorting, the PVC segments underwent manual size reduction. Large PVC pieces, typically measuring 5–10 cm, were cut into smaller chips using scissors and utility knives. This step facilitated subsequent mechanical grinding by reducing the size of the material to a manageable scale. Manual cutting also ensured that the material could be uniformly fed into the grinder for consistent particle size reduction.

The mechanical grinding of the PVC chips was then performed using a laboratory-scale grinder. The chips were ground in multiple passes to produce granular particles with irregular shapes, similar to natural sand. The grinding process reduced particle sizes to a range of approximately 0.5–2 mm. This size range was chosen to match the fine aggregates used in SCC, ensuring proper packing and flow characteristics. Though laboratory-scale equipment was used, this method reflects common industrial practices where rotary cutters, hammer mills, or blade-type grinders are employed to reduce PVC waste to the desired particle size.

Fig. 4. Laboratory-Scale Mechanical Grinder Used for PVC Size Reduction

Following grinding, sieve analysis was performed to control the particle size distribution. Standard laboratory sieves, including a 2 mm sieve, were used to separate oversized particles from the desired fraction. Only particles passing through the 2 mm sieve were retained for use in concrete mixes. This step is crucial because particle size affects the flowability, segregation resistance, and packing density of SCC. Uniform particle size distribution ensures that the PVC waste can integrate seamlessly with natural sand in the concrete matrix.

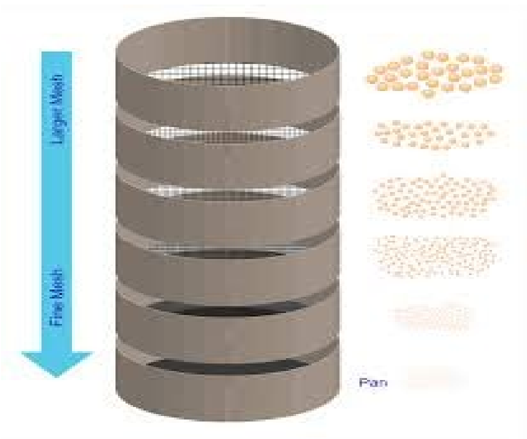

Fig. 5. Stacked Laboratory Sieves Used for Particle Size Analysis of Ground PVC

Once the appropriate particle size was obtained, the PVC particles were air-dried to remove any surface moisture. Drying prevents variations in the water-to-cement ratio during mixing and ensures consistency in the fresh concrete properties. The dried particles were then stored in sealed containers to avoid contamination and moisture absorption. In industrial practice, PVC powders are typically stored in silos or hopper bins with controlled environmental conditions to maintain particle quality.

Fig. 6. Pulverized PVC Waste for Self-Compacting Concrete Applications

The overall workflow of PVC processing can be summarized in six sequential steps: collection of PVC scrap, sorting to remove contaminants, manual cutting into smaller chips, mechanical grinding to reduce particle size, sieve analysis to select particles passing through 2 mm, and drying and storage for later use. This laboratory-based procedure provides a scalable and reproducible method that mirrors industrial processing techniques while producing PVC particles suitable for incorporation in SCC. The hydrophobic nature and irregular shape of PVC, combined with controlled particle size, ensure compatibility with concrete, while simultaneously promoting sustainability by reusing industrial waste.

To ensure technical reproducibility, the mechanical grinding was performed at a rotational speed of approximately 1500 RPM, with multiple passes until the majority of PVC particles fell within the 0.5–2 mm size range. Sieve analysis was conducted using a 2 mm mesh, and oversized particles were reprocessed to maintain uniformity. This particle size range was specifically selected to match the fine aggregate fraction used in self-compacting concrete, promoting optimal packing density, improved flowability, and reduced segregation. Uniform and appropriately sized PVC particles facilitate consistent interfacial bonding with the cement matrix, ensuring both fresh and hardened concrete properties are not compromised, while maintaining the lightweight and sustainable characteristics of the modified SCC mix.

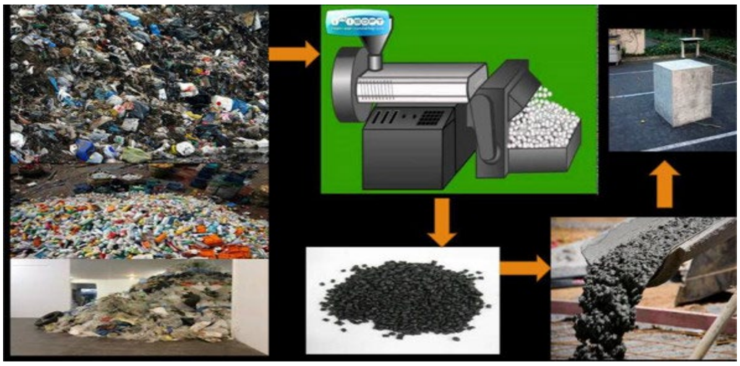

Fig. 7. PVC Processing Methodology for Self-Compacting Concrete (SCC)

METHODOLOGY

The experimental program focused on determining the fresh and hardened properties of a concrete mix in which sand was partially replaced with PVC. The mix design was such that the concrete had to be self-compacting and have desirable workability. Sand was replaced with PVC in percentages of 0%,10%,20%,30%, and 40%. ASTM and EFNARC standards were followed to conduct tests, including slump flow, V-funnel, and L-box, to assess the fresh properties of the concrete mix. Harden properties, including compressive strength and thermal conductivity, were also measured.

Several mix trials were made to develop SCC having the desired workability and strength. The first four trials were used to make a control mix without PVC, by adjusting cement, aggregates, w/c ratio, and amount of plasticizer. Several trials were made to achieve the desirable flow. The best mix design comes out to be 1:1.5:1.25, based on [18] which achieved good workability (V-funnel time: 3 s, L-box ratio: 0.85) and a compressive strength of 3015.34 psi (20.79) MPa at 7 days

Cylindrical (100 mm × 200 mm) and prism (100 × 100 × 500 mm) molds were used for casting. Given the self-leveling nature of SCC, no external vibration was applied. The concrete was cast under controlled laboratory conditions at 23 ± 2°C and relative humidity of 50–60% to prevent rapid moisture loss.

Fig. 8. Cylindrical and Prism Molds Used for SCC Casting

Table 2 Mix Design of Conventional Concrete (Without PVC)

Trials	Ratios (binder: fines: coarse)	Cement (kg)	Sand (kg)	Coarse (kg)	Plasticizer % of cement	W/C ratio
1	1:2.5:2.0	2.7	5.45	6.81	1.5	0.50
2	1: 2.0:2.5	2.7	5.45	6.81	1.5	0.50
3	1: 1.75:1.25	10	17.5	12.5	2	0.45
4	1:1.5:1.25	9.45	14	11.8	1.75	0.45

Natural sand was replaced with PVC by 10%,20%,30% and 40% in these trials to find the optimum mix in terms of both workability and mechanical strength.

Table 3. Mix Design of Concrete with PVC as Sand Replacement

Trial	Ratios (binder : fines : coarse)	Cement (Kg)	Sand (Kg)	Coarse (Kg)	PVC % of Sand	PVC (Kg)	W/C Ratio
1	1 : 1.5 : 1.25	10.6	14	11.8	10	1.4	0.45
2	1 : 1.5 : 1.25	10.6	12.8	11.8	20	3.2	0.45
3	1 : 1.5 : 1.25	10.6	9.8	11.6	30	4.2	0.45
4	1 : 1.5 : 1.25	10.6	9.7	11.6	40	6.4	0.45

After preparation of samples various tests were performed to assess fresh and physio-thermal properties of concrete mix

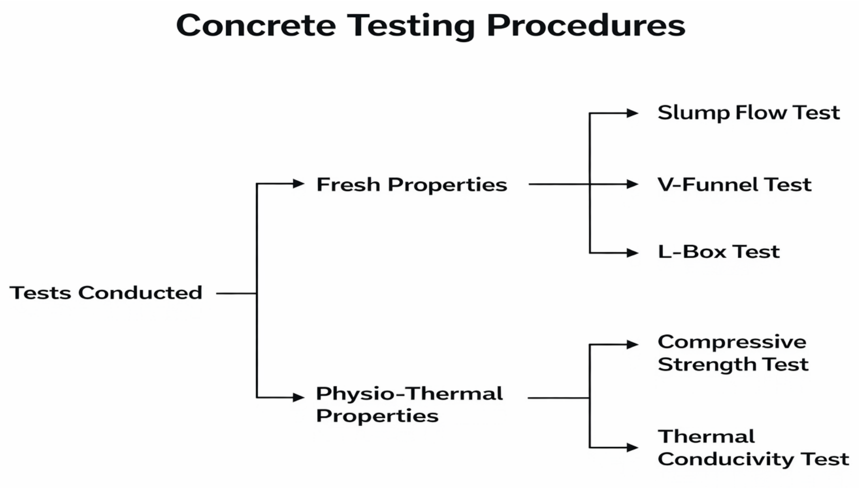

Fig. 9. Methodological framework of the present study

DETERMINATION OF FRESH PROPERTIES

Slump Flow Test:

A standard for the slump test is ASTM C1611. A conical mold of 300 mm in height, 100 mm in upper diameter, and 200 mm in lower diameter is utilized in this. Three layers of the mixture are poured, and it is tamped 25 times. After that, remove the mold and gauge how much the mix has grown in height.

V-Funnel Test:

The V-funnel test was conducted according to EFNARC guidelines. In this experiment, 12 liters of self-compacting concrete are poured into the V-funnel set on leveled and firm ground. The funnel is then filled with concrete mix. Within 10 seconds of filling, the bottom gate of the funnel should be opened, and the stopwatch should be started simultaneously. The time taken for the concrete to empty from the funnel is recorded.

L-Box Test:

The apparatus should be placed on a stable, leveled surface and vibration-free. Once the setup is confirmed, close the sliding gate. The vertical section (hopper) of the L-Box is then filled with fresh concrete, ensuring that no vibration, rodding, or tamping should be applied during filling. After filling, level the concrete top. The sliding gate is then opened, allowing the concrete to flow horizontally toward the end of the box. Once the flow ceases, the depths of concrete at two points—near the gate (h1) and at the horizontal end of the box (h2)—were measured. These measurements were used to calculate the blocking ratio, expressed as (h2/h1), which indicates the passing ability of the self-compacting concrete.

DETERMINATION OF HARDENED PROPERTIES

Compressive Strength Test:

For the compressive strength of concrete, ASTM C39 is used. It is performed on a Compression Testing Machine (CTM). Each cylinder was placed vertically and centrally between the machine's loading platens, and a uniform axial load was applied until failure occurred. The maximum load taken by the specimen is recorded, and the compressive strength is calculated by dividing this load by the cross-sectional area of the cylinder.

Thermal Conductivity Test:

The test is conducted according to ISO 22007-2:2015 and the transient plane heat source (hot disc) method was used to determine the thermal properties of the material. In this method, a flat hot disc sensor, which acts simultaneously as a heat source and a temperature recorder, was placed between two identical samples to ensure symmetrical heat flow and proper contact. A known current is passed through the probe, generating a heat pulse. The resulting temperature rise of the probe is continuously recorded with time, using, time-voltage graph thermal conductivity of the sample is analyzed

RESULTS AND DISCUSSION

This study investigated the performance of SCC when polyvinyl chloride (PVC) particles were used as a partial replacement for natural river sand. To make the mix design more eco-friendly and sustainable, PVC was deliberately introduced as a replacement material. The underlying idea was twofold: on one hand, recycling PVC waste directly contributes to sustainable construction practices, and on the other, its physical characteristics were expected to improve concrete workability. From a materials science perspective, the choice of PVC as a sand replacement was guided by its physical characteristics. PVC particles are fine, smooth, and exhibit zero water absorption, meaning they can increase the effective water content of the fresh mix and thereby improve flowability. More importantly, as highlighted by [19] by introducing PVC fines, it was expected that the rheological behavior of SCC could be enhanced, leading to superior self-compacting properties without additional chemical admixtures

After performing the tests on the control sample, it is clear that the addition of PVC influenced the fresh properties of SCC

Table 4. Workability of Conventional and PVC-Modified Concrete Mixes

Trial	Ratios (binder:fines: coarse)	PVC % of Sand	Slump(mm)	V-Funnel (sec)	L-box
1	1:2.5:2.0	0	65	-	-
2	1:2.5:2.0	0	73	-	-
4	1:1.5: 1.25	0	245	3	0.85
5	1:1.5:1.25	10	-	2.92	0.86
6	1:1.5:1.25	20	-	2.41	0.87
7	1:1.5:1.25	30	-	2.52	0.52
8	1:1.5:1.25	40	-	5.25	0.14

The data in table 4 shows that workability improved steadily up to 20% PVC replacement. This can be due to the physical nature of PVC particles. As they are smooth, non-porous, and hydrophobic, they do not absorb mixing water, which means a higher amount of free water remains available in the system. This additional free water reduces inter-particle friction and allows the mix to flow more easily.

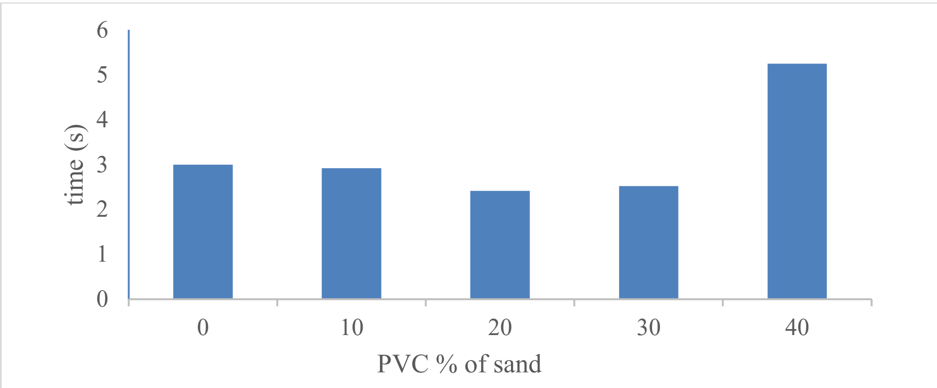

Fig. 10. Effect of PVC addition on V-funnel flow time of concrete

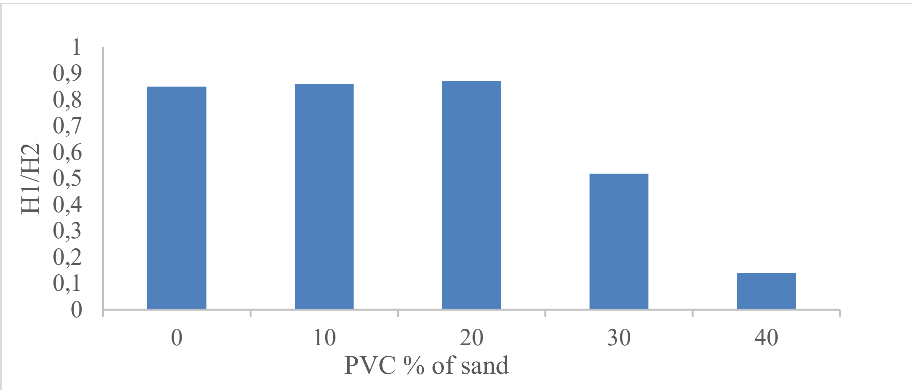

Fig. 11. Effect of PVC addition on the passing ability of concrete in the L-box test

From Figure 10 and Figure 11, it is implied that 20% PVC replacement has the maximum flowability, after which 20% workability is reduced, which is due to the edges of PVC particles.

The compressive strength decreases as the PVC increases, as shown in table 5. Across all replacement levels, the strength was lower than that of the control mix, primarily because PVC particles do not form strong interfacial bonds with the cement paste. This weak bonding limited the efficiency of stress transfer across the matrix, leading to an overall reduction of approximately 40% in compressive strength compared to the controlled SCC sample. The maximum strength recorded was 3700 psi at 30% replacement, suggesting that particle packing at this level may have produced a denser microstructure, even though the overall bonding remained poor. By contrast, mixes with 40% PVC showed a sharper strength loss as shown in Figure 11, confirming that excessive replacement compromises the compressive strength of the sample.

Table 5. Effect of PVC Addition on Compressive Strength of Concrete

Trial	Ratios (binder:fines:coarse)	PVC % of sand	7days compressive strength (psi)	28 days compressive strength (psi)
1	1 : 2.5 : 2.0	0	0	-
2	1 : 2.5 : 2.0	0	1784	-
3	1 : 1.5 : 1.25	0	3015	5025
4	1 : 1.5 : 1.25	10	1855	3092
5	1 : 1.5 : 1.25	20	1820	3033
6	1 : 1.5 : 1.25	30	2220	3700
7	1 : 1.5 : 1.25	40	2100	3500

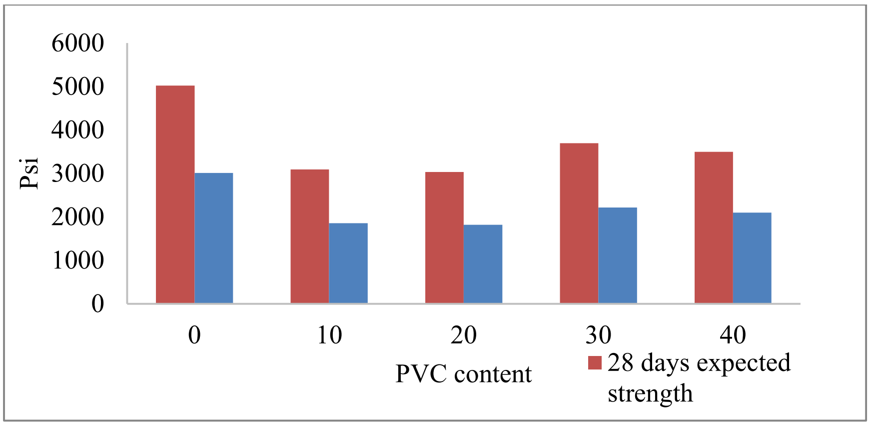

Fig. 12. Variation of compressive strength with PVC replacement levels

When these results are viewed alongside the fresh property tests, which indicated peak workability at 20% PVC, it becomes evident that the 10–20% replacement range provides the most balanced performance for SCC. Within this range, workability improvements are achieved while the strength reduction remains within tolerable limits for non-structural and moderately loaded applications.

Thermal conductivity tests were also carried out on the SCC samples containing PVC, using the transient plane heat source (hot disk) method in accordance with ISO22007-2. The results indicated that mixes with higher PVC content exhibited noticeably lower thermal conductivity compared to the control specimens. This is because PVC acts as an insulator for heat. As the proportion of PVC increased, the concrete became less effective at transferring heat, as shown in Figure 13.

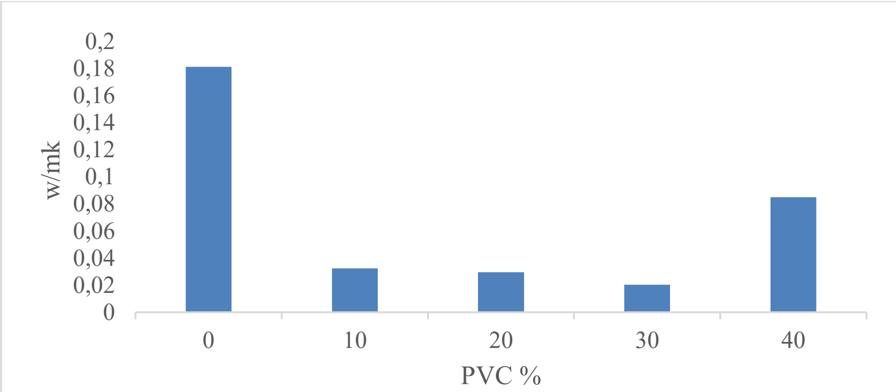

Fig. 13. Effect of PVC addition on thermal conductivity of concrete

The trend shows that minimum thermal conductivity occurs at 30% of PVC, and a sudden change in thermal conductivity at 40% can be due to voids. However, this reduction in conductivity also reflects a more heterogeneous internal structure, which, while beneficial from an energy-efficiency perspective, may not always align with structural requirements.

From the experimental results, it is clear that the optimum PVC content is between 20-30% for the fresh and hardened properties of SCC. At this range, workability is maximized while compressive strength reduction remains within acceptable limits, and thermal conductivity is significantly reduced, enhancing the material’s insulating capacity.

The optimized SCC with 20–30% PVC content is particularly suitable for precast non-structural members, such as panels, blocks, and partitions. Its improved flowability allows easy casting into complex molds without vibration, while reduced thermal conductivity enhances insulation properties. Although compressive strength is slightly lower than conventional concrete, it remains sufficient for lightweight precast applications, promoting sustainability and efficient material reuse.

Table 6. Variation of Thermal Conductivity and Diffusivity with PVC Content

Parametr	Thermal Conductivity(w/mk)	Thermal Diffusivity(w/mk)(mm2/s)
0% PVC	0.1397	0.74
	0.2231	0.88
	0.1814	0.81
Avg	**0.1814**	**0.81**
10% PVC	0.0349	0.78
	0.0298	0.76
	0.03235	0.77
Avg	**0.03235**	**0.77**
20%PVC	0.0307	0.79
	0.0202	0.73
	0.0377	0.76
Avg	**0.0295**	**0.76**
30%PVC	0.0123	0.99
	0.0286	0.95
	0.02045	0.8
Avg	**0.0205**	**0.91**
40% PVC	0.018	0.78
	0.152	0.96
	0.085	0.87
Avg	**0.085**	**0.87**

CONCLUSION

This study investigated the incorporation of Polyvinyl Chloride(PVC) as a partial replacement of natural sand to develop self-compacting concrete (SCC) to improve workability in congested rebars and address critical issues of sand scarcity and plastic waste management. Results indicate that the addition of PVC significantly influences SCC, improving flowability up to 20% addition with higher slump flow, shorter V-funnel times, and passing ratios above 80% in the L-box test, beyond which instability is indicated by segregation. Reduction of compressive strength occurs in all PVC-modified mixes, but 10-20% replacement retained acceptable strength of more than 3000 psi at 28 days. Reduction of thermal conductivity encouraged its use for insulation purposes.

Reduction of strength limits the use of the material in structural applications, but the material clearly indicates usage in precast non-structural elements. Further research should explore shrinkage, creep, advanced curing techniques, and environmental and economic assessments of material usage.

REFERENCES

[1]. P.-C. A. Ètcin, “Cements of yesterday and today Concrete of tomorrow.”
[2]. D. Babor, D. Plian, and L. Judele, “ENVIRONMENTAL IMPACT OF CONCRETE.”
[3]. K. H. Obla, “What is Green Concrete,” 2009. [Online]. Available: www.astm.org.
[4]. “Why the world is running out of sand.” Accessed: Aug. 16, 2025. [Online]. Available: https://www.bbc.com/future/article/20191108-why-the-world-is-running-out-of-sand
[5]. C. Shi, Z. Wu, K. Lv, and L. Wu, “A review on mixture design methods for self-compacting concrete,” Jun. 01, 2015, *Elsevier Ltd*. doi: 10.1016/j.conbuildmat.2015.03.079.
[6]. C. Sun, Q. Chen, J. Xiao, and W. Liu, “Utilization of waste concrete recycling materials in self-compacting concrete,” *Resour Conserv Recycl*, vol. 161, Oct. 2020, doi: 10.1016/j.resconrec.2020.104930.
[7]. P. Kannan, C. F. Jerin, and K. Murali, “A Review on Self Compacting Concrete,” 2015.
[8]. N. Gupta, R. Siddique, and R. Belarbi, “Sustainable and Greener Self-Compacting Concrete incorporating Industrial By-Products: A Review,” Feb. 15, 2021, *Elsevier Ltd*. doi: 10.1016/j.jclepro.2020.124803.
[9]. S. S. Devi and S. S. Vivek, “Self-Compacting Concrete Using Supplementary Cementitious Materials and Fibers: Review,” Dec. 01, 2024, *Springer Science and Business Media Deutschland GmbH*. doi: 10.1007/s40996-024-01414-9.
[10]. [M. Manjunatha, D. Seth, B. KVGD, S. Roy, and R. B. Tangadagi, “Utilization of industrial-based PVC waste powder in self-compacting concrete: A sustainable building material,” *J Clean Prod*, vol. 428, Nov. 2023, doi: 10.1016/j.jclepro.2023.139428.
[11]. A. Hamzeh, “Effects of Polyvinyl Chloride as a Partial Aggregate Replacement on Mechanical Properties and Behavior of Self Compacted Concrete.”
[12]. G. Naidu Gopu, R. Reddy Thummala, M. Sri Durga Vara Prasad, and S. Koti Thottempudi, “A review on mechanical properties of self compacting concrete incorporated with various types of plastic waste aggregates,” in *Materials Today: Proceedings*, Elsevier Ltd, Jan. 2022, pp. 976–982. doi: 10.1016/j.matpr.2022.05.075.
[13]. P. G. C. Nayanathara Thathsarani Pilapitiya and A. S. Ratnayake, “The world of plastic waste: A review,” Mar. 01, 2024, *Elsevier Ltd*. doi: 10.1016/j.clema.2024.100220.

[14]. L. Campisi, C. La Motta, and D. Napierska, “Polyvinyl chloride (PVC), its additives, microplastic and human health: Unresolved and emerging issues,” Jan. 15, 2025, *Elsevier B.V.* doi: 10.1016/j.scitotenv.2024.178276.

[15]. J. Miliute-Plepiene, A. Fråne, and A. M. Almasi, “Overview of polyvinyl chloride (PVC) waste management practices in the Nordic countries,” Oct. 01, 2021, *Elsevier Ltd*. doi: 10.1016/j.clet.2021.100246.

[16]. M. H. Kudzin, D. Piwowarska, N. Festinger, and J. J. Chruściel, “Risks Associated with the Presence of Polyvinyl Chloride in the Environment and Methods for Its Disposal and Utilization,” Jan. 01, 2024, *Multidisciplinary Digital Publishing Institute (MDPI)*. doi: 10.3390/ma17010173.

[17]. L. Lu, W. Li, Y. Cheng, and M. Liu, “Chemical recycling technologies for PVC waste and PVC-containing plastic waste: A review,” *Waste Management*, vol. 166, pp. 245–258, Jul. 2023, doi: 10.1016/j.wasman.2023.05.012.

[18]. B. M. Aïssoun, S. D. Hwang, and K. H. Khayat, “Influence of aggregate characteristics on workability of superworkable concrete,” *Materials and Structures/Materiaux et Constructions*, vol. 49, no. 1–2, pp. 597–609, Jan. 2016, doi: 10.1617/S11527-015-0522-9.

[19]. K. Marar and Ö. Eren, “Effect of cement content and water/cement ratio on fresh concrete properties without admixtures,” Article in International Journal of the Physical Sciences, vol. 6, no. 24, pp. 5752–5765, 2011, doi: 10.5897/IJPS11.188.

Received: 10.08.2025
Accepted: 22.12.2025

SUBMISSION GUIDELINES

General requirements.
Article should not be earlier published in any edition, stated in the short form and edited. The scientific article maintenance should correspond to one of the following scientific directions: Designing of machines; Materials technology; Mechanics; Manufacturing engineering; Economy and management; Automatics and ICT; Technical information.

The documents applied to article.
The conclusion of the corresponding organization (chair, etc.); The expert opinion on expediency of the publication of the article; The covering letter; The Information on the authors (name, patronymic, surname, the exact address, place of work and position, scientific degree, area of scientific activity, contact phones, e-mail address ,etc.).

Preparation rules.
Format - A4; *Margins from each party* - 20 mm; *Program* - Microsoft Office Word; *Font* - Times New Roman, a font size - 12, an interval – 1,15.
The scientific article can be written only in English language, and it is represented in duplicate.
Article volume - 5 … 8 pages.

Sequence of compilation:
1. Article name - on the center;
2. Names and surnames of the authors - on the center;
3. Full addresses of a place of work of authors - on the center;
4. Co-ordinates of authors: e-mail address, phone numbers.
5. The abstract: not less than two-three offers, and no more than 100 words. In the summary: article summary, problem statement, and the information on the received results should be reflected.
6. Keywords: often used 3 ÷ 5 terms under the article.
7. The basic text.
8. The references.

The main text of article should be divided as follows:
For example: "*Introduction*", "*Problem statement*", "*Decision or test methods*", "*Results of the decision or tests and their estimation*".
In introduction: the description of the problem statement, the work purpose and etc.;
In the main part: formation of problem statements; research and methods of the decision, their advantage and difference from existing methods; examples confirming efficiency of the offered method of the decision and the results received.
In the conclusion: evaluation of the results.

Drawings. *Formats* - DOC, JPEG, TIFF and PDF (600 dpi). *The size* – min. 5 × 5, max. 10 × 15. *Arrangement* - ("In the text", in the center). Images of drawings should be accurately visible, and all symbols well are read.
Drawings, paintings, schedules and algorithms should correspond to standard requirements.

Tables are located in the text and are numbered, and the name of each table should be specified in the right top corner.

Formulas should be written down in format *Equation* in the separate line. It is not recommended to use special symbols in the text written on the same line in format *Equation*. Formulas should be written down in certain sequence and are numbered on the right.

The references should correspond to the text and sequence of article. It is recommended to refer to sources published in last 10 years.

The additional information. Edition has the right to spend necessary updating and reductions. Authors bear a scientific article maintenance responsibility. To the publication those articles which have received a positive response are represented only. If article is not published, the edition decision is possible to data of authors, the manuscript and disks do not come back.

MACHINE SCIENCE № 2, 2025

Editorial address:
AZ1073, Azerbaijan, Baku, H.Javid av., 25.
Telephone: (+994 12) 538 94 12

E-mail: msj@aztu.edu.az
Web site: http://msj.aztu.edu.az/

Format: 60×84 1/8.
Number of copies printed: 100.

Publisher: AzTU Publisher